The Journal of Physiology

Multiscale mechanistic modelling of heterogeneity in cardiac sub-cellular calcium handling accounting for variable t-system density

Michael A Colman[1], Yohannes Shiferaw[2] and David Conesa[1]

[1]*Department of Biomedical Sciences, Faculty of Biological Sciences, University of Leeds, Leeds, West Yorkshire, UK*
[2]*Department of Physics & Astronomy, California State University, Northridge, California, USA*

Handling Editors: Eleonora Grandi & Mary Margot Maleckar

The peer review history is available in the Supporting Information section of this article (https://doi.org/10.1113/JP290572#support-information-section).

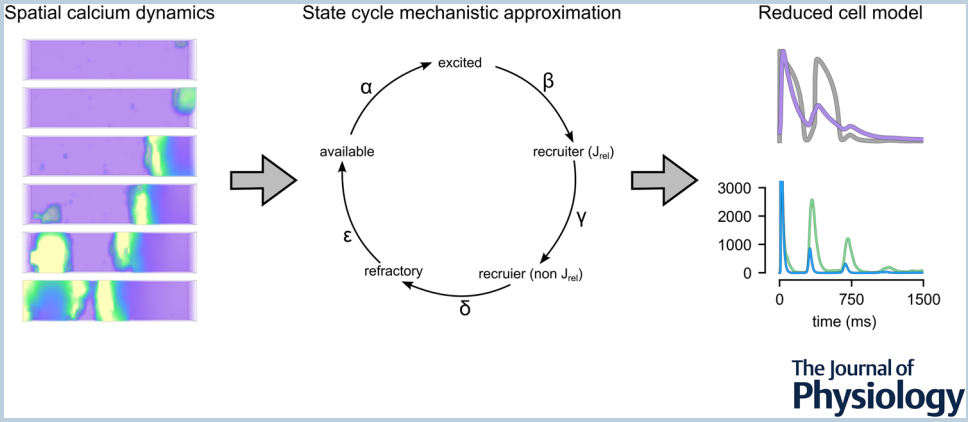

Abstract figure legend Illustration of spatial calcium dynamics (left panels) and the state cycle approximation (middle panel) that enables reduced simulation of spatially dependent dynamics without explicit description of space (right panels). The selected example here illustrates a spontaneous calcium wave, showing temporal snapshots of local calcium concentration in the cell (left) and the reduced model's reproduction of the spontaneous calcium transient that underlies a delayed after depolarisation and initiates a triggered action potential (right).

Abstract Spatial properties of subcellular calcium handling in cardiac myocytes underpin both normal and abnormal functions. The structure and density of the transverse and axial tubular system (t-system) strongly determine the spatiotemporal synchrony of calcium-induced-calcium-release, and arrhythmogenic behaviours such as calcium transient alternans and subcellular calcium waves inherently depend on stochastic calcium spark initiation and spatial diffusion. Although detailed three-dimensional cellular models can reproduce these processes, they are computationally

Michael Colman received his Masters in Theoretical Physics from the University of Manchester in 2008, followed by a PhD in Biological Physics in 2012. He is currently based at the University of Leeds. His research focuses on the development and application of novel multi-scale joint experimental-simulation frameworks to investigate the mechanisms of cardiac electrophysiology and intracellular calcium handling, with the aim of improving understanding of cardiac dysfunction and ultimately informing better diagnostic and therapeutic strategies. His primary interest lies in sub-micron to whole-heart interactions and their roles in the pathologies associated with heart failure, atrial fibrillation, and ageing.

DOI: 10.1113/JP290572

prohibitive for the tissue-scale simulations required to investigate arrhythmia mechanisms or inform patient-specific modelling.
In this study, we develop a computationally efficient model that reproduces a broad range of spatially dependent subcellular calcium-handling phenomena. The model tracks the population occupancy of distinct states of calcium release units (CRUs), with activation rates that capture the different mechanisms of calcium spark initiation (triggered, spontaneous and spatially recruited). The model has been designed as an independent module that can be integrated into existing cell models and enables the simulation of variable t-system density.
We demonstrate in three established cell models that this framework captures normal and abnormal pacing dynamics, including centripetal calcium waves in cells lacking a robust t-system, multiple mechanisms of calcium transient alternans, delayed triggered calcium sparks, and spontaneous calcium release mediated early and delayed after depolarisations. The model achieves this while maintaining a computational efficiency sufficient for large-scale tissue simulations, suitable for mechanistic and clinical applications.

(Received 18 November 2025; accepted after revision 7 April 2026; first published online 30 May 2026)
Corresponding author M. A. Colman: Department of Biomedical Sciences, Faculty of Biological Sciences, University of Leeds, Leeds, West Yorkshire, UK. Email: M.A.Colman@leeds.ac.uk

Key points

- Spatial features of sub-cellular calcium handling are integral to physiological and pathophysiological dynamics. This is particularly true for myocytes without a robust sub-cellular transverse and axial tubule system.
- Traditional computational models of cardiac myocytes do not capture these important features; detailed spatiotemporal models of sub-cellular calcium handling are computationally intensive and unsuitable for large-scale tissue simulation.
- We develop a novel model that captures spatial features of the sub-cellular calcium handling system without requiring explicit spatial modelling.
- The model was capable of reproducing normal and abnormal calcium handling dynamics, including centripetal calcium waves, calcium transient alternans, and spontaneous calcium sparks and waves, while being sufficiently efficient to perform tissue-scale simulations.

Introduction

Intracellular calcium handling in cardiomyocytes underlies many vital processes of cellular signalling. A primary function is excitation-contraction coupling (EC coupling), providing the link between electrical excitation and cellular contraction that enables organised rhythmic heartbeats (Bers, 2002; Stern et al., 1999). This is underpinned by calcium-induced-calcium-release (CICR), a process where an influx of calcium ions through the L-type calcium channels (LTCCs) during the action potential (AP) triggers the opening of the type-2 ryanodine receptors (RyR2s) that induces a much larger release of calcium from the intracellular calcium store, the sarcoplasmic reticulum (SR), into the intracellular space. The elevated intracellular calcium concentration initiates a cascade of processes that result in contraction of the cardiomyocyte.

Cardiac myocytes contain spatially heterogeneous structures that facilitate CICR throughout the intracellular volume to deliver homogeneous cell-wide contraction. The transverse and axial tubule system (t-system) comprises invaginations of the surface membrane that penetrate deep into the cell interior, ensuring delivery of the AP and hence LTCC trigger for CICR throughout the cell volume (Dibb et al., 2022; Ferrantini et al., 2013; Setterberg et al., 2021). Healthy ventricular myocytes contain a dense and robust t-system that ensures optimal cellular and tissue contraction. However, atrial myocytes of small mammals are largely devoid of a t-system, and, where atrial myocytes of large mammals do contain a t-system, it is less dense and more variable than in ventricular myocytes (Dibb et al., 2009; Richards et al., 2011). Remodelling of t-system structure, including axialisation (a shift to primarily longitudinally rather than transversally oriented tubules) and detubulation

(a reduction or almost entire loss of the t-system), has been linked to the mechanisms that underlie a loss of synchronisation of CICR, and hence reduced contractile performance, in multiple cardiac conditions (Dibb et al., 2022; Louch et al., 2004).

Spatial features of sub-cellular calcium handling are also central for multiple mechanisms of arrhythmia. Spontaneous calcium release events, including calcium sparks and waves, are inherently spatial phenomena and can result in early and delayed after depolarisations (EADs and DADs, respectively) that promote both trigger and substrate for arrhythmia (Eisner et al., 2009; Liu et al., 2015; Shiferaw et al., 2018). Calcium transient alternans, where the amplitude of the calcium transient alternates on a beat-by-beat basis in regular or irregular cycles, can result in abbreviated cellular contraction and may also lead to arrhythmia by introducing spatial heterogeneities of the AP duration that can promote wavebreak and the development of re-entry (Aistrup et al., 2009; Clusin, 2007; Kanaporis et al., 2023; Mora et al., 2019). Recent modelling studies have highlighted the important role that spatial features of calcium handling play in the mechanisms of calcium transient alternans (Alvarez-Lacalle et al., 2015; Holmes et al., 2022). The intracellular calcium handling system is therefore a major component of cardiac function relevant for both contractile performance and arrhythmia; detailed elucidation of its underlying mechanisms is vital to underpin better diagnostic and treatment strategies to manage a multitude of cardiac conditions.

This presents a major research challenge, not only because of the multitude of different presentations of cardiac dysfunction, but also in understanding how these (sub) micron-scale processes ultimately result in dysfunction of the whole-organ (Colman et al., 2022; Eisner et al., 2009; Xie et al., 2010). It is not currently possible through experimental approaches to study simultaneously sub-cellular and whole-heart function, and integration of concepts and mechanisms between these scales is far from trivial. Recent experimental approaches are helping to close this gap, for example, in the simultaneous sub-cellular imaging of multiple myocytes in tissue slices (Borile et al., 2021; Kazakova et al., 2025; Pitoulis et al., 2020; Wang et al., 2015). Despite the translational promise of these approaches, they are still substantially limited in spatial scale compared to the whole heart.

Computational modelling provides a powerful complementary approach that enables controlled and clean dissection of different physiological processes in single-cell and whole-organ scale simulations (Colman et al., 2022; Heijman et al., 2021; Niederer et al., 2019; Roney et al., 2018). However, the traditional non-spatial 'common pool' computational models of cellular electrophysiology, that are suitable for tissue-scale simulation, do not capture the important features and processes that depend on spatial calcium handling. Highly detailed models of spatial calcium handling in 3D offer a powerful approach to capture these important spatial features in both health and disease (Colman et al., 2017; Nivala et al., 2012; Restrepo et al., 2008; Shiferaw et al., 2017; Zhong & Karma, 2024), indeed helping to uncover the mechanisms of calcium spark initiation and propagation associated with normal EC-coupling, calcium transient alternans, and spontaneous sparks and waves. These models, however, are too computationally intensive to be applied in the large-scale tissue simulations required to understand arrhythmia mechanisms or for clinically focused, patient-specific image-based modelling (Colman et al., 2022; Xie et al., 2010).

Recent modelling developments have sought to bridge these scales, including independent approaches developed by the authors of this present study (Colman, 2019; Shiferaw et al., 2018) and others (Campos et al., 2023; Liu et al., 2015). Summarised in our recent review (Colman et al., 2022), these phenomenological approaches can be broadly considered to fit into two categories: 'spontaneous release functions' (Colman, 2019), where analytical waveforms with randomly sampled parameters enable modelling of the statistics and dynamics of spontaneous calcium release, and 'population dynamics' approaches (e.g. Shiferaw et al., 2018), where the cell comprises a discrete number of CRUs, and the number of active units, corresponding to calcium sparks, is tracked with stochastic algorithms. The spontaneous release function approach is ideally suited to the controllable exploration of the mechanisms of the synchronisation of DADs and spontaneous focal excitations, whereas the population dynamics approach has more general applicability in potentially being able to also model calcium transient alternans, EADs, and CICR in cells without a robust t-system.

In this study, we present a novel non-spatial, population dynamics model of calcium spark activation and recruitment that captures a variety of spatial calcium handling phenomena. A mechanistically motivated model structure, with populations separated into those that are coupled and not coupled to the t-system, enabled a robust reproduction of normal CICR, rate dependence, calcium spark spatial recruitment, spontaneous calcium release hierarchy and multiple mechanisms of calcium-transient alternans, in the context of a fully variable t-system density. The model was constructed with portability as a primary motivation, providing intuitive, physiologically driven control parameters that enable implementation into cell models with markedly different calcium handling system formulations and dynamics.

Methods

In this section core concepts of subcellular calcium handling are first discussed. The development and

structure of the 'spark-population' model then outlined, and the physiological interpretation of the control parameters is discussed. The portability of the model is demonstrated by integrating it into three contemporary common-pool models of cellular electrophysiology and calcium handling. Full equations are provided in the **Appendix**, but we do provide sufficient detail below to understand every aspect of how the model works.

Ethical approval

Experimental data were only used for minimal illustrative purposes in this study. All experiments were performed according to the United Kingdom Animals (Scientific Procedures) Act of 1986 and approved by the local Animal Welfare and Ethical Review Body (UK Home Office PPL No 70/8399). Male adult (150–200 g) Wistar rats were obtained from Central Biomedical Services, University of Leeds, and housed according to the Guide for the Care and Use of Laboratory Animals. Animals were bred and aged in-house at 20-22°C with 50% relative humidity on a 12-h light/dark cycle. Animals had no additional intervention, with *ab libitum* access to regular chow and water. Animals were euthanised by concussion followed by cervical dislocation.

Concepts of spatial subcellular calcium handling

Calcium sparks. Calcium sparks (Fig. 1Aa) are the elementary unit of the cellular calcium transient (Cheng et al., 1996; Stern et al., 1999). They are underpinned by the activity of clusters of RyR2s on the membrane of the SR that mediate a substantial release of calcium into the cytosolic space (Fig. 1Aa–c). RyR2 clusters are spatially distributed throughout the intracellular volume (Fig. 1Ab,d), and calcium sparks are an inherently local phenomenon, on spatial scales of a few microns; the whole-cell calcium transient associated with cell-wide CICR is the sum of thousands of spatially distributed calcium sparks within the cell.

Gating of RyR2s is sensitive primarily to cytosolic calcium concentration. Because open RyR2s release calcium into the local space of the cluster, this presents a feedback mechanism for the activation of neighbouring channels within the local cluster neighbourhood, underlying a full calcium spark. The calcium load in the SR determines the magnitude of calcium released through open RyR2s and therefore strongly influences the strength of this feedback. During CICR, calcium sparks are robustly triggered through the activity of the LTCCs that underlie the L-type calcium current (I_{CaL}). LTCCs are co-located with the RyR2s in junctional complexes (Fig. 1*Ab*,*c*) and the calcium influx associated with I_{CaL} during the AP sufficiently elevates cytosolic calcium concentration to initiate calcium sparks throughout the cell.

Calcium sparks can also occur without the LTCC trigger acting on a local cluster, through spontaneous activity and spatial recruitment. Spontaneous calcium sparks occur due to stochastic RyR2 openings during diastole and are enhanced at high SR calcium loads. Active calcium sparks may elicit calcium sparks in neighbouring clusters through spatial calcium diffusion. Diffusion is highly buffered, and propagation of calcium within the cell is driven primarily by subsequent recruitment of neighbouring clusters in a 'fire-diffuse-fire' mechanism (Thul et al., 2015). Thus in a practical sense, calcium sparks can be considered to have three distinct mechanisms of activation: triggered by I_{CaL}, spontaneous and recruited by neighbours.

The calcium release unit. In a simplified conception of the structure-function relationships underlying CICR in cardiomyocytes, one can consider single CRUs that are the local sub-cellular complexes comprising the junction coupling the LTCCs with the RyR2s and the surrounding intracellular and SR spaces (Fig. 1*Ad*). Crudely, cardiac myocytes can be considered as a 3D grid of spatially discrete CRUs, each comprising RyR2 clusters, LTCCs (where cell membrane is present) and local intracellular and SR calcium concentrations and other fluxes (Fig. 1*Ae*). In this simplification a calcium spark is localised to a single CRU and calcium spark propagation occurs through the recruitment of neighbouring CRUs.

The functional CRU cycle. We develop a stochastic model that is constructed on a mechanistic description of the temporal evolution of the functional states of a CRU associated with a calcium spark. A CRU can be considered to evolve through five functionally distinct states during a calcium spark (Fig. 1*B*; Table 1):

(1) Available: There is currently no activity of the CRU: All RyR2s within the cluster are closed; local cytosolic calcium concentration is low, at diastolic resting levels, and junctional Ca_{SR} is high (i.e. filled). The CRU is ready to be activated by any of the initiation mechanisms.

(2) Excited: A spark has been initiated, and the CRU is in its first active state. RyR2 opening generates intracellular calcium release flux, J_{rel}, and the local calcium concentration rises. At this stage, there has been insufficient time for calcium to diffuse to neighbouring CRUs, so the spark does not yet contribute to spatial recruitment.

(3) Recruiter (J_{rel}): After a short period, on the order of a few ms, the calcium concentration in the CRU may be sufficiently elevated to initiate a calcium spark in a neighbouring CRU. The CRU contributes both to intracellular calcium release and to spatial recruitment.

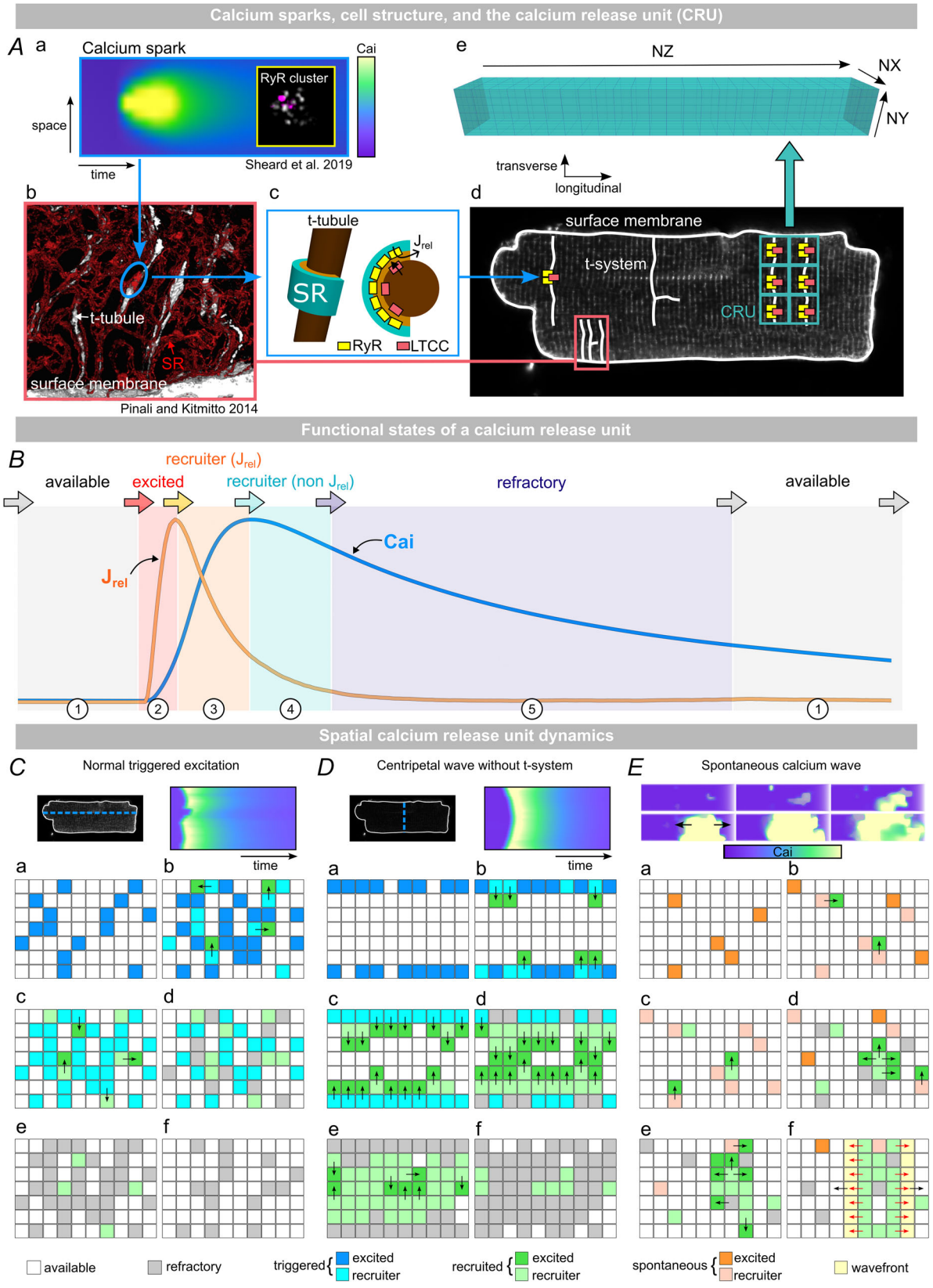

Figure 1. Illustration of calcium sparks and calcium release unit dynamics.
Aa, illustrative space-time plot of a calcium spark (produced through simulation). Inset – super resolution reconstruction of RyR2 distribution in a cluster underlying a calcium spark. Reproduced with permission from

Sheard et al. (2019). *b,c*, Illustration of the structural complex that couples ryanodine receptors (RyR2s) and L-type calcium channels (LTCCs) and underlies a calcium spark. Electron microscope reconstruction in *b* modified with permission from Pinali & Kitmitto (2014) whereas c shows a schematic illustration of RyR2-LTCC coupling in this structure. *d*, illustration of cell-wide t-system structure. Confocal image from unpublished data from the lab and provided for illustrative purposes only; indeed the annotations do not correspond to the real underlying data. The panel highlights a few transverse and axial tubules and illustrates RyR2 cluster distribution in calcium release units (CRUs) that can be approximated as a 3D grid (**e**) to represent the cell volume. *B*, illustration of the state cycle of a CRU associated with a calcium spark, overlaying the CRU waveforms for intracellular calcium release, J_{rel}, and the cytosolic calcium transient, Cai, on the different states of the outlined cycle. Numbers correspond to those in the main text description of this cycle. *C–E*, illustration of different calcium handling phenomena using the CRU grid concept. Top panels illustrate longitudinal *(in C)*, and transverse *(in D)*, calcium linescans or temporal snapshots of spatial calcium concentration *(in E)*; *a–f*, temporal snapshots of each phenomenon on a CRU grid.

Table 1. Functional contributions of the different CRU states.

State	Contributes to J_{rel}	Contributes to recruitment	Approx. duration	Rate constant for transition to next state
(1) Available	No	No	—	α
(2) Excited	**Yes**	No	10 ms	β
(3) Recruiter (J_{rel})	**Yes**	**Yes**	30 ms	γ
(4) Recruiter (non-J_{rel})	No	**Yes**	10–20 ms	δ
(5) Refractory	No	No	50–100+ ms	ϵ

(4) Recruiter (non-J_{rel}): Calcium release is typically a relatively short process, on the order of tens of ms, after which local SR calcium is depleted, RyR2s close and J_{rel} terminates. Average concentration in the CRU may still be sufficiently large to recruit neighbours.

(5) Refractory: Finally, the spark has terminated. The CRU is no longer active and does not contribute to J_{rel} or spatial recruitment, but the junctional Ca_{SR} concentration is initially still depleted, and the CRU is unable to undergo a newly elicited calcium spark. After some time, the junctional Ca_{SR} has sufficiently refilled, and the CRU can be considered fully recovered, available for the initiation of another calcium spark.

This simplification of the cardiac myocyte as a 3D grid of CRUs that each undergo this cycle during a calcium spark provides an intuitive framework for the understanding and visualisation of spatial calcium handling associated with different phenomena, including normal cell-wide CICR, centripetal calcium waves in detubulated cells, and spontaneous calcium sparks and full-cell propagating waves (Fig. 1*C–E*).

Overview of the spark-population model

The intention of the model developed in this study was to achieve the goal of incorporating the three mechanisms of calcium spark initiation (triggered, spontaneous and spatially recruited) into traditional, common-pool models of cardiac myocyte electrophysiology and calcium handling. This was achieved by formulating a model that describes the state occupancy of a discrete population of N_{tot} CRUs, representing a 3D cell. The model does not directly describe RyR2 gating nor local calcium concentration; instead, it tracks the number of CRUs that are in each state of the functional cycle.

The model is implemented as a standalone module that can be integrated into biophysically detailed cell models. At each timestep, it receives I_{CaL} and Ca_{SR} as inputs and returns the proportion of the total CRU population contributing to J_{rel}, replacing the native RyR2 formulation of the host cell model. Calcium concentrations in the host model then evolve according to J_{rel} and its own calcium-handling formulations.

A five-state unidirectional cycle describing CRU evolution was defined based on the mechanistic framework outlined previously (Fig. 2*Aa*; Table 1). At each timestep, the model calculates the number of CRUs that transition between connected states. To preserve the probabilistic nature of these transitions in a discrete population of N_{tot} CRUs, transitions are determined by random binomial sampling. The number of trials corresponds to the population available for the given state transition. The resulting sample therefore provides a probabilistic estimate of the number of CRUs that undergo each transition at a given timestep. In general:

$$\Delta^{+}N_{state} = B\left(p, N_{available}\right)$$

where Δ^{+} refers to the number of CRUs that have transitioned to a given state, and $B\left(p, N\right)$ refers to the random binomial sample with probability p and population N.

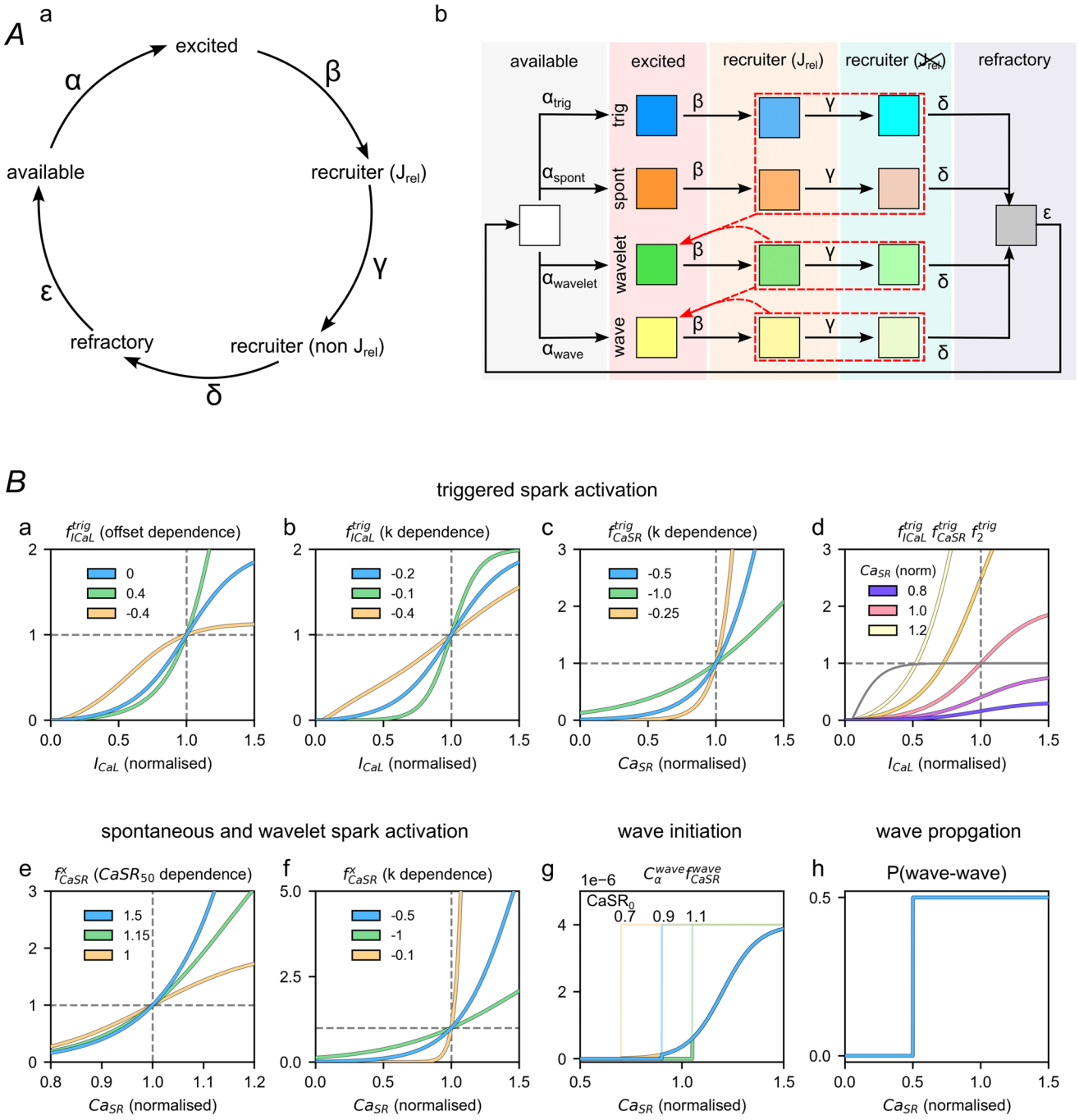

Figure 2. Fundamental model construction.
Aa, illustration of the five-state cycle of a CRU and the transition rates associated with each state. *b*, The full state cycle with the different pathways representing different spark activation mechanisms. The red arrows indicate that these states determine the available population for activation of the wavelet or wave states and are not themselves state transitions. *B*, Forms of the functions that determine the I_{CaL} and Ca_{SR} dependence of the α transition rates and illustration of the impact of the controlling parameters. *a–d* illustrate the functions that control the activation of triggered calcium sparks. Different coloured lines correspond to different values for the parameters in the parentheses of each panel title. Dotted lines indicate where the functions equal unity at the normalised I_{CaL} or Ca_{SR} values. Grey line in *d* illustrates the f_2^{trig} function that scales the response at low I_{CaL}. *e,f* show the Ca_{SR}-dependent functions controlling spontaneous and wavelet activation rates illustrating the impact of varying the half-maximal activation constant, $Ca_{SR_{50}}$, and the gradient parameter, k_{CaSR}. *g–h* illustrate the functions underpinning full-cell wave initiation and self-propagation. The thin coloured step-functions in **g** show the f_2^{wave} function at different thresholds (Ca_{SR_0}).

The probability is given as the product of the integration timestep, Δt, and the relevant transition rate, α, β, γ, δ or ϵ that corresponds to the physiological processes associated with each functional state (Fig. 2*Aa*). The activation transition rates (α) represent the different mechanisms through which a spark can be initiated and are examined in detail in the next sections. The remaining transition rates are constants in this initial implementation and can be conveniently derived from parameters that describe the approximate duration of each state (Table 1). The transition rate from the excited to the recruiter state (β) corresponds to the time between a spark being initiated and it being able to recruit neighbours ($t_{\text{wavedelay}}$), which effectively determines the calcium wave propagation velocity:

$$\beta = \frac{\ln(2)}{0.5 \cdot t_{\text{wavedelay}}}$$

The rate describing the transition from the recruiter (J_{rel}) to recruiter (non-J_{rel}) states, γ, is derived from the total duration of J_{rel} (t_{Jrel}):

$$\gamma = \frac{\ln(2)}{0.5 \cdot (t_{\text{Jrel}} - t_{\text{wavedelay}})}$$

The rate describing the transition from the recruiter (non-J_{rel}) to the refractory state, δ, is defined from the total time that CRUs may recruit neighbours (t_{recruit}):

$$\delta = \frac{\ln(2)}{0.5 \cdot (t_{\text{recruit}} - t_{J_{\text{rel}}})}$$

Finally, the rate ϵ controls the total refractory or recovery time, determining how rapidly CRUs in the refractory state transition to the available state, and is simply set to a constant rate. Note that this cycle is not a five-state Markov chain model, and CRUs can only transition in one direction.

Mechanisms of spark initiation

To represent the distinct mechanisms of spark activation, and the potentially different behaviour of these sparks, we separate the active states into four distinct populations (Fig. 2*Ab*):

(1) Triggered sparks refer to those activated by I_{CaL}.
(2) Spontaneous sparks refer to sparks that are not related to an external trigger.
(3) Wavelet sparks refer to CRUs that have been activated through recruitment by neighbouring CRUs as part of a small wavelet but not a full-cell calcium wave.
(4) Wave sparks refer to those that are part of a full-cell, robustly propagating calcium wave, with a wavefront size determined by cellular geometry.

In this framework, the number of CRUs in the recruiter states determines the population capable of recruiting neighbours. Consequently, the model captures the hierarchy from local to cell-wide calcium release: a currently active CRU (triggered or spontaneous) may activate a neighbour (wavelet), which can in turn recruit additional CRUs, potentially leading to a global calcium wave.

Wavelets and waves were treated separately for two reasons. First, it allows self-propagation of wavelets to remain controlled, preventing unstable dynamics and uncontrolled growth of the active population. Second, it permits explicit control of wavefront size for full-cell waves based on cell structure. Details of this formulation are provided later in **Methods ('Activation and propagation of full-cell calcium waves')** and in the Appendix. This set-up enables mechanism-dependent transition rates and provides a straightforward means to track the population of each state for analysis and interpretation.

General functional form of I_{CaL} and Ca_{SR} dependence. The spark activation rates are dependent on I_{CaL} and/or Ca_{SR}, with specific dependencies defined by the underlying mechanism of spark initiation. Throughout the model, the same general approach is used to describe this I_{CaL} and Ca_{SR} dependence. Logistic sigmoidal functions of the following general form are utilised:

$$f = \frac{A}{1 + b^{(x-(x_{50}+x_{50_{\text{shift}}}))/k}}$$

where x refers to the variable (I_{CaL} or Ca_{SR}), b is the exponential base (either e or 10), x_{50} is the basal half-maximal activation constant, $x_{50_{\text{shift}}}$ is an applied modulation shift to the half maximal activation constant, k is the slope parameter and A is the amplitude. This formulation allows intuitive control over both the range of I_{CaL} or Ca_{SR} values for which the transition rates are dynamic, and the steepness of this dependence, through the x_{50} and k parameters. Thus, the physiological characteristics of calcium spark initiation mechanisms are captured through the choice of these parameters and the nature of their functional dependencies.

Normalisation and parameterisation. To facilitate portability and comparable interpretation of the transition rate constants across cell models with different I_{CaL} and Ca_{SR} dynamics, functions are normalised to defined factors obtained from normal pacing of the native cell models. In the present study, normal pacing was considered as pacing to steady state under basal conditions at a cycle length of 1000 ms, but this cycle length should be adjusted based on the species of model

being developed. The normalised variables are defined as:

$$\overline{I_{\mathrm{CaL}}} = \frac{I_{\mathrm{CaL}}}{I_{\mathrm{CaL}}^{\mathrm{peak}}}$$

$$\overline{Ca_{\mathrm{SR}}} = \frac{Ca_{\mathrm{SR}}}{Ca_{\mathrm{SR}}^{\mathrm{diastolic}}}$$

Here $I_{\mathrm{CaL}}^{\mathrm{peak}}$ refers to the peak I_{CaL} observed during an AP, and $Ca_{\mathrm{SR}}^{\mathrm{diastolic}}$ refers to the end diastolic Ca_{SR} load. Both quantities are empirically determined from simulations using the original cell models. These reference values need not be exact, nor strictly maintained during steady-state pacing in the integrated model; rather they serve to normalise all functions relative to I_{CaL} and Ca_{SR}. This allows the parameters governing rate constants, gradients and half-maximal activation to be expressed on a comparable scale across models, thereby facilitating both model development and inter-model comparison. For brevity in this description assume all I_{CaL} and Ca_{SR} values in the functions described below refer to these normalised values.

The I_{CaL} and Ca_{SR}-dependent functions are defined such that they return a value of unity when the input equals its reference value (i.e. the normalised I_{CaL} or Ca_{SR} equals one). To achieve this, the amplitude of each sigmoidal function is rescaled based on its half-activation and slope parameters. This ensures that variations in these parameters alter only the steepness and non-linearity of the functions without affecting the basal rate. This is convenient both for isolating the functional implications of these parameters and for comparisons between models. Applied shifts to the half-maximal activation values, for example, for modulation or disease conditions, are not included in the amplitude calculation and thus can directly affect basal spark rate as a consequence of shifting the I_{CaL} or Ca_{SR} dependence.

Triggered sparks. For triggered sparks, the total number available for activation is simply the total number currently in the available state. The number of newly excited triggered CRUs at a given timestep is calculated by:

$$\Delta^{+}N_{\mathrm{excited}}^{\mathrm{trig}} = B\left(\Delta t \alpha_{\mathrm{trig}}, N_{\mathrm{available}}\right)$$

The activation rate, α, depends on both I_{CaL} (trigger) and Ca_{SR} (feedback):

$$\alpha_{\mathrm{trig}} = C_{\alpha}^{\mathrm{trig}} f_{\mathrm{I_{CaL}}}^{\mathrm{trig}} f_{2}^{\mathrm{trig}} f_{\mathrm{Ca_{SR}}}^{\mathrm{trig}}$$

where $C_{\alpha}^{\mathrm{trig}}$ is the transition rate constant. The L-type calcium current dependence is defined as (Fig. 2*Ba–b*):

$$f_{\mathrm{I_{CaL}}}^{\mathrm{trig}} = \frac{A_{\mathrm{I_{CaL}}}^{\mathrm{trig}}}{1 + \mathrm{e}^{\left(I_{\mathrm{CaL}} - \left(I_{\mathrm{CaL_{50}}} + I_{\mathrm{CaL,\,offset}} + I_{\mathrm{CaL_{50,\,shift}}}\right)\right)/k_{\mathrm{ICaL}}}}$$

$$f_{2}^{\mathrm{trig}} = \frac{2}{1 + \mathrm{e}^{(I_{\mathrm{CaL}} - 0.05)/-0.1}} - 1$$

where I_{CaL} refers to the normalised value at the given timestep of the model, and $I_{\mathrm{CaL_{50}}}$, $I_{\mathrm{CaL,\,offset}}$ and k_{ICaL} are all constants. $I_{\mathrm{CaL,\,offset}}$ shifts the half maximal activation pre-normalisation, to control the shape of the response to I_{CaL} (**Appendix** Fig. A1; it can be assumed to be zero for understanding of model set-up). f_{2}^{trig} is present to impose that the response is robustly zero at low I_{CaL}, independent of the gradient of the main function (Fig. 2*Bd*). $I_{\mathrm{CaL_{50,\,shift}}}$ is a modulation parameter with a default value of 0. The amplitude coefficient, $A_{\mathrm{I_{CaL}}}^{\mathrm{trig}}$, is calculated based on $I_{\mathrm{CaL,\,offset}}$ and the gradient, k_{ICaL}:

$$A_{\mathrm{ICaL}}^{\mathrm{trig}} = 1 + \mathrm{e}^{-I_{\mathrm{CaL,\,offset}}/k_{\mathrm{ICaL}}}$$

In the full implementation, $I_{\mathrm{CaL_{50}}}$ is defined as a function of Ca_{SR} and used to impose Ca_{SR}-dependent control over the shape of the response. This is described in detail in the Appendix but is not necessary to understand the workings of the model; we consider it to be a constant set to 1.0 in this description. The gradient parameter k_{ICaL} is therefore the primary control parameter to determine the steepness of the response to I_{CaL} (Fig. 2*Bb*).

The Ca_{SR} dependence is defined by:

$$f_{\mathrm{CaSR}}^{\mathrm{trig}} = \frac{A_{\mathrm{CaSR}}^{\mathrm{trig}}}{1 + 10^{\left(Ca_{\mathrm{SR}} - \left(Ca_{\mathrm{SR_{50}}}^{\mathrm{trig}} + Ca_{\mathrm{SR_{50,\,shift}}}^{\mathrm{trig}}\right)\right)/k_{\mathrm{CaSR}}^{\mathrm{trig}}}}$$

where the amplitude coefficient, $A_{\mathrm{CaSR}}^{\mathrm{trig}}$, is also calculated to impose the function equalling unity at normalised Ca_{SR}:

$$A_{\mathrm{CaSR}}^{\mathrm{trig}} = 1 + 10^{\left(1 - Ca_{\mathrm{SR_{50}}}^{\mathrm{trig}}\right)/k_{\mathrm{CaSR}}^{\mathrm{trig}}}$$

$k_{\mathrm{CaSR}}^{\mathrm{trig}}$ and $Ca_{\mathrm{SR_{50}}}^{\mathrm{trig}}$ are both constants that form control parameters for the impact of Ca_{SR} load feedback on triggered calcium sparks (Fig. 2*Bc*) and $Ca_{\mathrm{SR_{50,\,shift}}}^{\mathrm{trig}}$ is a modulation parameter with a default value of 0. Thus, the model contains a controllable shape of response to I_{CaL} that also includes feedback amplification by the Ca_{SR} load (Fig. 2*Bd*).

Spontaneous sparks. The creation of spontaneous sparks is dependent solely on Ca_{SR} and has a similar functional form to the Ca_{SR} dependence of triggered sparks:

$$\Delta^{+}N_{\mathrm{excited}}^{\mathrm{spont}} = B\left(\Delta t \alpha_{\mathrm{spont}}, N_{\mathrm{available}}\right)$$

$$\alpha_{\mathrm{spont}} = C_{\alpha}^{\mathrm{spont}} f_{\mathrm{CaSR}}^{\mathrm{spont}}$$

$$f_{\mathrm{CaSR}}^{\mathrm{spont}} = \frac{A_{\mathrm{CaSR}}^{\mathrm{spont}}}{1 + 10^{\left(Ca_{\mathrm{SR}} - \left(Ca_{\mathrm{SR_{50}}}^{\mathrm{spont}} + Ca_{\mathrm{SR_{50,\,shift}}}^{\mathrm{spont}}\right)\right)/k_{\mathrm{CaSR}}^{\mathrm{spont}}}}$$

$$A_{\mathrm{CaSR}}^{\mathrm{spont}} = 1 + 10^{\left(1 - Ca_{\mathrm{SR_{50}}}^{\mathrm{spont}}\right)/k_{\mathrm{CaSR}}^{\mathrm{spont}}}$$

where C_α^{spont} is the transition rate constant and $Ca_{\text{SR}_{50}}^{\text{spont}}$, $k_{\text{CaSR}}^{\text{spont}}$ and $A_{\text{CaSR}}^{\text{spont}}$ have equivalent interpretations to their triggered spark counterparts.

The parameter $Ca_{\text{SR}_{50}}^{\text{spont}}$ determines the degree of non-linearity in the dependence on Ca_{SR} in the basal load region (Fig. 2*Be*). If this parameter is set to one, the response is approximately linear in this Ca_{SR} region; larger values (e.g. 1.5) produce a predominantly exponential dependence. In general this parameter is set to around 1.5 to preserve the non-linearity of calcium response observed, but this may be adjusted if desired. The gradient parameter $k_{\text{CaSR}}^{\text{spont}}$ controls the steepness of the relationship (Fig. 2*Bf*).

Wavelet sparks. Wavelet sparks may be activated only by CRUs currently in the recruiter states. The number of CRUs available for activation is therefore not equal to the total population of available CRUs but is defined by the product of the number of CRUs in the recruiter states and the number of neighbours that each CRU may excite, $n_{\text{neigh}}^{\text{state}}$.

To preserve independent control over the dynamics of each spark mechanism, recruitment by each type of spark (triggered, spontaneous, or wavelet) is treated separately, each with its own transition rate constant. The number of newly excited wavelet CRUs at each timestep is given by:

$$\Delta^+ N_{\text{excited}}^{\text{wavelet}} = \Delta^+ N_{\text{excited}}^{\text{wavelet-trig}} + \Delta^+ N_{\text{excited}}^{\text{wavelet-spont}} + \Delta^+ N_{\text{excited}}^{\text{wavelet-wavelet}}$$

where:

$$\Delta^+ N_{\text{excited}}^{\text{wavelet-trig}} = B\left(\Delta t \alpha_{\text{wavelet-trig}}, n_{\text{neigh}}^{\text{trig}}\left(N_{\text{recruiter (J}_{\text{rel}})}^{\text{trig}} + N_{\text{recruiter (non-J}_{\text{rel}})}^{\text{trig}}\right)\right)$$

$$\Delta^+ N_{\text{excited}}^{\text{wavelet-spont}} = B\left(\Delta t \alpha_{\text{wavelet-spont}}, n_{\text{neigh}}^{\text{spont}}\left(N_{\text{recruiter (J}_{\text{rel}})}^{\text{spont}} + N_{\text{recruiter (non-J}_{\text{rel}})}^{\text{spont}}\right)\right)$$

$$\Delta^+ N_{\text{excited}}^{\text{wavelet-wavelet}} = B\left(\Delta t \alpha_{\text{wavelet-wavelet}}, n_{\text{neigh}}^{\text{wavelet}}\left(N_{\text{recruiter (J}_{\text{rel}})}^{\text{wavelet}} + N_{\text{recruiter (non-J}_{\text{rel}})}^{\text{wavelet}}\right)\right)$$

where the functional form for the transition rates is identical for the three different mechanisms:

$$\begin{bmatrix} \alpha_{\text{wavelet-trig}} \\ \alpha_{\text{wavelet-spont}} \\ \alpha_{\text{wavelet-wavelet}} \end{bmatrix} = \begin{bmatrix} C_\alpha^{\text{wavelet-trig}} \\ C_\alpha^{\text{wavelet-spont}} \\ C_\alpha^{\text{wavelet-wavelet}} \end{bmatrix} f_{\text{CaSR}}^{\text{wavelet}} f_2^{\text{wavelet}}$$

$$f_{\text{CaSR}}^{\text{wavelet}} = \frac{A_{\text{CaSR}}^{\text{wavelet}}}{1 + 10^{\left(Ca_{\text{SR}} - \left(Ca_{\text{SR}_{50}}^{\text{wavelet}} + Ca_{\text{SR}_{50,\,\text{shift}}}^{\text{wavelet}}\right)\right)/k_{\text{CaSR}}^{\text{wavelet}}}}$$

$$f_2^{\text{wavelet}} = \frac{2}{1 + \text{e}^{\left(Ca_{\text{SR}} - Ca_{\text{SR}_0}^{\text{wavelet}}\right)/-0.0001}} - 1$$

$$A_{\text{CaSR}}^{\text{wavelet}} = 1 + 10^{\left(1 - Ca_{\text{SR}_{50}}^{\text{wavelet}}\right)/k_{\text{CaSR}}^{\text{wavelet}}}$$

where $C_\alpha^{\text{wavelet-trig}}$, $C_\alpha^{\text{wavelet-spont}}$ and $C_\alpha^{\text{wavelet-wavelet}}$ are the transition rate constants for the activation of wavelets by triggered, spontaneous or other wavelet CRUs, respectively. The number of neighbours, $n_{\text{neigh}}^{\text{state}}$, is a constant (set to 2 for triggered and wavelet sparks, and 6 for spontaneous sparks). The Ca_{SR} dependence follows that of spontaneous sparks, with the additional function f_2^{wavelet} that imposes a propagation threshold ($Ca_{\text{SR}_0}^{\text{wavelet}}$) below which the probability of excitation is zero. The number of available CRUs for each of these activations is necessarily constrained by the overall population size to ensure population stability. In practice this constraint is unlikely to require implementation.

Activation and propagation of full-cell calcium waves. Wave CRUs may be activated by either wavelet CRUs (wave initiation) or other wave CRUs (wavefront propagation):

$$\Delta^+ N_{\text{excited}}^{\text{wave}} = \Delta^+ N_{\text{excited}}^{\text{wave-wavelet}} + \Delta^+ N_{\text{excited}}^{\text{wave-wave}}$$

The wavefront size is defined from the cell cross-section in CRUs (i.e. $N_{\text{x}} \times N_{\text{y}}$ where N_{z} defines the cell length and $N_{\text{x}} \times N_{\text{y}} \times N_{\text{z}}$ defines the total population, N_{tot}). The actual size of the wavefront (WF) is taken as a proportion of this cross section (WF = 0.7 $\times$ $N_{\text{x}} \times N_{\text{y}}$) reflecting that not every CRU along the cross section will be activated. Excitation of a wavefront is handled as an essentially binary process: When a new wave is created, two full wavefronts are created instantaneously to represent propagation from the nucleation site in each direction of the cell (as illustrated in Fig. 1*E*). The number of wave CRUs excited by initiation from wavelets is therefore:

$$\Delta^+ N_{\text{excited}}^{\text{wave-wavelet}} = 0.7 N_{\text{x}} N_{\text{y}} B\left(\Delta t \alpha_{\text{wave-wavelet}}, N_{\text{recruiter (J}_{\text{rel}})}^{\text{wavelet}} + N_{\text{recruiter (non-J}_{\text{rel}})}^{\text{wavelet}}\right)$$

$$\alpha_{\text{wave-wavelet}} = C_\alpha^{\text{wave}} f_{\text{CaSR}}^{\text{wave}} f_2^{\text{wave}}$$

$$f_{\text{CaSR}}^{\text{wave}} = \frac{1}{1 + 10^{\left(Ca_{\text{SR}} - \left(Ca_{\text{SR}_{50}}^{\text{wave}} + Ca_{\text{SR}_{50,\,\text{shift}}}^{\text{wave}}\right)\right)/k_{\text{CaSR}}^{\text{wave}}}}$$

$$f_2^{\text{wave}} = \frac{2}{1 + \text{e}^{\left(Ca_{\text{SR}} - Ca_{\text{SR}_0}^{\text{init, wave}}\right)/-0.0001}} - 1$$

where C_α^{wave} is the transition rate constant describing wave initiation. Note that $f_{\text{CaSR}}^{\text{wave}}$ is not scaled by an amplitude coefficient (unlike the other Ca_{SR}-dependent functions); therefore in this case the rate constant C_α^{wave} sets the maximal possible rate of wave creation from wavelets rather than the rate at basal values (Fig. 2*Bg*). The function f_2^{wave} imposes an initiation threshold ($Ca_{\text{SR}_0}^{\text{init, wave}}$)

below which waves cannot be initiated. The comparatively modest growth of $f_{\mathrm{CaSR}}^{\mathrm{wave}}$ at high Ca_{SR} is intentional: the strong non-linearity of full-cell wave creation is already inherited from the dependence of wave initiation on the number of active wavelet CRUs.

Robust propagation of the wavefront aims to approximate a near one-to-one mapping of CRU activation along a homogeneous travelling wavefront. Rather than using a continuous transition rate to model neighbour recruitment, propagation is handled via an explicitly defined probability that a recruiter wave CRU will successfully recruit a neighbour over its active lifetime. Using a lifetime probability avoids repeatedly sampling a small per-timestep probability and better captures the one-to-one propagating nature of a wavefront. For variability in the travelling wavefront, the maximum per-lifetime recruitment probability is set to 0.5, and each recruiter CRU is allowed to attempt to activate up to two neighbours. Because this is a lifetime probability (not a per-timestep rate) the binomial draw is performed once per newly created set of recruiter wave CRUs. Thus the number of excited CRUs due to wavefront propagation is:

$$\Delta^{+}N_{\mathrm{excited}}^{\text{wave-wave}} = B\left(P(\text{wave-wave}),\, 2\Delta^{+}N_{\mathrm{recruiter}}^{\mathrm{wave}}\right)$$

$$P(\text{wave-wave}) = 0.5\left(\frac{2}{1+\mathrm{e}^{\left(Ca_{\mathrm{SR}}-Ca_{\mathrm{SR}_0}^{\text{prop, wave}}\right)/-0.0001}}-1\right)$$

This simple step function returns a probability of 0.5 above the propagation threshold, $Ca_{\mathrm{SR}_0}^{\text{prop, wave}}$, and zero below it (Fig. 2*Bh*).

The model does not explicitly represent spatial boundaries and therefore the current implementation theoretically allows for infinitely traveling calcium waves (all available CRUs are 'seen' by the wavefront as there is no spatial restriction). Wavefront termination is handled by two mechanisms:

(1) Due to Ca_{SR} threshold for self-propagation; if Ca_{SR} is sufficiently depleted by the wave, then the imposition of this threshold will terminate wave propagation.

(2) Through imposed stochastic wavefront termination. A termination algorithm probabilistically terminates wavefronts with probability dependent on cell length and the number of concurrently active wavefronts. This reproduces effects such as wavefront collision (multiple waves) and single-front termination when a nucleation site is non-central. Termination is implemented by transitioning N = WF wave CRUs from the excited state into the recruiter (J_{rel}) state without including them in the $\Delta^{+}N_{\mathrm{recruiter}}^{\mathrm{wave}}$ pool used to calculate wavefront self-propagation. These CRUs therefore continue to contribute to J_{rel} but are no longer able to propagate the wave. Due to this stochastic wavefront termination algorithm, one of the two created wavefronts may be randomly rapidly terminated. This corresponds to a nucleation site located near one cell edge, such that only a single wavefront propagates. An extension to the model could be included to permit the explicit generation of singular wavefronts to represent nucleation occurring directly at a cell end, if this feature is determined important for future investigations.

Other state transitions and state occupancy

All remaining transitions around the CRU cycle are determined by a simple product of the transition rate constant and the occupancy of the originating state (e.g. the number of CRUs available for transition to a given recruiter state is set by the current number in the excited state). Full equations for all state transitions are provided in the **Appendix**.

The available and refractory CRUs are common to all mechanisms, whereas the activated CRUs are tracked in the distinct pathways around the cycle. The net changed in occupancy of each state at a given time-step is therefore described by:

$$\begin{aligned}
\Delta N_{\mathrm{available}} &= \Delta^{+}N_{\mathrm{available}} - \Delta^{+}N_{\mathrm{excited}}^{\mathrm{trig}} - \Delta^{+}N_{\mathrm{excited}}^{\mathrm{spont}} \\
&\quad - \Delta^{+}N_{\mathrm{excited}}^{\mathrm{wavelet}} - \Delta^{+}N_{\mathrm{excited}}^{\mathrm{wave}} \\
\Delta N_{\mathrm{excited}}^{\mathrm{trig}} &= \Delta^{+}N_{\mathrm{excited}}^{\mathrm{trig}} - \Delta^{+}N_{\mathrm{recruiter\ (J_{rel})}}^{\mathrm{trig}} \\
\Delta N_{\mathrm{excited}}^{\mathrm{spont}} &= \Delta^{+}N_{\mathrm{excited}}^{\mathrm{spont}} - \Delta^{+}N_{\mathrm{recruiter\ (J_{rel})}}^{\mathrm{spont}} \\
\Delta N_{\mathrm{excited}}^{\mathrm{wavelet}} &= \Delta^{+}N_{\mathrm{excited}}^{\mathrm{wavelet}} - \Delta^{+}N_{\mathrm{recruiter\ (J_{rel})}}^{\mathrm{wavelet}} \\
\Delta N_{\mathrm{excited}}^{\mathrm{wave}} &= \Delta^{+}N_{\mathrm{excited}}^{\mathrm{wave}} - \Delta^{+}N_{\mathrm{recruiter\ (J_{rel})}}^{\mathrm{wave}} \\
\Delta N_{\mathrm{recruiter\ (J_{rel})}}^{\mathrm{trig}} &= \Delta^{+}N_{\mathrm{recruiter\ (J_{rel})}}^{\mathrm{trig}} - \Delta^{+}N_{\mathrm{recruiter\ (non\text{-}J_{rel})}}^{\mathrm{trig}} \\
\Delta N_{\mathrm{recruiter\ (J_{rel})}}^{\mathrm{spont}} &= \Delta^{+}N_{\mathrm{recruiter\ (J_{rel})}}^{\mathrm{spont}} - \Delta^{+}N_{\mathrm{recruiter\ (non\text{-}J_{rel})}}^{\mathrm{spont}} \\
\Delta N_{\mathrm{recruiter\ (J_{rel})}}^{\mathrm{wavelet}} &= \Delta^{+}N_{\mathrm{recruiter\ (J_{rel})}}^{\mathrm{wavelet}} - \Delta^{+}N_{\mathrm{recruiter\ (non\text{-}J_{rel})}}^{\mathrm{wavelet}} \\
\Delta N_{\mathrm{recruiter\ (J_{rel})}}^{\mathrm{wave}} &= \Delta^{+}N_{\mathrm{recruiter\ (J_{rel})}}^{\mathrm{wave}} - \Delta^{+}N_{\mathrm{recruiter\ (non\text{-}J_{rel})}}^{\mathrm{wave}} \\
\Delta N_{\mathrm{recruiter\ (non\text{-}J_{rel})}}^{\mathrm{trig}} &= \Delta^{+}N_{\mathrm{recruiter\ (non\text{-}J_{rel})}}^{\mathrm{trig}} - \Delta^{+}N_{\mathrm{refractory}}^{\mathrm{trig}} \\
\Delta N_{\mathrm{recruiter\ (non\text{-}J_{rel})}}^{\mathrm{spont}} &= \Delta^{+}N_{\mathrm{recruiter\ (non\text{-}J_{rel})}}^{\mathrm{spont}} - \Delta^{+}N_{\mathrm{refractory}}^{\mathrm{spont}} \\
\Delta N_{\mathrm{recruiter\ (non\text{-}J_{rel})}}^{\mathrm{wavelet}} &= \Delta^{+}N_{\mathrm{recruiter\ (non\text{-}J_{rel})}}^{\mathrm{wavelet}} - \Delta^{+}N_{\mathrm{refractory}}^{\mathrm{wavelet}} \\
\Delta N_{\mathrm{recruiter\ (non\text{-}J_{rel})}}^{\mathrm{wave}} &= \Delta^{+}N_{\mathrm{recruiter\ (non\text{-}J_{rel})}}^{\mathrm{wave}} - \Delta^{+}N_{\mathrm{refractory}}^{\mathrm{wave}} \\
\Delta N_{\mathrm{refractory}} &= -\Delta^{+}N_{\mathrm{available}} + \Delta^{+}N_{\mathrm{refractory}}^{\mathrm{trig}} \\
&\quad + \Delta^{+}N_{\mathrm{refractory}}^{\mathrm{spont}} + \Delta^{+}N_{\mathrm{refractory}}^{\mathrm{wavelet}} \\
&\quad + \Delta^{+}N_{\mathrm{refractory}}^{\mathrm{wave}}
\end{aligned}$$

Table 2. List of control parameters and their implications. Note that the half-maximal activation constants, the gradients and the thresholds are dimensionless because they are relative to the normalised I_{CaL} or Ca_{SR} values.

	Parameter	Units	Grandi atria	Grandi ventricle	CRN atria	Functional implications
Model fitting	$I_{CaL}^{\text{peak normal pacing}}$	pA/pF	−8.5	−2.25	−4	Model fitting (I_{CaL} dependence)
	$Ca_{SR}^{\text{diastolic normal pacing}}$	mM	0.5	0.55	1.1	Model fitting (Ca_{SR} dependence)
	$N_{RyR2o_{rescale}}$	—	0.00342965	0.0064	0.075	Model fitting (J_{rel} magnitude)
	$t_{wavedelay}$	ms	10	10	10	Defines β and sets recruitment speed
	$t_{J_{rel}}$	ms	40	30	15	Defines γ and J_{rel} active time
	$t_{recruit}$	ms	41	40	40	Defines δ and total recruiter time
Triggered sparks	C_{α}^{trig}	ms^{-1}	0.09	0.05	0.15	Triggered spark activation rate constant
	k_{ICaL}^{trig}	—	−0.25	−0.4	−0.35	Gradient parameter (I_{CaL} dependence)
	k_{CaSR}^{trig}	—	−0.375	−0.5	−1.5	Gradient parameter (Ca_{SR} dependence)
	$Ca_{SR_{50}}^{trig}$	—	1.5	1.5	1.5	Half maximal activation constant (Ca_{SR})
Spontaneous sparks	C_{α}^{spont}	ms^{-1}	0.000002	0.000002	0.000002	Spontaneous spark activation rate constant
	k_{CaSR}^{spont}	—	−0.1	−0.1	−0.2	Gradient parameter (Ca_{SR} dependence)
	$Ca_{SR_{50}}^{spont}$	—	1.5	1.5	2.5	Half maximal activation constant (Ca_{SR})
Wavelet sparks	$C_{\alpha}^{wavelet\text{-}trig}$	ms^{-1}	0.01	0.01	0.01	Rate constant (activation from triggered)
	$C_{\alpha}^{wavelet\text{-}spont}$	ms^{-1}	0.005	0.005	0.005	Rate constant (activation from spontaneous)
	$C_{\alpha}^{wavelet\text{-}wavelet}$	ms^{-1}	0.01	0.01	0.01	Rate constant (activation from wavelet)
	$k_{CaSR}^{wavelet}$	—	−0.5	−0.75	−2.0	Gradient parameter (Ca_{SR} dependence)
	$Ca_{SR_{50}}^{wavelet}$	—	1.5	1.5	1.5	Half maximal activation constant (Ca_{SR})
	$Ca_{SR_0}^{wavelet}$	—	0.5	0.3	0.1	Wavelet activation threshold
Wave sparks	C_{α}^{wave}	ms^{-1}	0.00004	0.00004	0.00004	Wave activation rate constant
	k_{CaSR}^{wave}	—	−0.2	−0.2	−0.5	Gradient parameter (Ca_{SR} dependence)
	$Ca_{SR_{50}}^{wave}$	—	1.2	1.18	1.27	Half maximal activation constant (Ca_{SR})
	$Ca_{SR_0}^{init,\ wave}$	—	0.9	0.9	0.9	Wave initiation threshold
	$Ca_{SR_0}^{prop,\ wave}$	—	0.7	0.5	0.1	Wave self-propagation threshold

Integration into biophysically detailed models

This formulation introduces a set of physiologically grounded control parameters that can be tuned to different cell models or experimental conditions. The most important of these parameters are summarised in Table 2, and the full parameter list is in Table A1.

Coupling between the spark-population model and host cell models. The spark-population model was integrated into contemporary cell models through replacing the RyR2 model that governs intracellular calcium release, J_{rel}. Three cell models were chosen: The Grandi et al. (2010) model of the human ventricle and Grandi et al. (2011) human atrial model were chosen due to their detailed and robust intracellular calcium handling system, referred herein as Grandi ventricle and Grandi atria. The Courtemanche et al. (1998) atrial cell model ('CRN' model) was chosen as an alternative model which is widely used for studies of human atrial tissue dynamics. It features a simplified calcium-handling system with markedly different behaviour from the Grandi models, providing a useful contrast for assessing model integration.

Activation rates in the spark-population model were set such that approximately 50% of CRUs became activated during basal pacing at full t-system density. This corresponds to a peak value of roughly 0.5 for the RyR2 open-state variable, which may differ from the peak RyR2

open proportion in the original cell models. To maintain the correct magnitude of J_{rel}, a scaling factor $N_{RyR2o_{rescale}}$ was introduced to adjust the resultant release flux to match the expected dynamics of each host model. J_{rel} in the host cell model is therefore calculated by:

$$J_{rel} = g_{rel} N_{RyR2o_{rescale}} \frac{N^{tot}_{excited} + N^{tot}_{recruiter\ (J_{rel})}}{N_{tot}} (Ca_{SR} - Ca_i)$$

where

$$N^{tot}_{excited} = N^{trig}_{excited} + N^{spont}_{excited} + N^{wavelet}_{excited} + N^{wave}_{excited}$$

$$N^{tot}_{recruiter\ (J_{rel})} = N^{trig}_{recruiter\ (J_{rel})} + N^{spont}_{recruiter\ (J_{rel})} + N^{wavelet}_{recruiter\ (J_{rel})} + N^{wave}_{recruiter\ (J_{rel})}$$

g_{rel} refers to the conductance parameter and the specific variables for Ca_i and Ca_{SR} will depend on the host cell model. Only a basic parameterisation was performed in this study for integration with the three cell models, aimed at reproducing normal cell behaviour observed in the original cell models, with a focus on maintaining Ca_{SR} load under basal pacing conditions.

Initial model parameterisation. A full practical guide to parameterisation of the spark-population model for integration in contemporary cell models accompanies the source code in the related Zenodo repository. Briefly, parameterisation was performed using an ad hoc optimisation procedure. The basal cell models were first paced to steady state to determine the characteristic I^{peak}_{CaL}, $Ca^{diastolic}_{SR}$, $N^{peak}_{RyR,O}$ and the J_{rel} time course. These quantities define the normalisation variables, the rescaling factor ($N_{RyR2o_{rescale}}$) and the J_{rel} decay time parameters. The modified model was then paced, and parameters were adjusted to give the peak proportion of active CRUs during CICR as approximately 0.5 while preserving the J_{rel} time course and Ca_{SR} dynamics observed in the basal model, through tuning the LTCC sensitivity and J_{rel} kinetics. Spontaneous spark and wave propagation rates, together with their steepness, were subsequently adjusted to reproduce expected or experimentally observed behaviour.

Because the formulation is expressed in terms of normalised Ca_{SR}, the gradient parameters are expected to be broadly similar across models, but should be set to reflect the underlying basal dynamics corresponding to the extent of SR depletion during CICR and the degree of SR loading under different conditions. Models exhibiting limited SR depletion and relatively small load variation require a steeper gradient, reflecting the narrow operating range of Ca_{SR}, whereas models with larger depletion and wider load variation require a shallower gradient to represent the broader concentration range. These parameters are therefore constrained by the intrinsic model dynamics and determine the imposed rate-dependent behaviour. This process is somewhat subjective and should be informed/constrained by all available information, such as spark and wave rates at different pacing frequencies and conditions.

The parameters (Table 2) were chosen to ensure calcium handling properties remained within physiological ranges and comparable to the original models. These values are sufficient for demonstrating the mechanistic operation of the spark-population model presented. It is intended that future applications of this model will develop the various parameters based on experimental observations (such as calcium transient amplitude, spark and wave rates, etc.) or 3D spatial cell simulations in specifically focused studies. Modification of the parameters to reproduce disease conditions is considered further in **Discussion – Modelling regulation of calcium handling**, with 'toy' disease conditions considered in the results section to demonstrate the impact of the modification of parameters.

The intention was to avoid having to modify any parameters of the original, host models. However due to differences in the time of the upstroke of the calcium transient observed between the original and spark-population implementation of the Grandi models (see **Results – 'Integration into the three biophysically detailed cell models'**) it was necessary to slightly reduce the rate constant that governs calcium-induced inactivation of I_{CaL}. No other modifications were performed.

Variable t-system density

Variable t-system density was implemented by constructing two parallel populations encompassing the full CRU state cycle: one coupled to the t-system and one uncoupled. This required the modification of the host cell models to include a second set of calcium compartments associated with the non-t-system population. These additional compartments retained all SR fluxes from the original model but excluded membrane fluxes. Calcium concentrations in the bulk cytosolic space and the network SR were coupled between the two sets of compartments, but the recruitment of CRUs through the spark-population model provided the primary mechanism for calcium-wave propagation into non-t-system regions. Coupling between the two populations was achieved through the ability of recruiter CRUs in either population to activate new wavelet CRUs in the other.

The relative sizes of the t-system and non-t-system populations were determined by the number of interior CRUs and the specified t-system density. First the number of surface and interior CRUs were calculated from the cell dimensions. The t-system density, which

varies between 0 and 1, then defined the proportion of interior CRUs coupled to the t-system. Note that this definition does not numerically correspond to experimental estimates of t-system density derived from pixel-based area or volumetric analysis, as it is at the scale of a CRU. The total t-system population is given by the sum of surface CRUs and the proportion of interior CRUs defined by the t-system density, with the remainder assigned to the non-t-system population. The present formulation does not distinguish between surface and interior CRUs coupled to the membrane; however, such differentiation could readily be introduced in future implementations by defining a third population representing surface-membrane CRUs.

Results

Integration of the spark-population model into biophysically detailed cell models is first demonstrated. Dynamics associated with variable t-system density are then examined and compared with experimental observations under different conditions. Finally the mechanisms underlying calcium transient alternans and the hierarchy of spontaneous calcium release are explored, including the influence of t-system density on these phenomena.

Integration into the three biophysically detailed cell models

Under I_{CaL} voltage clamp (holding potential of −80 mV, stepped to test voltages for 500 ms and returned to −80 mV), the relationship between I_{CaL} and intracellular calcium release in the models is revealed. The spark-population implementation reproduced the basal Ca_{SR} dependent J_{rel}-I_{CaL} relationship observed in the original cell models (Fig. 3). One notable difference was that in the Grandi models, the fraction of open RyR2s is small, providing substantial reserve for larger responses at elevated Ca_{SR} loads. In contrast the spark-population model exhibits approximately 50% CRU activation at basal values, resulting in less dynamic range for further increases (Fig. 3*c*, upper vs lower panels).

AP and intracellular calcium transient features during normal pacing were well preserved following the integration of the spark population dynamics model (Fig. 4). In both Grandi-based models the primary difference was a more immediate J_{rel} response to I_{CaL}, producing an earlier calcium transient upstroke (Fig. 4*Ac,d, Bc,d*). The delayed onset of J_{rel} in the original models has been noted as a limitation (Tomek et al., 2025), and therefore this was not corrected for in the spark-population model. Rate dependence of the calcium transient and Ca_{SR} load were also largely preserved in the updated models (Fig. 4*e–h*). Importantly no major differences were observed in diastolic or post-pacing Ca_{SR} between the models, indicating that any parameters based on the range of Ca_{SR} will remain suitable (Fig. 4*f,h*). It is worth noting that the CRN model exhibits the opposite rate dependence of the calcium transient peak than the Grandi models in both the original and updated cell models.

Computational efficiency was modestly reduced in the spark-population implementation relative to the basal cell models, remaining within the range typical for single-cell simulations. The time required to compute one simulated second increased from 0.04 s to 0.10 s in the CRN atrial cell model, from 0.06 s to 0.16 s in the Grandi atrial cell model, and from 0.15 s to 0.33 s in the Grandi ventricular cell model, corresponding to an approximately 2-2.5-fold increase in cost. This remains substantially more efficient than a stochastic, spatial 3D cell model that may contain 20,000 explicitly described CRUs, with an average of 100 RyRs and 15 LTCCs each, which was four orders of magnitude slower when executed on a single core (1428 s per simulated second). This comparison is particularly relevant for tissue-scale simulations, in which parallelisation is applied across cells rather than within the subcellular spatial domain.

Spark model state occupancy

Inspection of CRU population state occupancies highlights the underlying dynamics of the spark-population model system (Fig. 5). The three models represent the range of ways that the duration of J_{rel} can be varied to fit within the contextual calcium handling system of each cell model. Recall (**Methods – 'Spark-population model states'**) that the J_{rel} activity time course must fit within the lower limit of the 'wave delay' (the time to transition from excited to recruiter state; time fixed to 10 ms in the present study) and the upper limit of the total time that sparks are able to recruit (time fixed to 40 ms in the present study), but may be freely varied within this range. This produces three characteristic behaviours:

(1) J_{rel} decay time is comparable to the total active time, in which case the model will very rapidly transition through the recruiter (non-J_{rel}) state to the refractory state, as in the Grandi atrial model (Fig. 5*Aa*).
(2) J_{rel} decay time lies centrally within the range, in which case the model spends comparable time in both recruiter (J_{rel}) and (non-J_{rel}) states, as in the Grandi ventricle model (Fig. 5*Ab*).
(3) alternatively, the J_{rel} decay time can be comparable to the wave delay time, in which case the model will rapidly transition through the recruiter (J_{rel}) state to

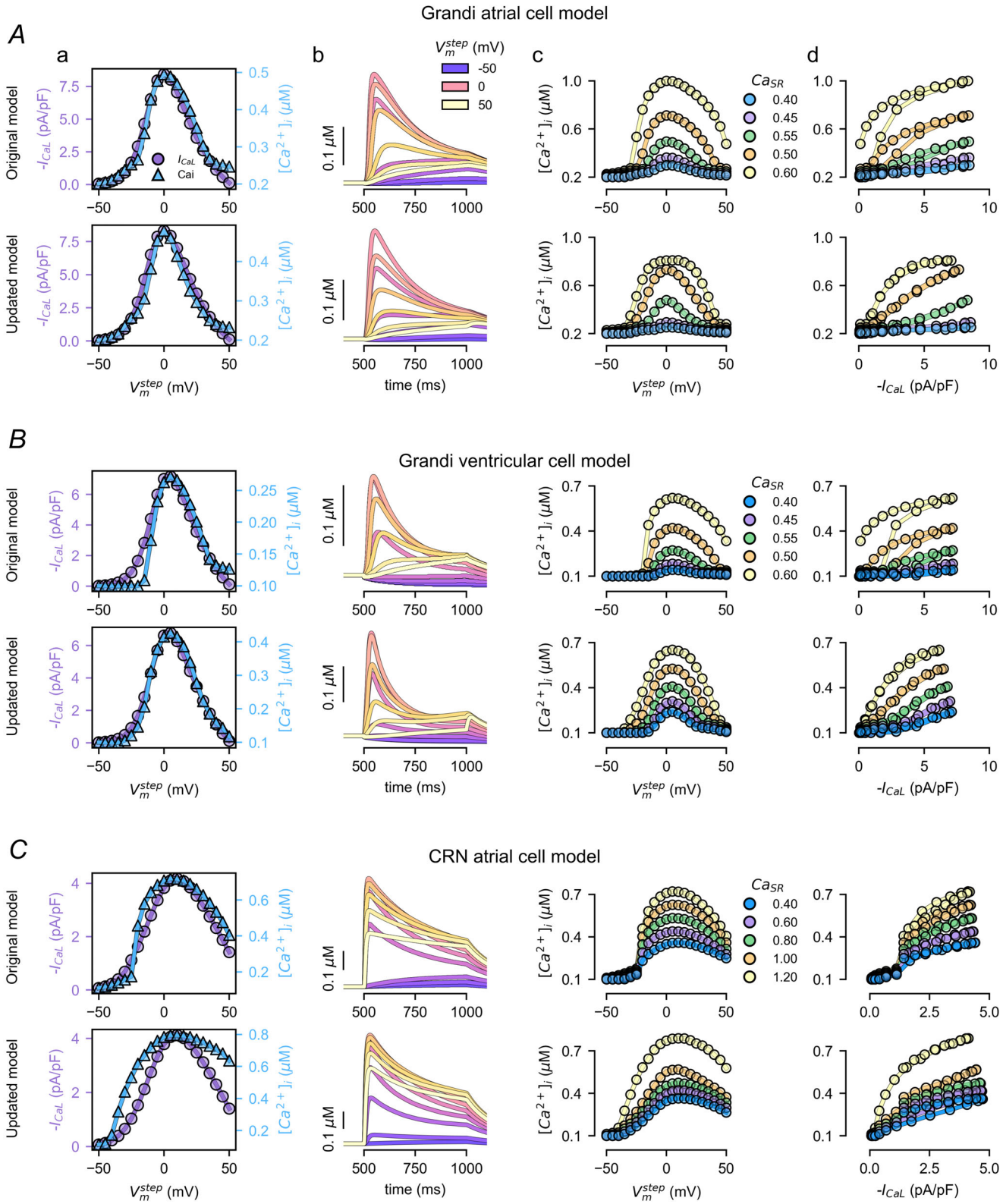

Figure 3. Comparison of response to I_{CaL} voltage clamp between the original and updated cell models. For the three cell models (*A*, Grandi atria; *B*, Grandi ventricle; *C*, CRN atria) are shown I_{CaL} current–voltage relationships and corresponding intracellular calcium transient peak (*a*), calcium transient traces across the range of voltage steps (*b*) and calcium transient magnitude as a function of voltage step potential (*c*), and I_{CaL} peak (*d*) at multiple Ca_{SR} loads.

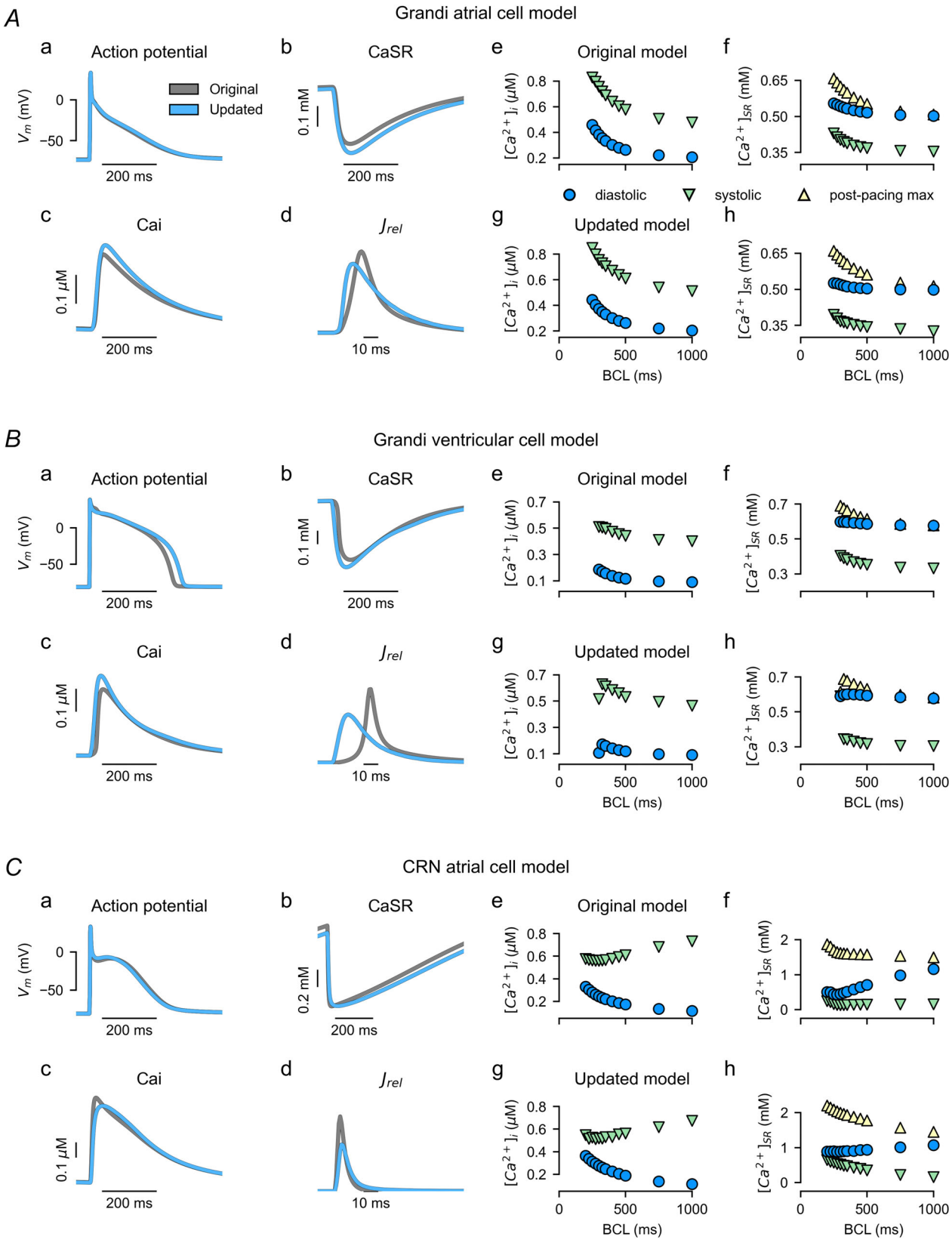

Figure 4. Comparison of model behaviour during normal pacing.
For the three cell models (*A*, Grandi atria; *B*, Grandi ventricle; *C*, CRN atria) are shown the APs (*a*), Ca_{SR} and calcium transients (*b,c*), J_{rel} time course (*d*), and rate-dependence of the intracellular (*e, g*) and Ca_{SR} (*f, h*) dynamics for the original and updated (spark-population) models.

the recruiter (non-J_{rel}) state, as in the CRN model (Fig. 5*Ac*).

Across all models, the total active profile has similar duration and peaks at approximately half of the total population. The occupancies also reveal the small contribution of diffusively activated CRUs (wavelets) during normal pacing (Fig. 5*B*) and the presence of spontaneous calcium sparks mediated by the spontaneous and wavelet populations (Fig. 5*B*, inset).

Variable t-system density

Simulations were first performed using parameters that produced robust propagation of calcium into non-t-system regions, consistent with the centripetal 'U' or 'V' waves observed experimentally in the absence of interior t-system (Brette et al., 2004; Dibb et al., 2022; Greiser et al., 2014; Greiser, 2017). Coupling between the t-system and non-t-system populations, described by the rate constants for non-t-system wavelet CRUs to be activated by t-system CRUs, was identical across all three cell models. In these simulations t-system density determined the whole-cell calcium transient upstroke and amplitude (Fig. 6*a,e*): as density decreased from 1.0 to approximately 0.5, the magnitude of the whole-cell-averaged transient was largely preserved, whereas the time to peak increased; as t-system density was further reduced below 0.5 towards zero, the transient amplitude progressively decreased and the time to peak increased further.

Examination of CRU dynamics in the t-system and non-t-system populations (Fig. 6*b–d*) shows that active CRU propagation in the non-t-system region underlies the slower upstroke and smaller amplitude of the whole-cell transient (Fig. 6*b*). Total CRU activation was largely maintained at moderate reductions of t-system density, and decreased by a small degree at low densities (Fig. 6*c,d*, inset); this reflects whole-cell activation associated with robust U- and V-wave propagation. For comparison, simulations were performed with the coupling between t-system and non-t-system populations reduced to 50% and 0%, demonstrating whole-cell calcium transients in the absence of effective centripetal wave propagation (Fig. 6*e*). In these cases time to peak was largely insensitive to t-system density, whereas the amplitude progressively declined as density was reduced.

Model behaviour under different conditions was compared with experimental observations of calcium handling in myocytes with reduced or absent t-system. A primary motivation for this model is to be able to capture the variable t-system density in healthy atrial cells. Experiments by Greiser et al. (2014) observe robust centripetal U wave propagation in transverse linescan calcium imaging (Fig. 7*A*). Under the default parameters (as used in the previous Fig. 6) the spark-population

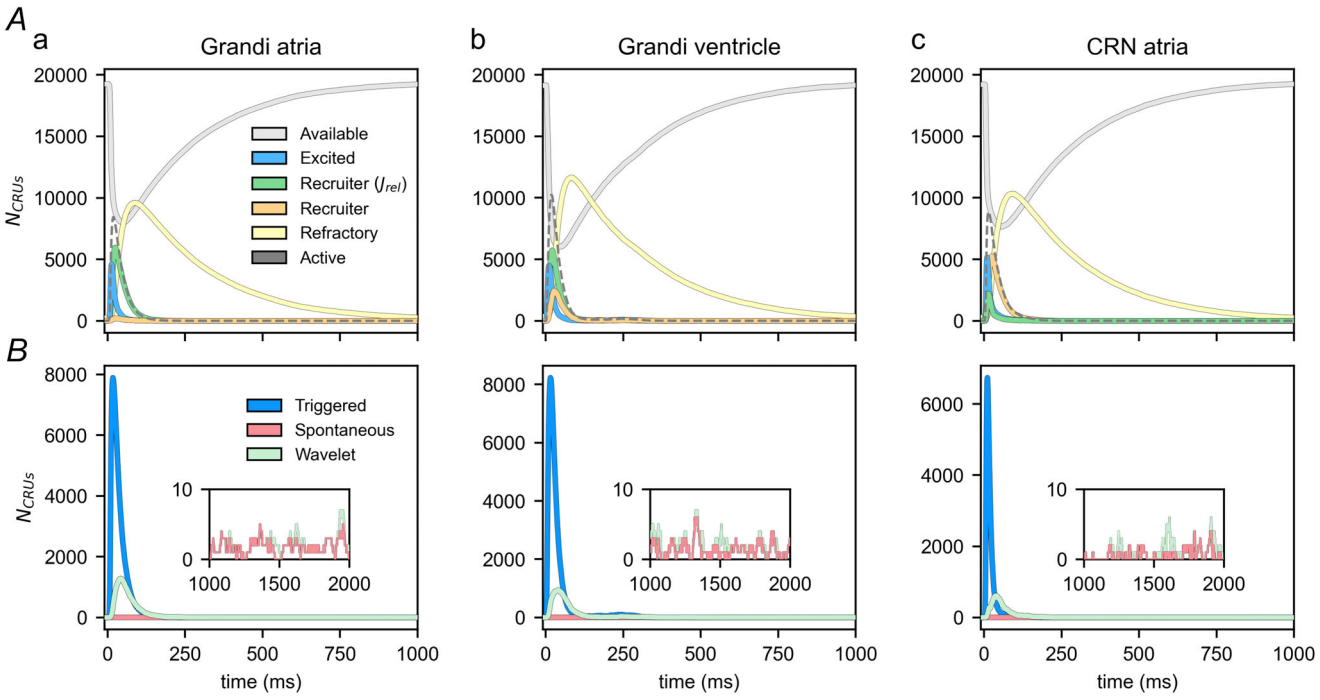

Figure 5. CRU state occupancy.
A, Occupancy of the different states, shown for the three different cell models *(a–c)*. Note that 'active' (grey dotted line) is considered as the total Excited+Recruiter(J_{rel})+Recruiter(non-J_{rel}) occupancy. *B*, the active occupancy for each type of spark.

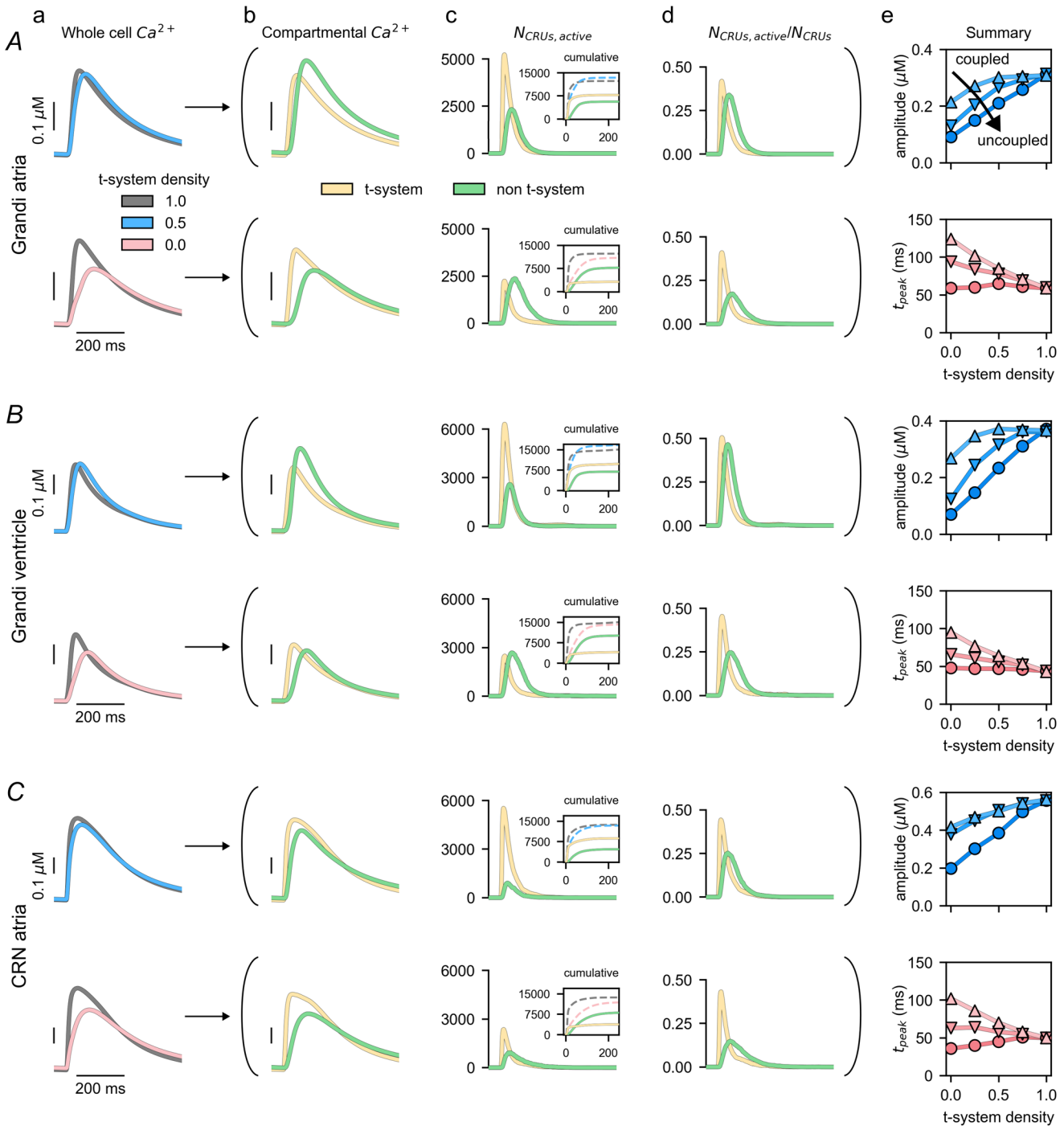

Figure 6. Calcium transient features versus t-system density with robust centripetal calcium propagation.
For the three cell models (*A*, Grandi atria; *B*, Grandi ventricle; *C*, CRN atria) is shown the whole-cell average calcium transient (*a*), associated with 50% (blue, upper) and 0% (pink, lower) t-system density compared to the control case of 100% t-system density (grey), and separated population traces for the average compartmental calcium (*b*), total number of active CRUs in each population (*c*), and proportion of active CRUs relative to the size of each population (*d*), illustrating t-system (yellow) and non-t-system (green) CRUs. The dependence of the total upstroke time and amplitude of the calcium transient on t-system density is summarised (*e*) across a range of densities (0%, 25%, 50%, 75% and 100%) and strength of coupling between the t-system and non-t-system CRUs (darker shades indicate lower coupling).

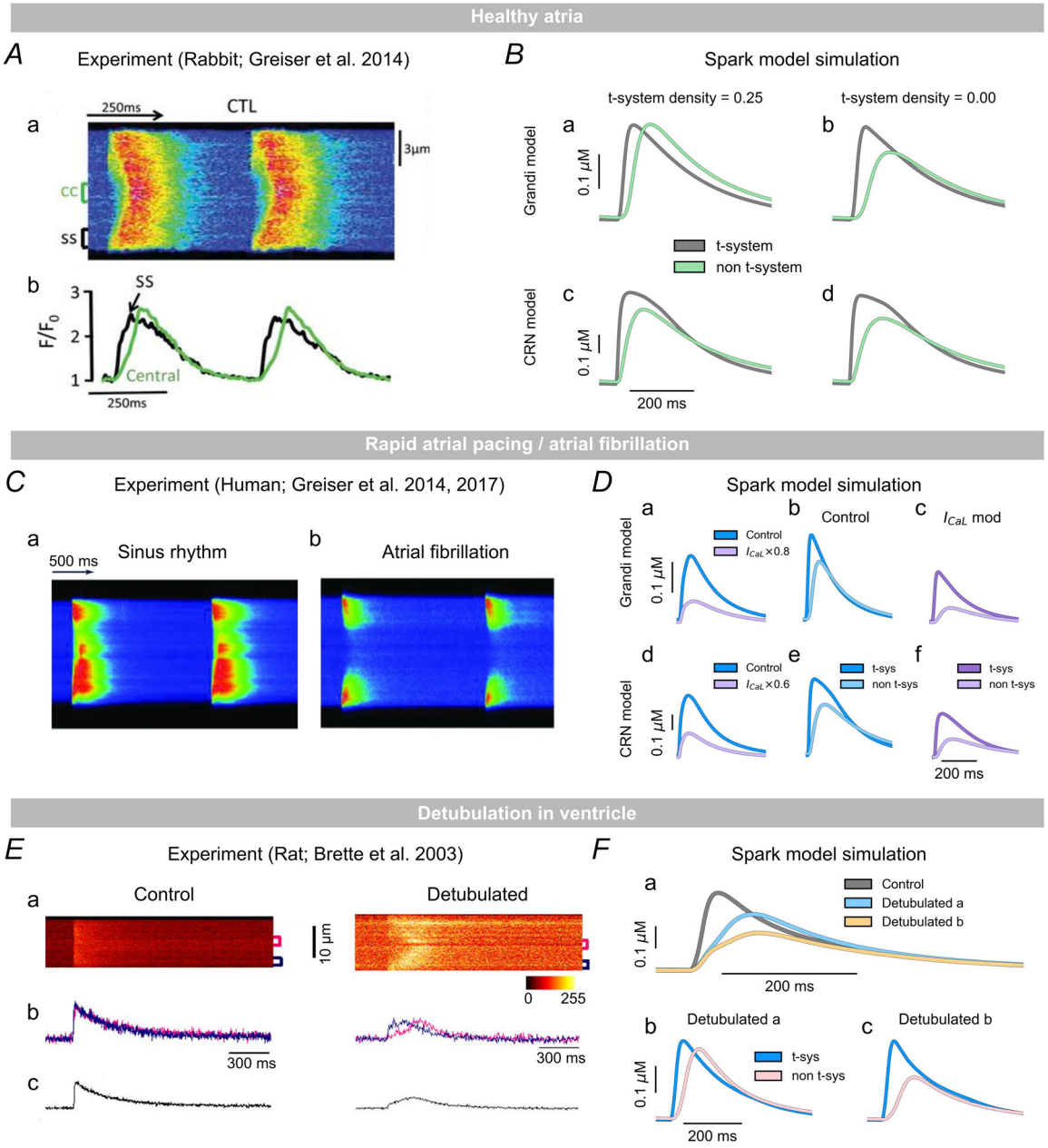

Figure 7. Modelling variable t-system density features compared to experimental observations.
A, Experimental observations of healthy atrial myocytes with low t-system density. Transverse linescans (*a*) reveal the 'U' centripetal wave and highlight the morphology of the calcium transient at surface and interior sties (*b*). Images from Greiser et al. (2014) and reproduced under the CC BY 4.0 license. *B*, Model comparisons of the average calcium transient in the t-system (black) and non-t-system (green) compartments at two different t-system densities (25% and 0%) in both the Grandi (*a,b*) and CRN (*c,d*) atrial models. *C*, Experimental linescan images highlighting calcium silencing (failed centripetal wave propagation) in human atrial fibrillation. Images from Greiser (2017) reproduced with permission, copyright Wiley 2017. *D*, illustration in the reduced computational cell model. A reduction in I_{CaL} was used to represent the downregulation of the current in atrial fibrillation. Whole-cell average transient is shown (*a,d*) for control and remodelling (blue vs purple, respectively) as well as the compartmental calcium transients corresponding to the t-system and non-t-system (dark vs. bright) for control (*b,e*) and remodelling (*c,f*). *E*, Experimental linescan (*a*), local calcium (*b*) and whole-cell (*c*) calcium traces associated with control and detubulated ventricular cells. Images from Brette et al. (2004) and reproduced with permission; copyright Elsevier 2004. *F*, Results in the computational model showing whole-cell average calcium transient (*a*) and compartmental transients in two different models of detubulation: 'detubulation a' refers to simply setting the t-system density to 0 (*b*) whereas in 'detubulation b' the coupling between the t-system and non-t-system was also reduced by 50% (*c*).

model reproduced the observed features, with the calcium transients in the t-system and non-t-system populations being comparable to those at the surface and centre of the linescan (Fig. 7*A*,*B*). They are not a direct correspondence of measurements, as the model traces represent the average transient in each population rather than specific locations of the cell. Nevertheless, the feature of the delayed interior (non-t-system) transient is captured in the model at low t-system densities.

In further experiments (Greiser et al., 2014; Greiser, 2017), atrial rapid pacing and atrial fibrillation, both associated with a reduction of I_{CaL} magnitude, were observed to result in failed centripetal propagation of the calcium transient (Fig. 7*C*). Under comparable conditions in the model (reduced I_{CaL} conductance), recruitment of non-t-system CRUs was markedly diminished, reproducing the failed propagation and resulting in a reduced whole-cell average transient (Fig. 7*D*). The transition rates coupling the t-system and non-t-system populations were reduced by half to generate failed propagation to the extent observed in the experiment; this could reflect structural remodelling or the need for further refinement or a limitation of the models.

In ventricle, loss and remodelling of the t-system has been associated with multiple disease conditions (e.g. Setterberg et al., 2021) and manifests as a dyssynchronous calcium release with a reduced transient and delayed upstroke (Fig. 7*E*; Brette et al., 2004). In the Grandi ventricular cell model, detubulation (i.e. setting the t-system density to 0%) produced the same behaviour. The strength of coupling between the t-system and non-t-system populations and the rate of wavelet self-recruitment determined the details of the dynamics observed, but with the key macroscopic features preserved (Fig. 7*F*).

Beat-to-beat variability and alternans

Beat-to-beat variability was observed in the updated models during both normal and rapid pacing due to the stochastic algorithm and non-linearities in the activation transition rate functions. Examination of the dependence of the calcium transient amplitude at beat, n, on the previous beat ($n-1$), highlights the degree and regularity of this beat-to-beat variability. Simulations were first performed with the activation rates of spontaneous and wavelet sparks set to zero, that is, to isolate the dynamics emerging from the LTCC-triggered calcium sparks only. The Grandi-based models exhibited greater variability than the CRN model (Fig. 8*A*). For interpretation of this figure, recall that the CRN and Grandi models produce the opposite rate dependence of calcium transient amplitude (Fig. 4). In all cases the original deterministic models showed no beat-to-beat variability.

Calcium-transient alternans emerged following multiple insults, including the downregulation of SERCA in the host cell model (Fig. 8*Ba*) and altered steepness of the I_{CaL} and Ca_{SR} dependent activation functions for triggered CRUs (Fig. 8*Bb–d*). Across a range of parameters, multiple behaviours were observed, including typical robust 2-cycle alternans at fast rates (Fig. 8*Ba, Cb*), intermittent, unstable small alternans (Fig. 8*Bb*, *Ca*), stable 3- and 4-cycle alternans (Fig. 8*Bc*, *Cc*) and semi-stable more complex patterns, such as one that exhibited a generally 7-beat cycle (Fig. 8*Bd*, *Cd*).

Restoring calcium propagation (i.e. enabling the wavelet activation rate) also produced a variety of dynamics. The impact on beat-to-beat variability was only small (Fig. 9*A*). In some conditions alternans persisted with similar dynamics to the triggered-only case (Fig. 9*Ba*); in others the specific alternans patterns were modulated (Fig. 9*Bb*); whereas in others spatial recruitment was protective against the development of regular alternans (Fig. 9*Bc–d*). Under conditions with substantial recruited-spark contributions during normal pacing (i.e. large wavelet activation rates), the model exhibited disordered and chaotic calcium dynamics. However these are likely non-physiological conditions and are not shown here. Future studies, if justified, may want to explore this further.

Cells with low t-system density displayed more complex, noisy and irregular rate-dependent responses compared to those with a dense t-system (Fig. 10), with less ordered and more chaotic patterns across models and conditions. Generally the t-system and non-t-system populations oscillated in amplitude together, although not always synchronously. Low t-system density also enabled alternans at relatively slow pacing rates (e.g. Fig. 10*Ab,c*).

Delayed calcium sparks

Recent experiments (e.g. Fowler et al., 2022) have observed late calcium sparks, that is, those occurring after the primary calcium transient upstroke (Fig. 11*A*). In a series of elegant experiments, it was demonstrated that inhibiting the transient outward current (I_{to}) via dynamic clamp elevated the plateau potential, reduced the peak I_{CaL}, induced dyssynchronous initial calcium release and increased the frequency of delayed calcium sparks that prolonged the calcium transient (Fig. 11*B*). This behaviour was reproduced in the model by setting I_{to} conductance to 0, representing complete dynamic-clamp cancellation, and to negative values, representing potential overestimation of the current cancellation by imposing an inverted current with the same kinetics. The latter adjustment was primarily intended to reproduce the experimentally observed difference in AP morphology which determines the I_{CaL} profile and subsequent

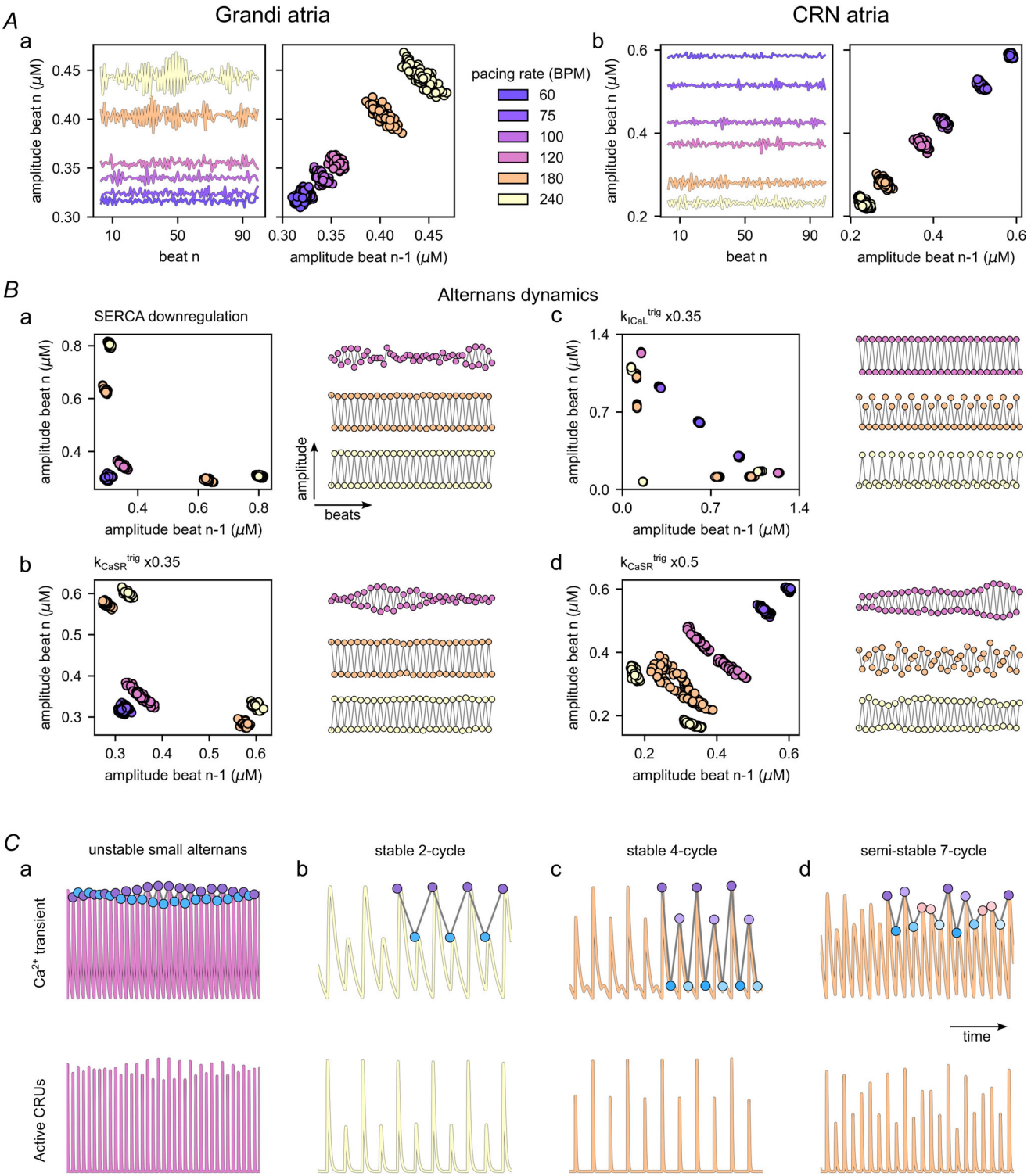

Figure 8. Beat-to-beat variability and alternans without spatial calcium coupling.
A, variability during normal pacing in the Grandi atria (*a*) and CRN atria (*b*) models. The amplitude of the intracellular calcium transient at each beat is shown (left) and the summary of the amplitude of beat n versus amplitude of beat ($n-1$) (right). The colour scheme refers to the applied pacing rate and is consistent throughout the figure. *B*, examples of different alternans dynamics under different conditions, showing the beat n vs beat ($n-1$) summary (left) as well as an extracted plot of beat-by-beat amplitude (right). Note that these panels are scaled to the range observed in each individual condition/pacing rate, and so the magnitudes are not comparable between panels. *C*, example intracellular calcium transients and active CRU traces illustrating different behaviour.

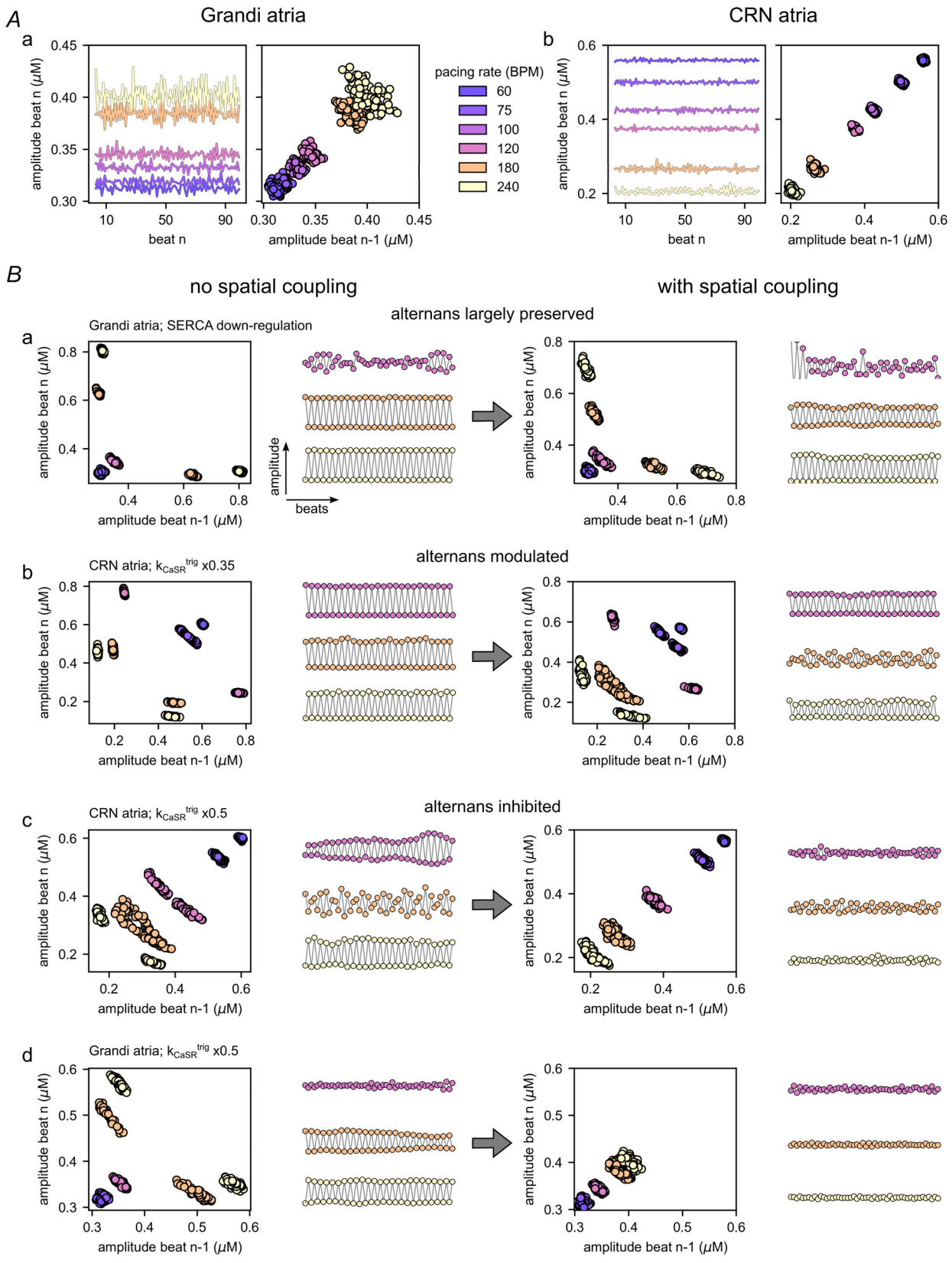

Figure 9. Beat-to-beat variability and alternans with spatial calcium coupling included.
A, variability during normal pacing in the Grandi atria (*a*) and CRN atria (*b*) models with the wavelet propagation rates set to the basal values. The colour scheme refers to the applied pacing rate and is consistent throughout the

figure. *B*, examples of alternans dynamics compared between the cases of no spatial coupling (left) and included spatial coupling (right).

triggered calcium spark dynamics. The same mechanisms observed experimentally were reproduced by the model (Fig. 11*C*): the calcium transient peak was reduced and delayed relative to control, a greater number of triggered sparks occurred during the late AP phase, and both the whole-cell calcium transient and AP duration were prolonged.

Spontaneous calcium release hierarchy and triggered APs

The hierarchy of spontaneous calcium release was reproduced through the dynamics of the spontaneous, wavelet and wave spark populations (Fig. 12). The Grandi ventricle model was paced to steady state at a cycle length of 400 ms, and the resulting state parameters were used as initial conditions for spontaneous simulations. This provides a single Ca_{SR} load to provide the baseline for varying the rate constants and function parameters for the spontaneous, wavelet and wave spark activation mechanisms. A single stimulus was applied, after which the model was allowed to run for 10 s and the spontaneous activity measured.

With the inclusion of spontaneous activation only (i.e. transition rates for wavelet and wave sparks set to zero), transient spontaneous activity occurred immediately following the AP, when the Ca_{SR} first loads above the release thresholds, before being subsequently depleted due to leak mediated by this release. Thereafter the system stabilised with a consistent spontaneous spark rate (Fig. 12*Aa*, *Ba*).

Inclusion of wavelet sparks produced a continuum of behaviours ranging from short-lived spontaneous activity (Fig. 12*Bb*) similar to the spontaneous-only conditions (but occurring at lower rate constants) to DADs and fully triggered spontaneous APs (Fig. 12*Bc–e*). DADs and spontaneous APs always followed directly after the paced AP, emerging only at the highest Ca_{SR} loads before depletion by calcium leak. Negative shifts applied to the $Ca_{SR_{50}}$ of spontaneous and wavelet CRU activation produced substantial spontaneous release during the AP, underpinning a range of EAD dynamics including low-upstroke EADs and APD prolongation (Fig. 12*Bf*), phase 3 EADs (Fig. 12*Bg*) and oscillatory phase 2 EADs followed by DADs (Fig. 12*Bh*; Johnson et al., 2013). Large spontaneous transients were never observed substantially delayed from the stimulated AP.

The inclusion of full-cell calcium waves enabled spontaneous transients underlying DADs or triggered APs to occur over a much broader range of latency times (Fig. 12*C*). This is a consequence of the all-or-nothing nature of full-cell wave initiation. At equilibrium the number of active spontaneous and wavelet sparks may be low, but this still yields a non-zero probability of initiating a full-cell wave, depending on the relation between the wave initiation threshold parameter ($Ca_{SR_0}^{init,\ wave}$) and the Ca_{SR} load. Thus calcium waves underlying DADs could occur well after the stimulated AP, emerging from a background of relatively few active wavelet CRUs (Fig. 12*Ca*). Full-cell calcium waves could also be initiated during the large transient of spontaneous and wavelet sparks immediately after the AP (Fig. 12*Cb*); the high active wavelet population could initiate multiple calcium waves in rapid succession. These waves rapidly self-terminated, producing a large spontaneous calcium transient and a triggered AP.

Dynamic dependence of spontaneous calcium release

The dependence of spontaneous calcium release on Ca_{SR} load was first examined. The Grandi ventricle cell model was pre-paced at cycle lengths of 1000, 750, 500 and 400 ms and then left unstimulated for 2 s for the Ca_{SR} to fully load. The spontaneous spark activation rate was set to zero to prevent spontaneous release, leading to Ca_{SR} values of 0.58, 0.60, 0.63 and 0.66 mM, respectively. The state variables were saved and used as initial conditions to perform 250 simulations with the spontaneous spark rate on and no stimulated excitations applied (Fig. 13*A*). The incidence of DADs and triggered APs was increased at higher Ca_{SR} loads (Fig. 13*A*,*Ba*). For simulations exhibiting DADs or triggered APs, the time to peak voltage also showed clear Ca_{SR} dependence, with narrower and earlier latency time distributions at higher Ca_{SR} values (Fig. 13*Bb*). The spontaneous spark rate (measured as the rate of creation of spontaneous and wavelet sparks in the absence of full-cell calcium waves) also demonstrated a steep dependence on Ca_{SR} load with a substantially higher rate during the first 200 ms (corresponding to the initial release transient and unloading of the Ca_{SR}) than the next 1800 ms observed across all Ca_{SR} (Fig. 13*Bc*).

To illustrate the effects of enhanced calcium release, the protocol was repeated with parameters promoting full-cell calcium release (spontaneous spark rate constant, C_{α}^{spont}, and wave creation rate constant, C_{α}^{wave}, both multiplied by 100). These same Ca_{SR} levels may not be practically reachable with this increased calcium release, which would lead to substantial leak during pacing, but through this protocol we are able to compare behaviour at like-for-like Ca_{SR}. Under these parameters all simulations resulted in DADs with most resulting in triggered APs (Fig. 13*Ca*) and the latency time distributions were sub-

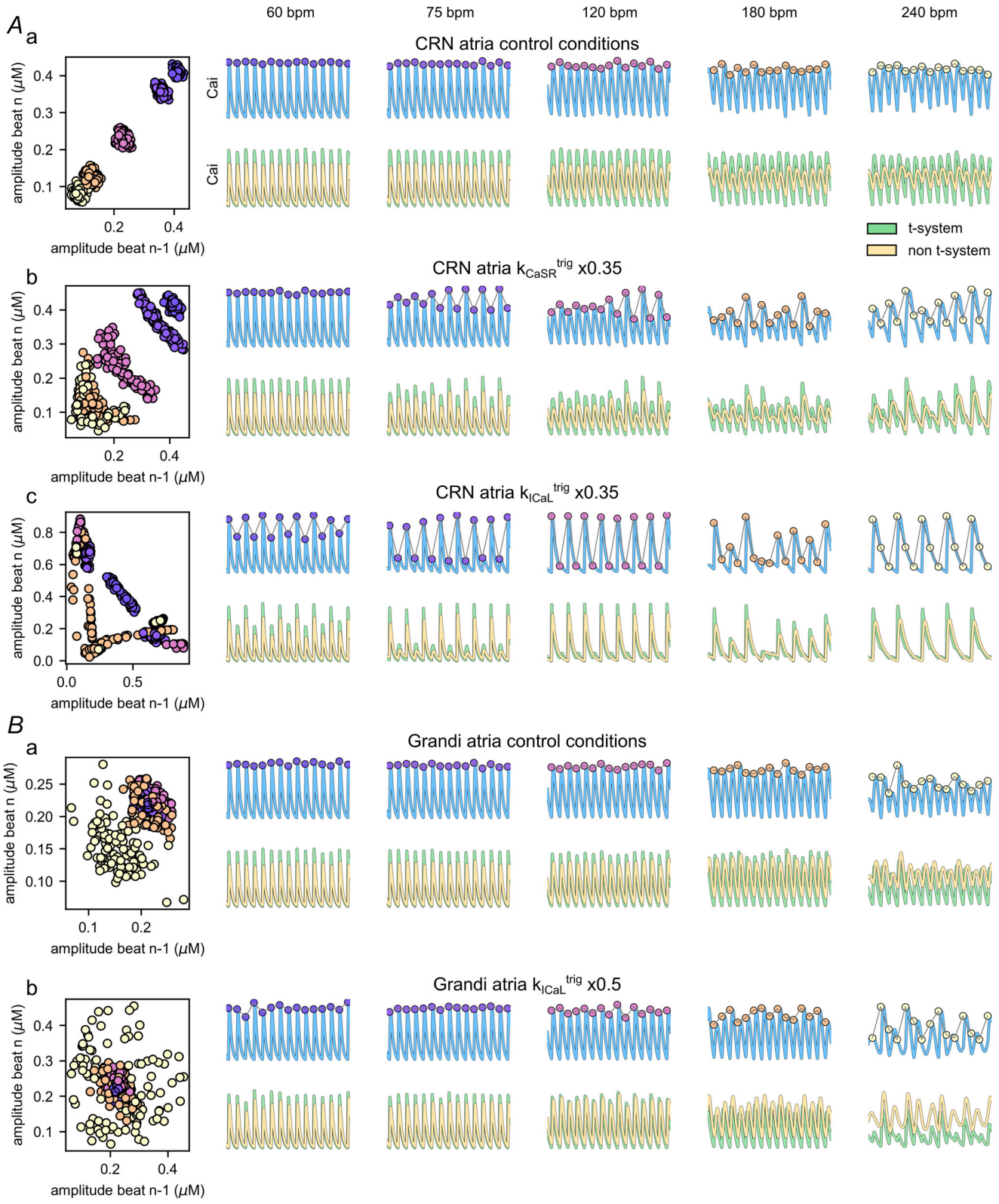

Figure 10. Beat-to-beat variability and alternans in cells without a t-system.
Whole cell average calcium (blue, upper) and compartmental calcium (green, orange, lower) transients during pacing at different cycle lengths and spark-population model parameters in the CRN (*A*) and Grandi (*B*) atria cell models.

stantially narrower and earlier (Fig. 13*Cb*), underpinned by an increase in the spark rate during the first 200 ms (Fig. 13*Cc*).

The interplay between pacing and spontaneous calcium release was further explored by pacing the models at various cycle lengths under various spontaneous-activity parameter combinations. Once steady state was achieved, five simulations were performed in which the models were paced for 100 cycles and then left to run without further applied pacing for 10 s. Under control conditions, both the CRN and Grandi atrial models showed a rate-dependence of post-pacing spontaneous release events: at slow pacing rates, few DADs or triggered APs were observed, across a broad range of latency times, whereas at higher pacing frequency, the propensity was enhanced (Fig. 13*D*,*E*). Very few triggered APs were observed under these control conditions, consistent with healthy myocytes.

The Grandi ventricle model was then used to demonstrate the combined effects of electrophysiological and spontaneous-release remodelling (Fig. 13*F*). At high pacing frequencies a small number of triggered APs were observed under normal conditions (Fig. 13*Fa*). Incorporation remodelling associated with heart failure (Gomez et al., 2014), which affected the host cell model but not the spark-population model, markedly increased triggered AP incidence (Fig. 13*Fb*). Increasing the propensity for spontaneous calcium release (C_{α}^{spont} and C_{α}^{wave} ×100) produced rapid triggered activity in the control model (Fig. 13*Fc*) and repeated spontaneous oscillations in the heart failure model (Fig. 13*Fd*).

Spontaneous calcium release also occurred during pacing, particularly at slow pacing frequencies where there is a sufficient diastolic interval for DADs and triggered APs to emerge. Under control conditions at 60 BPM occasional DADs (0.6% of beats; three events across 5 × 100-beat simulations) arose between elicited APs (Fig. 13*Ga*). The stimulated APs that followed a DAD typically showed an increased duration, consistent with

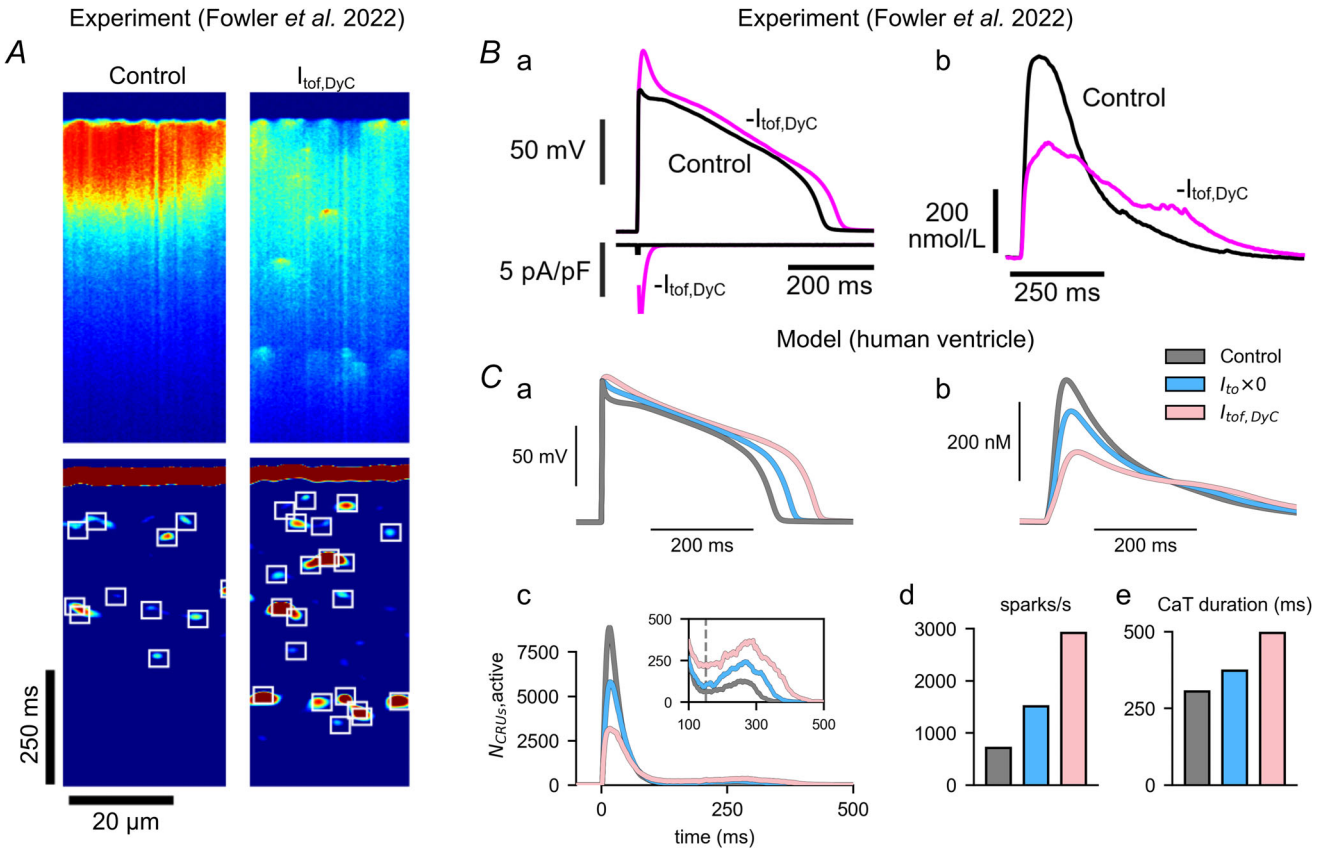

Figure 11. Delayed calcium sparks.
A, Experimental linescan images illustrating delayed calcium sparks occurring during the late phase of the AP under the intervention of dynamic clamp I_{to} ($I_{to,DyC}$). *B*, AP and calcium transient traces associated with control and $I_{to,DyC}$, illustrating the lower calcium transient amplitude and extended duration associated with delayed calcium sparks. *C*, Simulation reproducing the effect of $I_{to,DyC}$ also captures the enhanced delayed calcium sparks and associated calcium transient prolongation. Calcium spark rate (*d*) is measured from 125 ms after the AP upstroke, as indicated by the dotted line in the inset of *c*. Data from Fowler et al. (2022) reproduced with permission from original images sent by the authors.

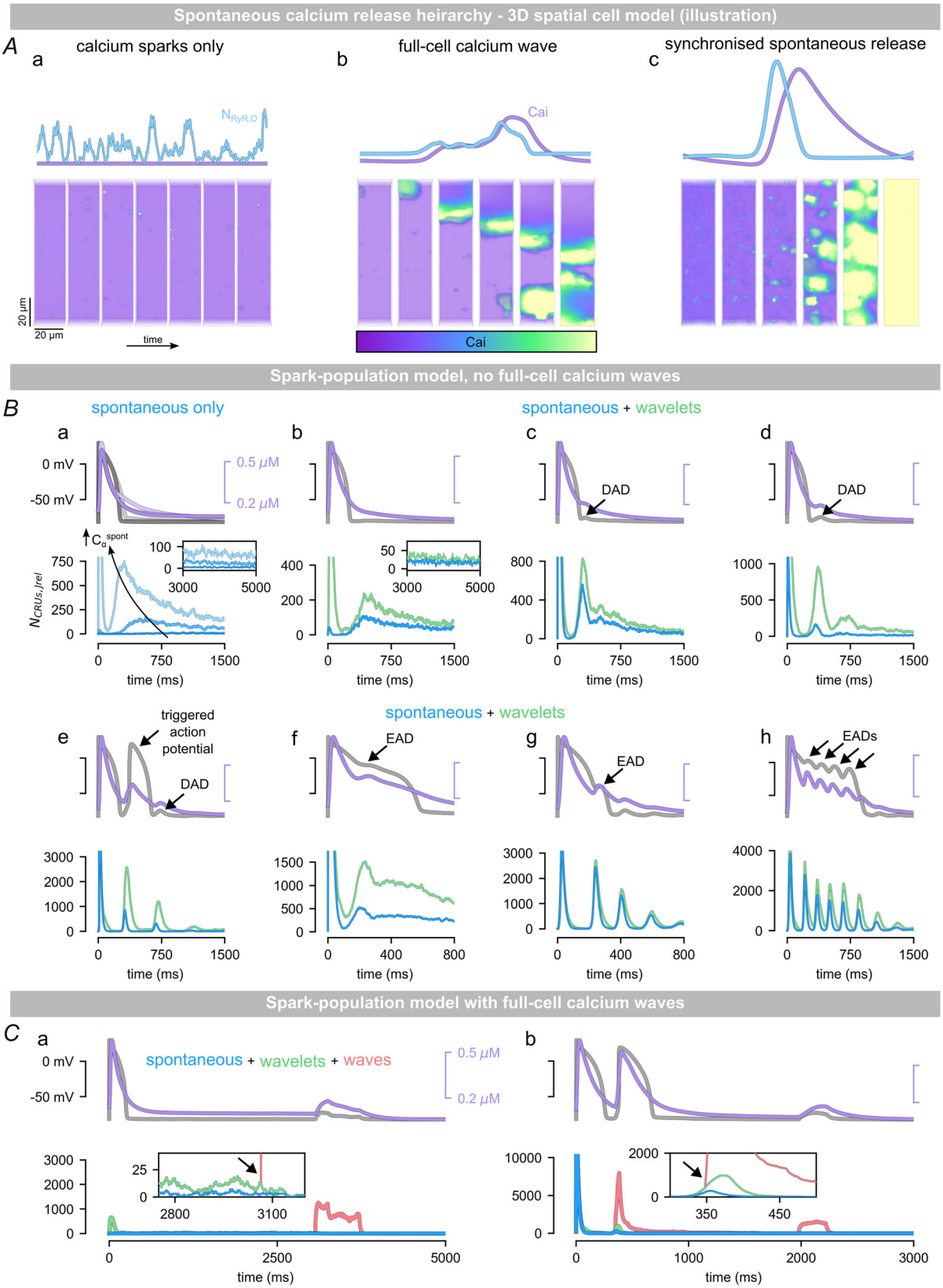

Figure 12. Spontaneous calcium release hierarchy.
A, Illustrative simulations of spontaneous calcium sparks (*a*), waves (*b*) and whole-cell release (*c*) performed in a 3D cell model (Colman, 2019). Top panels show the average intracellular calcium (purple) and open RyR2 wave-

form from the model, whereas the lower panels are temporal snapshots of calcium concentration in the 3D volume. *B*, Dynamics observed in the spark-population model under different spontaneous release parameters, with spontaneous sparks only at differing spark rates (*a*) and with both spontaneous and wavelet sparks (*b*-*h*). EADs, DADs and triggered action potentials are labelled for clarity. *C*, Full-cell spontaneous calcium waves in the spark-population model, emerging from a background of low noise (*a*) and high noise (*b*). Parameters used for each panel are as follows: *Ba*: $C_\alpha^{\text{spont}} \times 1.0$ (dark blue), $\times 100$ (medium shade) and $\times 10000$ (light blue), $C_\alpha^{\text{wavelet-spont}} = 0$ and $k_{\text{CaSR}}^{\text{spont}} = -0.2$. *Bb*: $C_\alpha^{\text{spont}} \times 100$, $C_\alpha^{\text{wavelet-spont}} \times 1.0$ and $k_{\text{CaSR}}^{\text{spont}} = -0.2$. *Bc*: $C_\alpha^{\text{spont}} \times 1000$, $C_\alpha^{\text{wavelet-spont}} \times 5.0$, $C_\alpha^{\text{wavelet-wavelet}} \times 2.0$ and $k_{\text{CaSR}}^{\text{spont}} = -0.2$. *Bd*: $C_\alpha^{\text{spont}} \times 1000$, $C_\alpha^{\text{wavelet-spont}} \times 5.0$, $C_\alpha^{\text{wavelet-wavelet}} \times 2.0$ and $k_{\text{CaSR}}^{\text{spont}} = -0.1$. *Be*: $C_\alpha^{\text{spont}} \times 100$, $C_\alpha^{\text{wavelet-spont}} \times 5.0$, $C_\alpha^{\text{wavelet-wavelet}} \times 2.0$, $k_{\text{CaSR}}^{\text{spont}} = -0.025$ and $Ca_{\text{SR}_{50}}^{\text{spont}}$ shifted by -0.05. *Bf*: $C_\alpha^{\text{spont}} \times 1000$, $C_\alpha^{\text{wavelet-spont}} \times 5.0$, $C_\alpha^{\text{wavelet-wavelet}} \times 2.0$, $k_{\text{CaSR}}^{\text{spont}} = -0.2$ and $Ca_{\text{SR}_{50}}^{\text{spont}}$ shifted by -0.2. *Bg*: $C_\alpha^{\text{spont}} \times 1000$, $C_\alpha^{\text{wavelet-spont}} \times 1.0$, $C_\alpha^{\text{wavelet-wavelet}} \times 1.0$, $k_{\text{CaSR}}^{\text{spont}} = -0.025$ and $Ca_{\text{SR}_{50}}^{\text{spont}}$ shifted by -0.1. *Bh*: $C_\alpha^{\text{spont}} \times 1000$, $C_\alpha^{\text{wavelet-spont}} \times 5.0$, $C_\alpha^{\text{wavelet-wavelet}} \times 2.0$, $k_{\text{CaSR}}^{\text{spont}} = -0.025$ and $Ca_{\text{SR}_{50}}^{\text{spont}}$ shifted by -0.2. *Ca*: $C_\alpha^{\text{spont}} \times 1.0$, $C_\alpha^{\text{spont}} \times 1.0$, $C_\alpha^{\text{wavelet-wavelet}} \times 1.0$, $C_\alpha^{\text{wave}} \times 1.0$, $k_{\text{CaSR}}^{\text{spont}} = -0.2$ and $Ca_{\text{SR}_{50}}^{\text{wave}}$ shifted by -0.05. *Cb*: $C_\alpha^{\text{spont}} \times 1000$, $C_\alpha^{\text{wavelet-spont}} \times 5.0$, $C_\alpha^{\text{wavelet-wavelet}} \times 2.0$, $C_\alpha^{\text{wave}} \times 100$, $k_{\text{CaSR}}^{\text{spont}} = -0.1$ and $Ca_{\text{SR}_{50}}^{\text{wave}}$ shifted by -0.1.

experimental studies (Fowler et al., 2025). With the model of spontaneous activity substantially increased (C_α^{spont} and $C_\alpha^{\text{wave}} \times 100$, $k_{\text{CaSR}}^{\text{spont}} \times 0.5$, and $Ca_{\text{SR}_{50}}^{\text{spont}}$ and $Ca_{\text{SR}_{50}}^{\text{wave}}$ shifted by -0.05) DADs and spontaneous APs frequently occurred between stimulated excitations (Fig. 13*Gb*).

Finally the effect of t-system density on spontaneous release was assessed. In the Grandi atrial model few spontaneous events occurred at full t-system density (Fig. 13*Ha–b*), whereas reduced density produced calcium oscillations primarily originating from the non-t-system region (Fig. 13*Hc–d*) consistent with recent 3D cell modelling studies (Zhang et al., 2023). Under enhanced spontaneous-release conditions multiple spontaneous APs arose, often exhibiting prolongation or EADs (Fig. 13*I*).

Effect of cell size and structure

Although the model is non-spatial, cell size and shape, defined by the number of CRUs in the X, Y and Z directions, affect its dynamics in three ways. First, the total CRU population influences the level of stochastic noise: beat-to-beat variability is greater in smaller cells and reduced in larger ones (Fig. 14*A*). Second, cell dimensions determine the ratio of surface to interior CRUs, and thus the ratio of t-system to non-t-system CRUs in detubulated cells. In thin cells the number of interior CRUs is comparable to surface CRUs, allowing robust and rapid propagation into the non-t-system region even at low t-system density (Fig. 14*B*). Conversely in wide cells, interior CRUs vastly outnumber surface CRUs, leading to slower activation of interior non-t-system CRUs and an abbreviated whole-cell calcium transient (Fig. 14*B*). Finally, the cell's cross-sectional area (defined by $N_x \times N_y$) determines the size of a full-cell wavefront, while cell length is inversely correlated with the likelihood of wavefront termination. Consequently full-cell calcium waves exhibit distinct dynamics in long and thin versus short and wide cells: the former favour low-amplitude, long-duration waves, whereas the latter promote high-amplitude, short-duration waves (Fig. 14*C*).

Translation into tissue models

The model was next applied in tissue simulations. As an illustrative example, a random t-system density was assigned across a 2D sheet of tissue comprising 50×50, 200×200 or 300×300 nodes. The smaller sheet was used primarily for visualisation, ensuring that intercellular variability was not obscured by image resolution. During normal pacing in the CRN atrial model, variations in t-system density clearly influenced both the peak calcium concentration and the rise time of the calcium transient (Fig. 15*A*). Increasing the steepness of the dependence of triggered sparks on I_{CaL} produced calcium-transient alternans, which in turn gave rise to alternans of the AP duration (Fig. 15*B*).

Discussion

In this study we present a mechanistically focused phenomenological model of cardiac calcium spark dynamics that captures a wide range of spatially dependent behaviours and enables the simulation of variable cellular structures. The model was shown to be highly portable, readily integrated into calcium-handling formulations with distinct architectures and capable of reproducing both normal and rate-dependent pacing dynamics (Fig. 4). It also reproduced key experimental observations, including centripetal calcium-wave propagation in detubulated cells (Figs. 6 and 7), delayed calcium sparks arising from loss of upstroke synchrony (Fig. 11), multiple mechanisms underlying calcium-transient alternans (Figs. 8–10) and spontaneous calcium release hierarchy (Figs. 12 and 13).

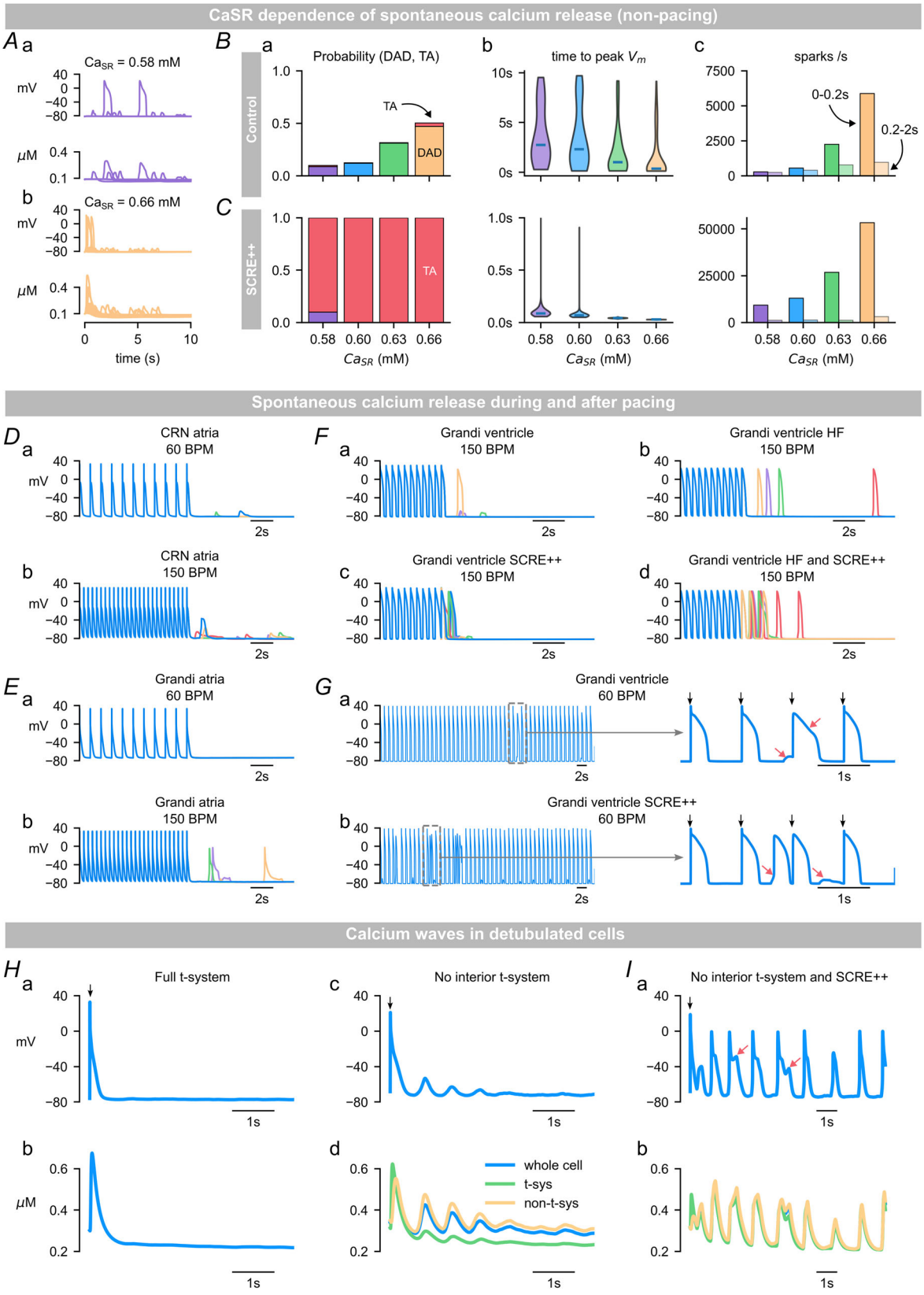

Figure 13. Spontaneous activity during pacing.
A, 100 simulation overlays of voltage and calcium at low (*a*) and high (*b*) Ca_{SR} (corresponding to 60 and 150 BPM, respectively). *Ba,Ca*, The probability of DADs or triggered action potentials (TA); *b*, latency time to the voltage

peak for conditions that did observe a DAD or TA and; *c*, spontaneous spark rates at the different Ca_{SR} for the first 0.2 and next 1.8 s in control (*B*) and a spontaneous calcium release prone model (SCRE++; *C*). *D–F*, Examples of the final few stimulated excitations and the quiescent period under different conditions; five simulations overlaid for each panel. *G*, Example of where spontaneous calcium release can interrupt normal pacing. *H*, spontaneous activity under normal conditions in a cell without a t-system compared to one with full t-system, showing the whole-cell average (blue) and t-system and non-t-system concentrations (green and orange, respectively). Vertical downward arrows indicate applied stimuli.

Portability and controllability

The model structure and primary control parameters were designed so that each parameter represents a physiologically meaningful process, making the model intuitive to tune. These processes are as follows: (1) response to LTCC trigger, with parameters controlling the coupling strength and functional dependence on I_{CaL} and Ca_{SR}; (2) spontaneous spark basal rate and the steepness of its dependence on Ca_{SR}; (3) the rate of spatial CRU recruitment, and full-cell wave creation with controllable Ca_{SR} dependent steepness. Parameters can also be varied independently for the t-system and non-t-system populations, enabling reproduction of observed behaviours beyond the scope explored in this study.

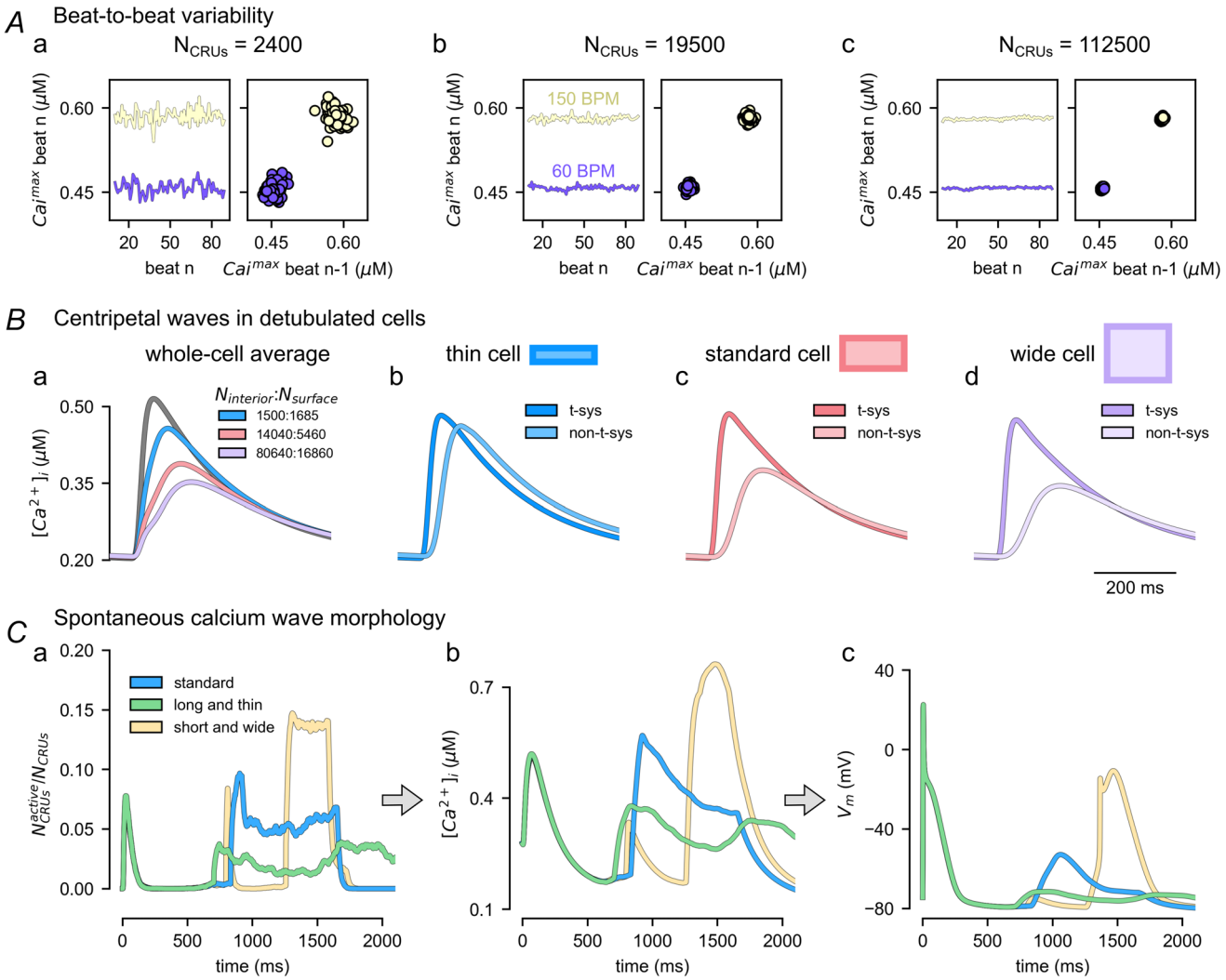

Figure 14. Impact of cell size.
A, Beat-to-beat variability in models with different total CRU populations (*a–c*). *B*, Whole cell (*a*) and compartmental (*b-d*) calcium concentrations in different sized cells with a t-system density of zero. *C*, Examples of full-cell calcium waves in cells of different sizes, showing the number of active CRUs (*a*), the resulting spontaneous calcium transient (*b*) and the voltage deflection (*c*).

Whereas the model cannot be implemented in every contemporary cell model (some features of calcium handling are required, such as well-behaved Ca_{SR} ranges), it is readily portable to many models. Furthermore its direct tracking of discrete active CRUs makes it well suited for non-spatial adaptations of 3D cell models, allowing the replacement of the RyR2 formulation with minimal modification. This enables detailed spatial-scale investigations to inform parameters of reduced cell models, which can then be translated into tissue-scale simulations.

Capturing spatially dependent calcium handling phenomena

Variable t-system density. A primary motivation for developing this model was to capture calcium handling in myocytes with variable t-system density, ranging from fully robust networks (100% t-system density) to cells with few or no tubules (0% t-system density). This is particularly relevant for atrial myocytes, which typically have lower t-system density than ventricular cells in healthy conditions, as well as for disease-associated

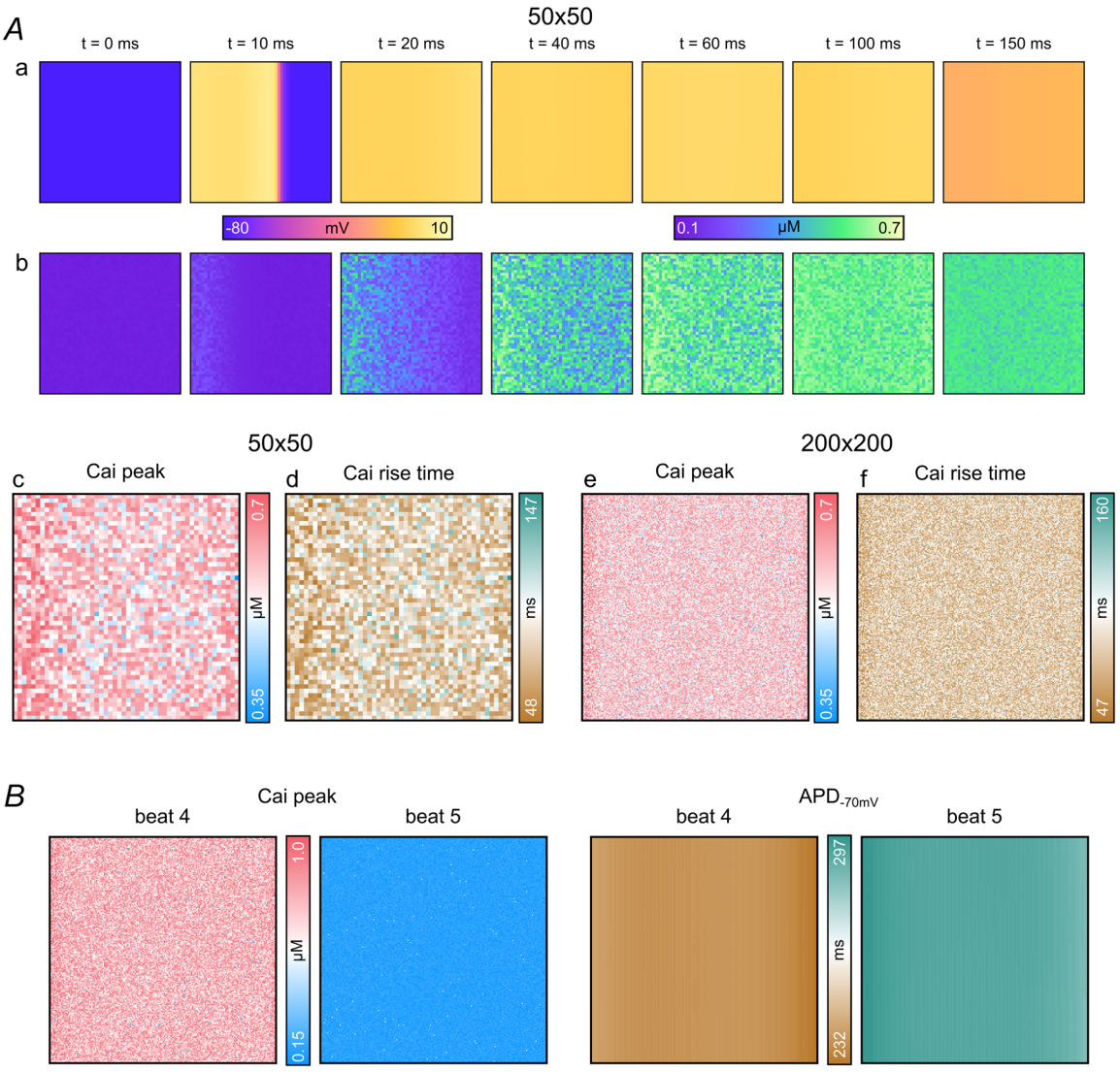

Figure 15. Example tissue simulations.
A, normal pacing with variable t-system density, illustrating temporal snapshots of voltage (*a*) and calcium (*b*) as well as the calcium peak (*c,e*) and rise times (*d,f*) in the 50×50 and 200×200 tissue models. *B*, example of calcium transient alternans underlying AP duration alternans, illustrating the peak calcium and the duration on two successive beats.

detubulation observed in heart failure and atrial fibrillation. Lower t-system density reduces synchrony of the calcium transient, as spatial CRU recruitment contributes substantially to the whole-cell average transient, resulting in centripetal 'U' or 'V' waves observed in linescan imaging of detubulated cells (Brette et al., 2004; Dibb et al., 2022; Greiser et al., 2014; Greiser, 2017). Reproducing this behaviour is challenging in non-spatial models, but is captured by the presented spark-population model.

The importance of reproducing calcium wave propagation and its failure is highlighted by the case of rapid atrial pacing or atrial fibrillation. Both conditions are associated with reduced LTCC function and a consequent decrease in whole-cell calcium transient amplitude. Imaging studies, however, show that surface calcium transients, where RyR2 clusters are coupled to LTCCs, remain largely unchanged, indicating that 'calcium silencing,' that is, failed centripetal wave propagation, is the primary mechanism underlying the reduced whole-cell amplitude (Greiser et al., 2014). This surface-internal disparity may reflect compensatory remodelling of dyadic structure–function relationships at the surface membrane, enhancing triggered calcium release locally (Bers, 2006; Greiser et al., 2014; Smith et al., 2022). Traditional cell models cannot capture this mechanism, instead reproducing the effect of atrial fibrillation through a uniform loss of LTCC-triggered calcium release. In contrast, the spark-population model can reproduce failed centripetal propagation while allowing local upregulation of calcium release at surface sites independently of the interior. This framework enables more accurate modelling of calcium handling dysfunction in atrial fibrillation and its translation to tissue-scale simulations, with similar applicability to heart failure and other conditions.

More generally the model also enables more meaningful investigation into the effect of cell size and structure on tissue dynamics. Traditional cell models are typically expressed with all currents normalised to the cell capacitance and therefore changes to the cell capacitance (and the accompanying change to cellular volume) have only limited impact on whole-cell dynamics. The spark-population model explicitly represents N discrete CRUs, and the stochastic activation and spatial propagation of calcium waves allow the effects of cell size and geometry to be meaningfully incorporated. This enables more detailed predictions of the influence of cell structure on function and provides a framework for translating these effects to tissue-scale simulations.

Beat-to-beat variability, alternans, disorder and spontaneous activity. The model reproduces multiple mechanisms underlying calcium transient alternans, including modulation by spatial coupling. Its stochastic formulation allows complex and disordered patterns to emerge, including higher-order alternans (e.g. 4- and 7-cycle) and highly irregular beat-to-beat variability. Alternans occurred across all t-system densities, with lower densities promoting greater disorder and the emergence of alternans at slower pacing rates. These heterogeneous patterns were also observed in illustrative tissue-scale simulations.

The model was also capable of reproducing Ca_{SR}-dependent spontaneous calcium release hierarchy leading to a range of presentations of EADs, DADs and triggered APs, both with and without full-cell calcium waves. The explicit separation of wavelet and wave states enables controlled initiation of full-cell waves and is essential for generating significant spontaneous activity at large latency times (i.e. during equilibrium quiescent Ca_{SR}). This framework therefore allows mechanistic investigation of arrhythmia triggers and substrate at both the cellular and tissue scales.

Value of the model

The presented model provides a powerful and convenient framework for mechanistic inquest into spatial calcium handling dynamics. Its controllability and transparency enable straightforward experimental design and interpretation, particularly compared to wet-lab experiments. Even relative to 3D spatial cell models, the spark-population model offers additional control and analytic accessibility: the populations of triggered, spontaneous and recruited CRUs are readily accessible, and their dynamics can be independently controlled, with the ability to directly incorporate experimental measures such as spark rate, propagation probability and whole-cell wave probability.

A primary motivation for the model is its ability to translate spatial calcium handling features to the whole-organ, the scale where cardiac function and dysfunction ultimately reside. By providing a framework that integrates easily into a variety of contemporary computational cell models, it offers a tool for ongoing and future studies of cellular electrophysiology and calcium handling across species and cell types. It is readily implementable in large-scale tissue models to dissect multiscale mechanisms of EC coupling and arrhythmia and offers advantages over previous approaches attempting to bridge spatial scales.

The presented model represents the most generalised and mechanistically focused approach for integration of spatial calcium handling into non-spatial cell models. The spontaneous release function approach (Colman, 2019), for example, is limited to only modelling whole-cell spontaneous calcium release events, and was not a model

of stochastic CICR, transverse calcium wave propagation during pacing or calcium transient alternans. Previous models that used a population dynamics approach presented a more general model than the spontaneous release function approach, but were less detailed and limited in scope compared to the present model. This new model offers major advantages, including explicit t-system/non-t-system coupling, representation of different cell sizes and structures, modelling of whole-cell calcium wavefront size and the ability to reproduce features of spontaneous calcium release hierarchy.

Other previous alternatives include the Koivumäki et al. (2011) model, which used a four-compartment calcium handling system to simulate centripetal calcium waves in atrial cells lacking a t-system. While it successfully reproduced the delayed calcium transient peak relative to full t-system models, it was limited to four diffusive compartments, could not model variable t-system density and lacked the stochastic dynamics captured in the present model.

The present mechanistic model is closer to being biophysically detailed than it is to a pure phenomenological model, although it is important to clarify that it is not biophysically detailed: despite controlling J_{rel} through modelling open RyR2 dynamics, there is no RyR2 gating model contained within; indeed the purpose was to separate different phenomena that result from RyR2 gating and inter-CRU coupling. Therefore the model cannot directly predict the impact of a modulation to RyR2 gating on cellular function. Rather, these must be reproduced in the functional dependence and transition rates of the mechanistic model. Nevertheless it is constructed based on the biophysical details of the mechanisms of calcium spark activation, recruitment and lifetime, and there are clear correlations between the parameters of the model and those of biophysically detailed models and physiological measures.

Modelling regulation of calcium handling

For any condition that does not have a direct impact on RyR2 kinetics or relevant calcium handling sub-cellular structure, this framework naturally incorporates any secondary impact on calcium handling function through the dependence on I_{CaL} and Ca_{SR}. For example a condition that reduces LTCC activity will naturally lead to a smaller response of the triggered calcium sparks as well as potential SR unloading, further reducing the triggered response. However conditions that directly affect RyR kinetics or inter-cluster coupling (e.g. structural remodelling) need to be explicitly encoded into the spark-population model through modification of the appropriate parameters. For example a general increase in RyR sensitivity can be implemented by increasing all activation transition rate constants; changes to the propagation threshold for waves can be directly included through the threshold parameters; steeper Ca_{SR} dependence of triggered or spontaneous sparks can be captured through directly modifying the relevant gradient parameters; reduced RyR opening time would correspond to a shorter J_{rel} time course and total recruiter time.

An advantage of this set-up is indeed this ability to control these independently. For example, the spontaneous spark rate could be increased without affecting the triggered spark rate, representing increased leakiness but not overall sensitivity of RyR2s to LTCCs; conversely, the coupling strength to the LTCCs could be adjusted independently of the RyR sensitivity, capturing structural remodelling of the dyad that alters the co-localisation distances of LTCCs and RyR2s; furthermore, the wave rate could be increased/decreased without affecting the spontaneous spark rate, capturing an easier/inhibited propagation of sparks into waves that may emerge due to increased/decreased inter-cluster coupling. Hence, experimental data can be directly included without requiring a detailed model that fully captures the underlying mechanisms, and detailed analysis of 3D cell models can be similarly translated through these parameters. Application of this model to these disease conditions therefore requires sufficient data or theoretical basis to modify the appropriate parameters; indeed the model can be directly used to test the viability of proposed theories.

In general, a framework wherein detailed simulations are performed using a spatial cell model to inform the parameters of the spark-population model is recommended for more complicated regulation. For example, SERCA can have contradictory implications for calcium cycling: larger SERCA expression can help to maintain or overload the SR, promoting spontaneous release, but it may also lower local cytosolic concentration near and in the dyad, which would inhibit spontaneous release; the efflux can also inhibit the propagation of calcium waves while the higher load could maintain them. Indeed, we recently revealed some of the complex non-linear impacts of heterogeneity in the sub-cellular expression of SERCA on calcium cycling including alternans and SCRE (Holmes et al., 2022). Other structural features, such as inter-tubule spacing, RyR arrangement, NCX heterogeneity and mitochondrial distribution, would also be most suitable to first explore their impact at the cellular scale, before parameterising the present model to provide the tissue-level and translational benefits.

Limitations

A primary limitation of the model is that spark transition rates depend only on Ca_{SR} and I_{CaL}, and not directly

on intracellular calcium concentration. This choice was made to minimise the number of parameters while still capturing the key spatially dependent phenomena relevant for EC-coupling and arrhythmia mechanisms. Local calcium dependence is implicitly encoded within the activation transition rates, but there may be conditions of elevated intracellular calcium where the model is limited. In principle, calcium-dependent terms could be added to any state transition function to incorporate direct intracellular calcium regulation.

T-system variability described a fully random t-system distribution, without implementation of potential clustering or patches of t-system regions. However, it would be possible to introduce an additional factor controlling the distribution of neighbours to accommodate t-system patchiness. It was also the only feature that was considered to be spatially variable in the model. This was motivated by its importance in fundamental calcium handling regulation. However it is also the simplest system to reproduce in such a model because, at the CRU scale, it is essentially binary: each CRU either does or does not contain a sarcolemmal or t-system membrane component. This feature was critical in enabling the construction of this model, as it allowed splitting the total CRU population into the two populations of t-system and non-t-system; it is not clear if continuous spatial heterogeneities, such as RyR2 cluster size and local LTCC, SERCA and NCX expression, could be directly incorporated into this framework. These could be incorporated 'brute-force' by deriving parameter sets from experiments or 3D models, but a more robust integration would be beneficial.

Separation into the two populations of t-system and non-t-system also omits any differences in the dynamics of surface sarcolemma CRUs and interior t-system CRUs. Evidence suggests that RyR2-LTCC coupling differs between these regions, influencing calcium dynamics. Introducing a third CRU population for surface LTCC-coupled CRUs would allow separate behaviour, although the approach to neighbour coupling between these three populations would need to be carefully considered.

The model does not account for variability in the proportion of open RyR2s within a single CRU. In reality SR calcium load or RyR2 sensitisation can modulate the amplitude of individual sparks. It is non-trivial to implement a dynamically variable peak proportion of open RyR2s per CRU as the variables that would control this, I_{CaL} and Ca_{SR}, vary dynamically during J_{rel}, which does not easily align with the distinct state occupancy of the model. However, a distinct magnitude of calcium spark could be set for the different populations if required (e.g. a triggered spark could be larger than a spontaneous spark). Moreover both excited and recruiter states contribute equally to J_{rel}. A more physiological approach could weigh the excited state more heavily in J_{rel}.

Membrane capacitance was also non-trivial to consider in the context of variable t-system density. This is because the ratio of interior to surface CRUs does not align with the ratio of the capacitance of the surface sarcolemma to the interior t-system. That is, the per CRU capacitance is not equal between these two regions. This presents some complex considerations that must be accounted for if the total membrane capacitance (per CRU capacitance multiplied by number of CRUs) is required, including as with coupling to non-myocytes such as fibroblasts or macrophages.

Conclusions

We have presented a conceptually simple phenomenological model that captures multiple mechanisms of calcium spark initiation and spatial recruitment in cardiac myocytes. This approach integrates spatially dependent calcium handling phenomena into conventional non-spatial models of cellular electrophysiology and calcium dynamics. The model provides a powerful framework for mechanistic analysis of calcium handling, enabling the translation of sub-micron scale dynamics to the whole organ and supporting detailed multiscale investigations into arrhythmia mechanisms and EC-coupling dysregulation. More broadly the framework offers a flexible foundation for developing a generalised description of calcium handling, adaptable across species and regional myocyte subtypes, while maintaining computational efficiency.

Appendix A: Model description

A.1. State transition rates

The transition rates that describe the CRU-state cycle (Figs. 1 and 2) take the following form:

$$\alpha_{\text{trig}} = C_{\alpha}^{\text{trig}} f_1(I_{\text{CaL}}, Ca_{\text{SR}}) \tag{A.1}$$

$$\alpha_{\text{spont}} = C_{\alpha}^{\text{spont}} f_2(Ca_{\text{SR}}) \tag{A.2}$$

$$\begin{bmatrix} \alpha_{\text{wavelet}-\text{trig}} \\ \alpha_{\text{wavelet-spont}} \\ \alpha_{\text{wavelet-wavelet}} \end{bmatrix} = \begin{bmatrix} C_{\alpha}^{\text{wavelet-trig}} \\ C_{\alpha}^{\text{wavelet-spont}} \\ C_{\alpha}^{\text{wavelet-wavelet}} \end{bmatrix} f_3(Ca_{\text{SR}}) \tag{A.3}$$

$$\alpha_{\text{wave-wavelet}} = C_{\alpha}^{\text{wave}} f_4(Ca_{\text{SR}}) \tag{A.4}$$

$$P(\text{wave} - \text{wave}) = f_5(Ca_{\text{SR}}) \tag{A.5}$$

$$\beta = \frac{\ln(2)}{0.5 \cdot t_{\text{wavedelay}}} \tag{A.6}$$

$$\gamma = \frac{\ln(2)}{0.5 \cdot \left(t_{J_{\text{rel}}} - t_{\text{wavedelay}}\right)} \tag{A.7}$$

$$\delta = \frac{\ln(2)}{0.5 \cdot \left(t_{\text{recruit}} - t_{\text{J}_{\text{rel}}}\right)} \tag{A.8}$$

$$\epsilon = r_{\text{recov}} \tag{A.9}$$

The forms of the functions f_{1-5} will be discussed later in the subsection A.6. The next subsection will describe the algorithm to implement the model.

A.2. Implementation of the spark-population model

The model calculates the occupancy of the various states in a discrete system of size N_{T}. The model is solved using a succession of random binomial samples to determine the number of CRUs that transition from one state to the next, governed by the transition rates. In general the number created at a given timestep is described by the probability, p, and the currently available population for the given state transition:

$$\Delta^{+}N_x = \text{B}\left(\text{p, population}\right) \tag{A.10}$$

We describe in full the algorithm used to implement this approach for the multiple populations. We will first describe the model in the case of uniform t-system density (only a single total population) before discussing how two coupled populations were implemented. Because the model counts the number of CRUs that transition between states, the following description is identical to the algorithm for computational implementation of the model and is presented in the same sequence as the accompanying C++ code.

Triggered CRUs. The total population for the activation of triggered CRUs is the total available population, whereas the populations available for the transitions through the state cycle are given by the current occupancy of the state from which the transition occurs:

$$\Delta^{+}N^{\text{trig}}_{\text{excited}} = \text{B}\left(\Delta t\alpha_{\text{trig}}, N_{\text{available}}\right) \tag{A.11}$$

$$\Delta^{+}N^{\text{trig}}_{\text{recruiter-Jrel}} = \text{B}\left(\Delta t\beta, N^{\text{trig}}_{\text{excited}}\right) \tag{A.12}$$

$$\Delta^{+}N^{\text{trig}}_{\text{recruiter-nonJrel}} = \text{B}\left(\Delta t\gamma, N^{\text{trig}}_{\text{recruiter-Jrel}}\right) \tag{A.13}$$

$$\Delta^{+}N^{\text{trig}}_{\text{refractory}} = \text{B}\left(\Delta t\delta, N^{\text{trig}}_{\text{recruiter-nonJrel}}\right) \tag{A.14}$$

$$N_{\text{available}} = N_{\text{available}} - \Delta^{+}N^{\text{trig}}_{\text{excited}} \tag{A.15}$$

where the update of the number of available CRUs is to ensure that activated CRUs cannot be activated by other mechanisms (i.e. avoid double counting of available CRUs). Note that this does allow failed trials to be activated by other mechanisms, which reflects the independence of the activation mechanisms.

Spontaneous CRUs. The spontaneous CRU populations have exactly the same implementation as the triggered CRUs:

$$\Delta^{+}N^{\text{spont}}_{\text{excited}} = \text{B}\left(\Delta t\alpha_{\text{spont}}, N_{\text{available}}\right) \tag{A.16}$$

$$\Delta^{+}N^{\text{spont}}_{\text{recruiter-Jrel}} = \text{B}\left(\Delta t\beta, N^{\text{spont}}_{\text{excited}}\right) \tag{A.17}$$

$$\Delta^{+}N^{\text{spont}}_{\text{recruiter-nonJrel}} = \text{B}\left(\Delta t\gamma, N^{\text{spont}}_{\text{recruiter-Jrel}}\right) \tag{A.18}$$

$$\Delta^{+}N^{\text{spont}}_{\text{refractory}} = \text{B}\left(\Delta t\delta, N^{\text{spont}}_{\text{recruiter-nonJrel}}\right) \tag{A.19}$$

$$N_{\text{available}} = N_{\text{available}} - \Delta^{+}N^{\text{spont}}_{\text{excited}} \tag{A.20}$$

Wavelet CRUs. Wavelet CRUs may be activated by three populations – the current occupancy of the recruiter states for triggered, spontaneous and wavelet CRUs. The minimum of the recruiter state occupancy multiplied by the number of neighbours each active CRU has access to and the total available state occupancy is taken to ensure that the number of available CRUs ultimately limits the number that can be activated through spatial propagation.

$$P_{\text{recruiter}} = \min \left(nei^{\text{trig}}\left(N^{\text{trig}}_{\text{recruiter-Jrel}} + N^{\text{trig}}_{\text{recruiter-nonJrel}}\right), N_{\text{available}}\right) \tag{A.21}$$

$$\Delta^{+}N^{\text{wavelet-trig}}_{\text{excited}} = \text{B}\left(\Delta t\alpha_{\text{wavelet-trig}}, P_{\text{recruiter}}\right) \tag{A.22}$$

$$N_{\text{available}} = N_{\text{available}} - \Delta^{+}N^{\text{wavelet-trig}}_{\text{excited}} \tag{A.23}$$

$$P_{\text{recruiter}} = \min \left(nei^{\text{spont}}\left(N^{\text{spont}}_{\text{recruiter-Jrel}} + N^{\text{spont}}_{\text{recruiter-nonJrel}}\right), N_{\text{available}}\right) \tag{A.24}$$

$$\Delta^{+}N^{\text{wavelet-spont}}_{\text{excited}} = \text{B}\left(\Delta t\alpha_{\text{wavelet-spont}}, P_{\text{recruiter}}\right) \tag{A.25}$$

$$N_{\text{available}} = N_{\text{available}} - \Delta^{+}N^{\text{wavelet-spont}}_{\text{excited}} \tag{A.26}$$

$$P_{\text{recruiter}} = \min \left(nei^{\text{wavelet}}\left(N^{\text{wavelet}}_{\text{recruiter-Jrel}} + N^{\text{wavelet}}_{\text{recruiter-nonJrel}}\right), N_{\text{available}}\right) \tag{A.27}$$

$$\Delta^{+}N^{\text{wavelet-wavelet}}_{\text{excited}} = \text{B}\left(\Delta t\alpha_{\text{wavelet-wavelet}}, P_{\text{recruiter}}\right) \tag{A.28}$$

$$N_{\text{available}} = N_{\text{available}} - \Delta^{+}N^{\text{wavelet-wavelet}}_{\text{excited}} \tag{A.29}$$

$$\Delta^{+}N^{\text{wavelet}}_{\text{excited}} = \Delta^{+}N^{\text{wavelet-trig}}_{\text{excited}} + \Delta^{+}N^{\text{wavelet-spont}}_{\text{excited}} + \Delta^{+}N^{\text{wavelet-wavelet}}_{\text{excited}} \tag{A.30}$$

$$\Delta^{+}N^{\text{wavelet}}_{\text{recruiter-Jrel}} = \text{B}\left(\Delta t\beta, N^{\text{wavelet}}_{\text{excited}}\right) \tag{A.31}$$

$$\Delta^{+}N^{\text{wavelet}}_{\text{recruiter-nonJrel}} = \text{B}\left(\Delta t\gamma, N^{\text{wavelet}}_{\text{recruiter-Jrel}}\right) \tag{A.32}$$

$$\Delta^{+}N^{\text{wavelet}}_{\text{refractory}} = \text{B}\left(\Delta t\delta, N^{\text{wavelet}}_{\text{recruiter-nonJrel}}\right) \tag{A.33}$$

Full-cell wave CRUs. Wave CRUs are dependent only on the populations of wavelet CRUs (for wavefront activation) and wave CRUs (for wavefront propagation):

$$\Delta^{+}N^{\text{wave-wavelet}}_{\text{excited}} = 0.7N_xN_y\,\text{B}\left(\Delta t\alpha_{\text{wave-wavelet}}, N^{\text{wavelet}}_{\text{recruiter-Jrel}} + N^{\text{wavelet}}_{\text{recruiter-nonJrel}}\right) \quad \text{(A.34)}$$

$$\Delta^{+}N^{\text{wave-wavelet}}_{\text{excited}} = \min\left(\Delta^{+}N^{\text{wave-wavelet}}_{\text{excited}}, N_{\text{available}}\right) \quad \text{(A.35)}$$

$$N_{\text{available}} = N_{\text{available}} - \Delta^{+}N^{\text{wave-wavelet}}_{\text{excited}} \quad \text{(A.36)}$$

$$P_{\text{recruiter}} = \min\left(2\Delta^{+}N^{\text{wave}}_{\text{recruiter}}, N_{\text{available}}\right) \quad \text{(A.37)}$$

$$\Delta^{+}N^{\text{wave-wave}}_{\text{excited}} = \text{B}\left(P(wave-wave), P_{\text{recruiter}}\right) \quad \text{(A.38)}$$

$$N_{\text{available}} = N_{\text{available}} - \Delta^{+}N^{\text{wave-wave}}_{\text{excited}} \quad \text{(A.39)}$$

$$\Delta^{+}N^{\text{wave}}_{\text{recruiter-Jrel}} = \text{B}\left(\Delta t\beta, N^{\text{wave}}_{\text{excited}}\right) \quad \text{(A.40)}$$

$$\Delta^{+}N^{\text{wave}}_{\text{recruiter-nonJrel}} = \text{B}\left(\Delta t\gamma, N^{\text{wave}}_{\text{recruiter-Jrel}}\right) \quad \text{(A.41)}$$

$$\Delta^{+}N^{\text{wave}}_{\text{refractory}} = \text{B}\left(\Delta t\delta, N^{\text{wave}}_{\text{recruiter-nonJrel}}\right) \quad \text{(A.42)}$$

Refractory to available. The number of created available CRUs depends only on the recruiter population:

$$\Delta^{+}N_{\text{available}} = \text{B}\left(\Delta t\epsilon, N_{\text{recruiter}}\right) \quad \text{(A.43)}$$

Update states. The state occupancies are then updated by simply summing and subtracting the number created in each state:

$$N_x = N_x + \Delta N_x \quad \text{(A.44)}$$

$$\Delta N_{\text{available}} = \Delta^{+}N_{\text{available}} - \Delta^{+}N^{\text{trig}}_{\text{excited}} - \Delta^{+}N^{\text{spont}}_{\text{excited}} - \Delta^{+}N^{\text{wave}}_{\text{excited}} - \Delta^{+}N^{\text{wavelet}}_{\text{excited}} \quad \text{(A.45)}$$

$$\Delta N^{\text{trig}}_{\text{excited}} = \Delta^{+}N^{\text{trig}}_{\text{excited}} - \Delta^{+}N^{\text{trig}}_{\text{recruiter-Jrel}} \quad \text{(A.46)}$$

$$\Delta N^{\text{spont}}_{\text{excited}} = \Delta^{+}N^{\text{spont}}_{\text{excited}} - \Delta^{+}N^{\text{spont}}_{\text{recruiter-Jrel}} \quad \text{(A.47)}$$

$$\Delta N^{\text{wavelet}}_{\text{excited}} = \Delta^{+}N^{\text{wavelet}}_{\text{excited}} - \Delta^{+}N^{\text{wavelet}}_{\text{recruiter-Jrel}} \quad \text{(A.48)}$$

$$\Delta N^{\text{wave}}_{\text{excited}} = \Delta^{+}N^{\text{wave}}_{\text{excited}} - \Delta^{+}N^{\text{wave}}_{\text{recruiter-Jrel}} \quad \text{(A.49)}$$

$$\Delta N^{\text{trig}}_{\text{recruiter-Jrel}} = \Delta^{+}N^{\text{trig}}_{\text{recruiter-Jrel}} - \Delta^{+}N^{\text{trig}}_{\text{recruiter-nonJrel}} \quad \text{(A.50)}$$

$$\Delta N^{\text{spont}}_{\text{recruiter-Jrel}} = \Delta^{+}N^{\text{spont}}_{\text{recruiter-Jrel}} - \Delta^{+}N^{\text{spont}}_{\text{recruiter-nonJrel}} \quad \text{(A.51)}$$

$$\Delta N^{\text{wavelet}}_{\text{recruiter-Jrel}} = \Delta^{+}N^{\text{wavelet}}_{\text{recruiter-Jrel}} - \Delta^{+}N^{\text{wavelet}}_{\text{recruiter-nonJrel}} \quad \text{(A.52)}$$

$$\Delta N^{\text{wave}}_{\text{recruiter-Jrel}} = \Delta^{+}N^{\text{wave}}_{\text{recruiter-Jrel}} - \Delta^{+}N^{\text{wave}}_{\text{recruiter-nonJrel}} \quad \text{(A.53)}$$

$$\Delta N^{\text{trig}}_{\text{recruiter-nonJrel}} = \Delta^{+}N^{\text{trig}}_{\text{recruiter-nonJrel}} - \Delta^{+}N^{\text{trig}}_{\text{refractory}} \quad \text{(A.54)}$$

$$\Delta N^{\text{spont}}_{\text{recruiter-nonJrel}} = \Delta^{+}N^{\text{spont}}_{\text{recruiter-nonJrel}} - \Delta^{+}N^{\text{spont}}_{\text{refractory}} \quad \text{(A.55)}$$

$$\Delta N^{\text{wavelet}}_{\text{recruiter-nonJrel}} = \Delta^{+}N^{\text{wavelet}}_{\text{recruiter-nonJrel}} - \Delta^{+}N^{\text{wavelet}}_{\text{refractory}} \quad \text{(A.56)}$$

$$\Delta N^{\text{wave}}_{\text{recruiter-nonJrel}} = \Delta^{+}N^{\text{wave}}_{\text{recruiter-nonJrel}} - \Delta^{+}N^{\text{wave}}_{\text{refractory}} \quad \text{(A.57)}$$

$$\Delta N_{\text{refractory}} = -\Delta^{+}N_{\text{available}} + \Delta^{+}N^{\text{trig}}_{\text{refractory}} + \Delta^{+}N^{\text{spont}}_{\text{refractory}} + \Delta^{+}N^{\text{wavelet}}_{\text{refractory}} + \Delta^{+}N^{\text{wave}}_{\text{refractory}} \quad \text{(A.58)}$$

Note that the subtractions in eqn A.44 have already been performed during the implementation of the algorithm at each step and are not repeated again during the update portion of the code; they are included here for completeness.

A.3. Implementation within cell models

The spark-population model takes in the I_{CaL} and Ca_{SR} variables from the cell model and returns the number of CRUs that contribute to intracellular calcium release:

$$N_{\text{Jrel}} = \sum_{x}\left(N^{x}_{\text{excited}} + N^{x}_{\text{recruiter-Jrel}}\right) \quad \text{(A.59)}$$

$$N_{\text{RyR}} = N_{\text{Jrel}}/N_{\text{T}} \quad \text{(A.60)}$$

where x = triggered, spontaneous, wavelet and wave. The model that describes RyR gating in the original cell model is replaced by this output, scaling from NRyR from the spark-population model to the number of open RyRs in the model's state variable:

$$N_{\text{RyR,O}} = N^{\text{model-rescale}}_{\text{RyR}}N_{\text{RyR}} \quad \text{(A.61)}$$

To account for the difference in local Ca_{SR} load and the global average during calcium release, an effective Ca_{SR} state variable was introduced:

$$\frac{d\left(Ca^{\text{eff}}_{\text{SR}}\right)}{dt} = \frac{Ca_{jSR} - Ca^{\text{eff}}_{\text{SR}}}{\tau_{Ca^{\text{eff}}_{\text{SR}}}} \quad \text{(A.62)}$$

with initial conditions set to the same as the Ca_{SR} concentrations. This is the value of Ca_{SR} that is passed into the spark-population model Ca_{SR} dependent functions.

A.4. Variable t-system density

T-system and non-t-system population sizes. First, the total population of CRUs must be assigned based on the t-system density parameter, ρ_{T}, by calculating the number

of surface and interior CRUs and then assigning interior CRUs to either the t-system or non-t-system populations:

$$N_{\text{surface}}^{\text{CRU}} = 2N_zN_y + 2(N_x-2)N_z + 5(N_x-2)\big(N_y-2\big) \tag{A.63}$$

$$N_{\text{interior}}^{\text{CRU}} = N_{\text{T}} - N_{\text{surface}}^{\text{CRU}} \tag{A.64}$$

$$(N_{\text{T}})^{\cancel{\text{tsys}}} = N_{\text{interior}}^{\text{CRU}}(1-\rho_{\text{T}}) \tag{A.65}$$

$$(N_{\text{T}})^{\text{tsys}} = N_{\text{T}} - (N_{\text{T}})^{\cancel{\text{tsys}}} \tag{A.66}$$

$$\left(n^{\text{CRU}}\right)^{\text{tsys}} = \frac{(N_{\text{T}})^{\text{tsys}}}{N_{\text{T}}} \tag{A.67}$$

$$\left(n^{\text{CRU}}\right)^{\cancel{\text{tsys}}} = 1 - \left(n^{\text{CRU}}\right)^{\text{tsys}} \tag{A.68}$$

Two populations of the spark-population model are then created based on the population sizes $(N_{\text{T}})^{\text{tsys}}$ and $(N_{\text{T}})^{\cancel{\text{tsys}}}$. The non-t-system state transitions are solved in exactly the same way as the t-system population, except that there is no triggered spark population associated with the non-system model.

Coupling between the t-system and non-t-system populations. The two populations are solved independently, with coupling between them occurring through the activation of wavelet CRUs: wavelet CRUs of either population can be activated by triggered, spontaneous and wavelet recruiter CRUs from the t-system population and by spontaneous and wavelet CRUs from the non-t-system population. The number of recruiter CRUs and number of neighbours parameter determines the number of CRUs available for activation of a wavelet CRU (eqns A.21–A.28); this is now distributed between the two populations dependent on the ratio of the populations. An additional random binomial sample was conducted to determine how many of the available neighbours for activation are from the t-system population, and the remaining are set to be available for the non-system population. For example let's consider the number of wavelets that are activated by currently recruiter triggered CRUs:

$$P_{\text{recruiter}}^{\text{tot}} = nei^{\text{trig}}\left(N_{\text{recruiter-Jrel}}^{\text{trig}} + N_{\text{recruiter-nonJrel}}^{\text{trig}}\right) \tag{A.69}$$

$$(P_{\text{recruiter}})^{\text{tsys}} = \text{B}\left(\left(n^{\text{CRU}}\right)^{\text{tsys}}, P_{\text{recruiter}}^{\text{tot}}\right) \tag{A.70}$$

$$(P_{\text{recruiter}})^{\cancel{\text{tsys}}} = P_{\text{recruiter}}^{\text{tot}} - (P_{\text{recruiter}})^{\text{tsys}} \tag{A.71}$$

These available populations, $(P_{\text{recruiter}})^{\text{tsys}}$ and $(P_{\text{recruiter}})^{\cancel{\text{tsys}}}$, are then the ones that are passed into the binomial sample (eqns A.22, A.25 and A.28) to determine the actual number of created CRUs of either population (with each limited to the total $N_{\text{available}}$ of each population). The same process is followed for all mechanisms of activation of wavelet CRUs, providing coupling between the populations through spatial recruitment.

For whole-cell calcium waves the size of the wavefront is distributed between the two populations based on the ratio of their population sizes.

Implementation in the cell models. A copy of all of the intracellular calcium state variables and non-membrane fluxes was made to model the calcium dynamics in the non-t-system population. The number of active J_{rel} CRUs in the t-system and non-t-system spark-populations models is then coupled to the appropriate compartment of the cell model through controlling J_{rel} in each compartment. The non-t-system model has its own associated effective Ca_{SR}:

$$\frac{d\left(Ca_{\text{SR}}^{\text{eff}}\right)^{\cancel{\text{tsys}}}}{dt} = \frac{\left(Ca_{\text{jSR}}\right)^{\cancel{\text{tsys}}} - \left(Ca_{\text{SR}}^{\text{eff}}\right)^{\cancel{\text{tsys}}}}{\left(\tau_{Ca_{\text{SR}}^{\text{eff}}}\right)^{\cancel{\text{tsys}}}} \tag{A.72}$$

And the calcium concentrations in the cytosolic and network SR spaces are coupled between the t-system and non-t-system compartments as described by the following calcium fluxes:

$$J_{Ca_{\text{i}}}^{\text{tsys}\to\cancel{\text{tsys}}} = \frac{(Ca_{\text{i}})^{\text{tsys}} - (Ca_{\text{i}})^{\cancel{\text{tsys}}}}{\tau_{Ca_{\text{i}}}^{\text{tsys}\to\cancel{\text{tsys}}}} \tag{A.73}$$

$$J_{Ca_{\text{SR}}}^{\text{tsys}\to\cancel{\text{tsys}}} = \frac{(Ca_{\text{SR}})^{\text{tsys}} - (Ca_{\text{SR}})^{\cancel{\text{tsys}}}}{\tau_{Ca_{\text{SR}}}^{\text{tsys}\to\cancel{\text{tsys}}}} \tag{A.74}$$

A.5. Wavefront termination algorithm

Wavefront termination is imposed to capture wavefront destructive interference and hitting the edges of a cell, while also imposing that full-cell waves are terminated if sufficient triggered CRUs are activated. Wavefront termination is always achieved by transitioning CRUs from the excited wave state to the recruiter state, without contributing to the calculation of the number of created recruiter sparks that determines wavefront propagation (eqn A.36). Hence the CRUs remain active and contribute to J_{rel}, but are not able to continue to sustain propagation of the wavefront. First let us consider a triggered excitation, which should interrupt a calcium wave. If $\left(N_{\text{excited}}^{\text{trig}} > 0.075N_{\text{T}}\right)$, then impose the following:

$$N_{\text{recruiter-Jrel}}^{\text{wave}} = N_{\text{recruiter-Jrel}}^{\text{wave}} + N_{\text{excited}}^{\text{wave}} \tag{A.75}$$

$$N_{\text{excited}}^{\text{wave}} = 0 \tag{A.76}$$

The second way a wavefront is terminated is due to hitting other wavefronts or the edge of the cell. This is calculated by determining the current number of wavefronts and then performing a random sample to determine how many wavefronts will be destroyed. First determine the number of destroyed wavefronts:

$$N_{\text{wavefronts}} = \frac{N_{\text{excited}}^{\text{wave}}}{0.7 N_x N_y} \quad \text{(A.77)}$$

$$N_{\text{destroyed-wavefronts}} = B\left(\frac{N_{\text{wavefronts}}}{N_z}, N_{\text{wavefronts}}\right) \quad \text{(A.78)}$$

Then if the number of destroyed wavefronts is greater than zero, that number of CRUs will be transitioned to the recruiter state as in eqns A.75 and A.76. Note that due to Ca_{SR} depletion, full-cell waves often self-terminate before this algorithm has been implemented. But this does get used when many waves are created simultaneously or in the case of insufficient Ca_{SR} depletion to terminate the wave.

A.6. Functional forms of α transition rates

In full the dependence of the α transition rates on Ca_{SR} and I_{CaL} is described below.

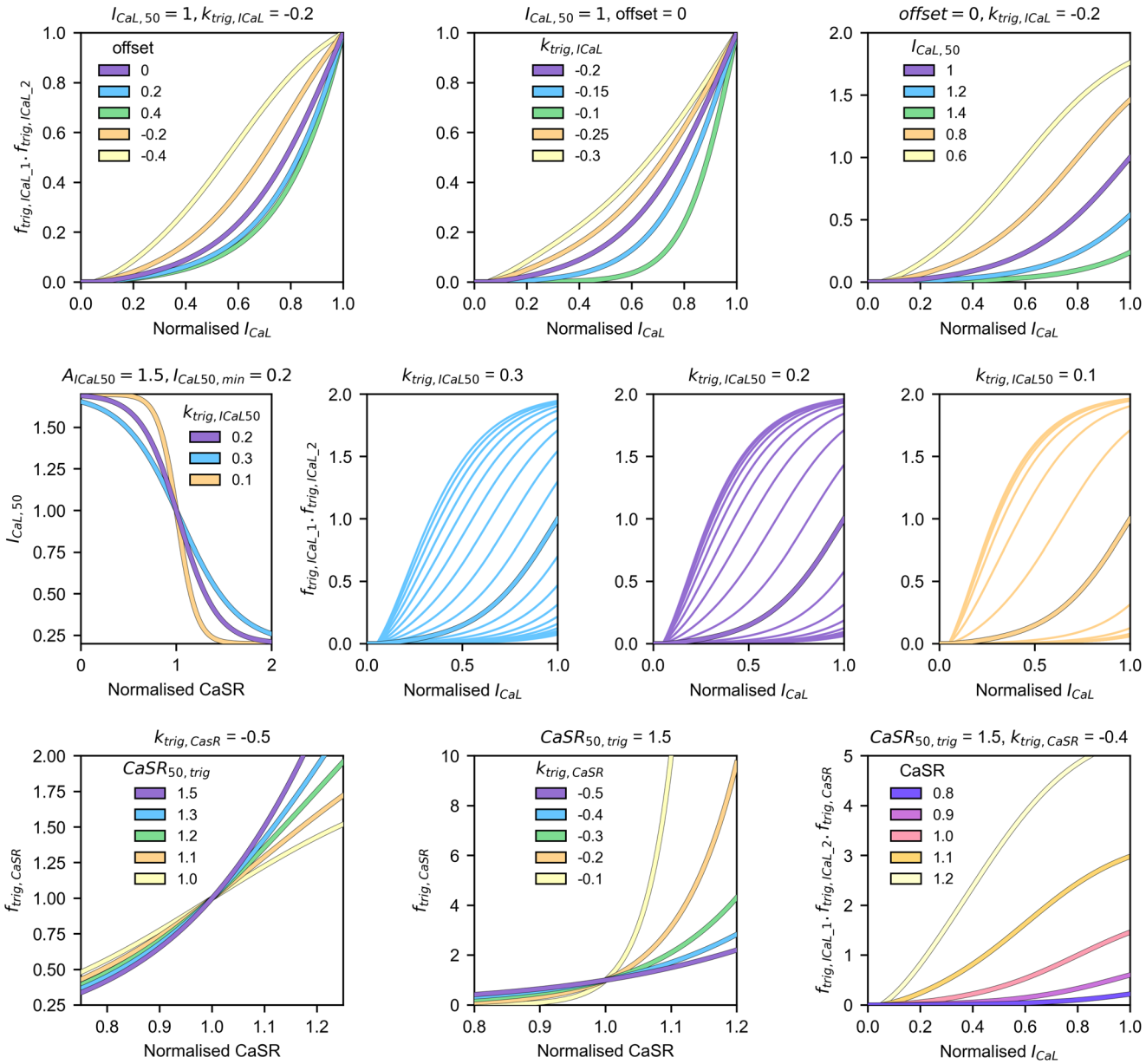

Figure A1. Forms of the functions that determine I_{CaL} and Ca_{SR} dependence of the α transition rate. The first row, first panel illustrates how the offset affects the shape; second panel illustrates the effect of the gradient and the third panel shows the half maximal activation. Second row illustrates how the half maximal activation constant can depend on Ca_{SR} and the impact that has on the shape of the response at different Ca_{SR} and different gradients of its dependence. The third panel illustrates the direct Ca_{SR} dependence and the combination of all the functions together.

Table A1. Parameter values for the spark-population model integrated into the Grandi atria, Grandi ventricle and CRN atria models.

Description	Abbreviation	Grandi atria	Grandi ventricle	CRN atria
# of CRUs in X direction	N_x	15	15	15
# of CRUs in Y direction	N_y	20	20	20
# of CRUs in Z direction	N_z	65	65	65
Total # of CRUs	N_T	$N_xN_yN_z$	$N_xN_yN_z$	$N_xN_yN_z$
# of neighbours coupled to triggered CRUs	nei^{trig}	2	2	2
# of neighbours coupled to spontaneous CRUs	nei^{spont}	6	6	6
# of neighbours coupled to wavelet CRUs	nei^{wavelet}	2	2	2
Time between excited and recruiter	$t_{\text{wavedelay}}$	10 ms	10 ms	10 ms
Time J_{rel} active	$t_{J_{\text{rel}}}$	40 ms	30 ms	15 ms
Time available for recruitment	t_{recruit}	41 ms	40 ms	40 ms
Recovery rate	r_{recov}	0.004125 ms^{-1}	0.004125 ms^{-1}	0.004125 ms^{-1}
Rescaling factor of N_{RyR} to $RyR_{\text{O}}^{\text{max}}$	$N_{\text{RyR}}^{\text{model-rescale}}$	0.00342965	0.0064	0.075
Time constant of $Ca_{\text{SR}}^{\text{eff}}$ adjustment	$\tau_{Ca_{\text{SR}}^{\text{eff}}}$	20 ms	20 ms	20 ms
Time constant of $Ca_{\text{SR}}^{\text{eff}}$ adjustment in non-t-system CRUs	$\left(\tau_{Ca_{\text{SR}}^{\text{eff}}}\right)^{\cancel{\text{tsys}}}$	40 ms	40 ms	40 ms
Time constant of Ca_{i} coupling between t-system and non-t-system	$\tau_{Ca_{\text{i}}}^{\text{tsys}\rightarrow\cancel{\text{tsys}}}$	50 ms	50 ms	50 ms
Time constant of Ca_{SR} coupling between t-system and non-t-system	$\tau_{Ca_{\text{SR}}}^{\text{tsys}\rightarrow\cancel{\text{tsys}}}$	250 ms	250 ms	250 ms
Triggered spark act. rate const.	C_α^{trig}	0.09 ms^{-1}	0.05 ms^{-1}	0.15 ms^{-1}
Normalised $I_{\text{CaL}_{50}}$ offset	$I_{\text{CaL}_{\text{offset}}}$	0.4	0.2	0
Gradient parameter α vs. I_{CaL}	k_{ICaL}	−0.25	−0.4	−0.35
Gradient parameter $I_{\text{CaL}_{50}}$ vs. Ca_{SR}	$k_{\text{ICaL,50}}$	0.1	0.1	0.1
Gradient parameter α vs. Ca_{SR}	$k_{\text{CaSR}}^{\text{trig}}$	−0.375	−0.5	−1.5
Half maximal act. const. (Ca_{SR})	$Ca_{\text{SR}_{50}}^{\text{trig}}$	1.5	1.5	1.5
Minimum value of $I_{\text{CaL}_{50}}$	$I_{\text{CaL}_{50}}^{\text{min}}$	0.2	0.2	0.2
Scaling factor of the $I_{\text{CaL}_{50}}$-Ca_{SR} relationship	$A_{\text{ICaL,50}}$	1.8	1.8	1.8
Spontaneous spark act. rate const.	C_α^{spont}	2×10^{-6} ms^{-1}	2×10^{-6} ms^{-1}	2×10^{-6} ms^{-1}
Gradient parameter α vs. Ca_{SR}	$k_{\text{CaSR}}^{\text{spont}}$	−0.1	−0.1	−0.2
Half maximal act. const. (Ca_{SR})	$Ca_{\text{SR}_{50}}^{\text{spont}}$	1.5	1.5	2.5
Wavelet spark act. rate const. (from triggered)	$C_\alpha^{\text{wavelet-trig}}$	0.01 ms^{-1}	0.01 ms^{-1}	0.01 ms^{-1}
Wavelet spark act. rate const. (from spontaneous)	$C_\alpha^{\text{wavelet-spont}}$	0.005 ms^{-1}	0.005 ms^{-1}	0.005 ms^{-1}
Wavelet spark act. rate const. (from wavelet)	$C_\alpha^{\text{wavelet-wavelet}}$	0.01 ms^{-1}	0.01 ms^{-1}	0.01 ms^{-1}
Gradient parameter α vs. Ca_{SR}	$k_{\text{CaSR}}^{\text{wavelet}}$	−0.5	−0.75	−2
Half maximal act. const. (Ca_{SR})	$Ca_{\text{SR}_{50}}^{\text{wavelet}}$	1.5	1.5	1.5
Wavelet act. threshold	$Ca_{\text{SR}_0}^{\text{wavelet}}$	0.5	0.3	0.1
Wave activation rate constant	C_α^{wave}	4×10^{-5} ms	4×10^{-5} ms	4×10^{-5} ms
Gradient parameter α vs. Ca_{SR}	$k_{\text{CaSR}}^{\text{wave}}$	−0.2	−0.2	−0.5
Half maximal act. const. (Ca_{SR})	$Ca_{\text{SR}_{50}}^{\text{wave}}$	1.2	1.18	1.27

(*Continued*)

Table A1. (Continued)

Description	Abbreviation	Grandi atria	Grandi ventricle	CRN atria
Wave initiation threshold	$Ca_{SR_0}^{init,wave}$	0.9	0.9	0.9
Wave self-propagation threshold	$Ca_{SR_0}^{prop,wave}$	0.7	0.5	0.1
Wave activation rate constant in non-t-system CRUs (~~tsys~~)	$(C_\alpha^{wave})^{~~tsys~~}$	4×10^{-6} ms	4×10^{-6} ms	4×10^{-6} ms
Spontaneous spark act. rate const. in non-t-system CRUs (~~tsys~~)	$\left(C_\alpha^{spont}\right)^{~~tsys~~}$	2×10^{-6} ms^{-1}	2×10^{-6} ms^{-1}	2×10^{-6} ms^{-1}
Wavelet spark act. rate const. (from triggered), ~~tsys~~	$\left(C_\alpha^{wavelet\text{-}trig}\right)^{~~tsys~~}$	0.03 ms^{-1}	0.03 ms^{-1}	0.03 ms^{-1}
Wavelet spark act. rate const. (from spontaneous), ~~tsys~~	$\left(C_\alpha^{wavelet\text{-}spont}\right)^{~~tsys~~}$	0.005 ms^{-1}	0.005 ms^{-1}	0.005 ms^{-1}
Wavelet spark act. rate const. (from wavelet), ~~tsys~~	$\left(C_\alpha^{wavelet\text{-}wavelet}\right)^{~~tsys~~}$	0.03 ms^{-1}	0.03 ms^{-1}	0.03 ms^{-1}

Triggered sparks.

$$\alpha_{trig} = C_\alpha^{trig} f_{ICaL}^{trig} f_2^{trig} f_{CaSR}^{trig} \tag{A.79}$$

$$f_2^{trig} = \frac{2}{1 + e^{(I_{CaL} - 0.05)/-0.1}} - 1 \tag{A.80}$$

$$f_{ICaL}^{trig} = \frac{A_{ICaL}^{trig}}{1 + e^{\left(I_{CaL} - \left(I_{CaL_{50}} + I_{CaL_{offset}}\right)\right)/k_{ICaL}}} \tag{A.81}$$

$$f_{CaSR}^{trig} = \frac{A_{CaSR}^{trig}}{1 + 10^{\left(Ca_{SR} - Ca_{SR_{50}}^{trig}\right)/k_{CaSR}^{trig}}} \tag{A.82}$$

$$A_{ICaL}^{trig} = 1 + e^{-I_{CaL_{offset}}/k_{ICaL}} \tag{A.83}$$

$$A_{CaSR}^{trig} = 1 + 10^{\left(1 - Ca_{SR_{50}}^{trig}\right)/k_{CaSR}^{trig}} \tag{A.84}$$

$$I_{CaL_{50}} = \frac{A_{ICaL,50}}{1 + e^{\left(Ca_{SR} - Ca_{SR_{50}}^{ICaL,50}\right)/k_{ICaL,50}}} + I_{CaL_{50}}^{min} \tag{A.85}$$

$$Ca_{SR_{50}}^{ICaL,50} = -\ln\left(\frac{A_{ICaL,50}}{1 - I_{CaL_{50}}^{min}} - 1\right) k_{ICaL,50} + 1 \tag{A.86}$$

Spontaneous sparks.

$$\alpha_{spont} = C_\alpha^{spont} f_{CaSR}^{spont} \tag{A.87}$$

$$f_{CaSR}^{spont} = \frac{A_{CaSR}^{spont}}{1 + 10^{\left(Ca_{SR} - Ca_{SR_{50}}^{spont}\right)/k_{CaSR}^{spont}}} \tag{A.88}$$

$$A_{CaSR}^{spont} = 1 + 10^{\left(1 - Ca_{SR_{50}}^{spont}\right)/k_{CaSR}^{spont}} \tag{A.89}$$

Wavelet sparks.

$$\alpha_{wavelet\text{-}x} = C_\alpha^{wavelet\text{-}x} f_2^{wavelet} f_{CaSR}^{wavelet} \tag{A.90}$$

$$f_{CaSR}^{wavelet} = \frac{A_{CaSR}^{wavelet}}{1 + 10^{\left(Ca_{SR} - Ca_{SR_{50}}^{wavelet}\right)/k_{CaSR}^{wavelet}}} \tag{A.91}$$

$$f_2^{wavelet} = \frac{2}{1 + e^{\left(Ca_{SR} - Ca_{SR_0}^{wavelet}\right)/-0.0001}} - 1 \tag{A.92}$$

$$A_{CaSR}^{wavelet} = 1 + 10^{\left(1 - Ca_{SR_{50}}^{wavelet}\right)/k_{CaSR}^{wavelet}} \tag{A.93}$$

Wave CRUs.

$$\alpha_{wave\text{-}wavelet} = C_\alpha^{wave} f_{CaSR}^{wave} f_2^{wave} \tag{A.94}$$

$$f_{CaSR}^{wave} = \frac{1}{1 = 10^{\left(Ca_{SR} - Ca_{SR_{50}}^{wave}\right)/k_{CaSR}^{wave}}} \tag{A.95}$$

$$f_2^{wave} = \frac{2}{1 + e^{\left(Ca_{SR} - Ca_{SR_0}^{init,wave}\right)/-0.0001}} - 1 \tag{A.96}$$

$$P(wave - wave) = 0.5\left(\frac{2}{1 + e^{\left(Ca_{SR} - Ca_{SR_0}^{prop,wave}\right)/-0.0001}} - 1\right) \tag{A.97}$$

A.7. List of parameters

References

Aistrup, G. L., Shiferaw, Y., Kapur, S., Kadish, A. H., & Wasserstrom, J. A. (2009). Mechanisms underlying the formation and dynamics of subcellular calcium alternans in the intact rat heart. *Circulation Research*, **104**(5), 639–649.

Alvarez-Lacalle, E., Echebarria, B., Spalding, J., & Shiferaw, Y. (2015). Calcium alternans is due to an order-disorder phase transition in cardiac cells. *Physical Review Letters*, **114**(10), 108101.

Bers, D. M. (2002). Cardiac excitation–contraction coupling. *Nature*, **415**(6868), 198–205.

Bers, D. M. (2006). Cardiac ryanodine receptor phosphorylation: Target sites and functional consequences. *Biochemical Journal*, **396**(1), e1–e3.

Borile, G., Zaglia, T., E Lehnart, S., & Mongillo, M. (2021). Multiphoton imaging of Ca^{2+} instability in acute myocardial slices from a RyR2(R2474S) murine model of catecholaminergic polymorphic ventricular tachycardia. *Journal of Clinical Medicine*, **10**(13), 2821.

Brette, F., Rodriguez, P., Komukai, K., Colyer, J., & Orchard, C. (2004). β-adrenergic stimulation restores the Ca transient of ventricular myocytes lacking t-tubules. *Journal of Molecular and Cellular Cardiology*, **36**(2), 265–275.

Campos, F. O., Shiferaw, Y., Whitaker, J., Plank, G., & Bishop, M. J. (2023). Subthreshold delayed after depolarizations provide an important arrhythmogenic substrate in the border zone of infarcted hearts. *Heart Rhythm*, **20**(2), 299–306.

Cheng, H., Lederer, M. R., Lederer, W. J., & Cannell, M. B. (1996). Calcium sparks and [Ca2+]i waves in cardiac myocytes. *American Journal of Physiology-Cell Physiology*, **270(1 pt1)**, C148–C159.

Clusin, W. T. (2007). Mechanisms of calcium transient and action potential alternans in cardiac cells and tissues. *American Journal of Physiology–Heart and Circulatory Physiology*, **294**(1), H1–H10.

Colman, M. A. (2019). Arrhythmia mechanisms and spontaneous calcium release: Bi-directional coupling between re-entrant and focal excitation. *PLoS Computational Biology*, **15**(8), e1007260.

Colman, M. A., Alvarez-Lacalle, E., Echebarria, B., Sato, D., Sutanto, H., & Heijman, J. (2022). Multi-scale computational modeling of spatial calcium handling from nanodomain to whole-heart: Overview and perspectives. *Frontiers in Physiology*, **13**, 836622.

Colman, M. A., Pinali, C., Trafford, A. W., Zhang, H., & Kitmitto, A. (2017). A computational model of spatio-temporal cardiac intracellular calcium handling with realistic structure and spatial flux distribution from sarcoplasmic reticulum and t-tubule reconstructions. *PLoS Computational Biology*, **13**(8), e1005714.

Courtemanche, M., Ramirez, R. J., & Nattel, S. (1998). Ionic mechanisms underlying human atrial action potential properties: Insights from a mathematical model. *American Journal of Physiology*, **275**(1), H301–H321.

Dibb, K. M., Clarke, J. D., Horn, M. A., Richards, M. A., Graham, H. K., Eisner, D. A., & Trafford, A. W. (2009). Characterization of an extensive transverse tubular network in sheep atrial myocytes and its depletion in heart failure. *Circulation: Heart Failure*, **2**(5), 482–489.

Dibb, K. M., Louch, W. E., & Trafford, A. W. (2022). Cardiac transverse tubules in physiology and heart failure. *Annual Review of Physiology*, **84**, 229–255.

Eisner, D. A., Kashimura, T., Venetucci, L. A., & Trafford, A. W. (2009). From the ryanodine receptor to cardiac arrhythmias. *Circulation Journal*, **73**(9), 1561–1567.

Ferrantini, C., Crocini, C., Coppini, R., Vanzi, F., Tesi, C., Cerbai, E., Poggesi, C., Pavone, F. S., & Sacconi, L. (2013). The transverse-axial tubular system of cardiomyocytes. *Cellular and Molecular Life Sciences*, **70**(24), 4695–4710.

Fowler, E. D., Diakite, S. L., Gomez, A. M., & Colman, M. A. (2025). Disruption of ventricular activation by subthreshold delayed afterdepolarizations in RyR2-R420Q catecholaminergic polymorphic ventricular tachycardia. *Journal of Molecular and Cellular Cardiology Plus*, **13**, 100466.

Fowler, E. D., Wang, N., Hezzell, M. J., Chanoit, G., Hancox, J. C., & Cannell, M. B. (2022). Improved Ca^{2+} release synchrony following selective modification of I_{tof} and phase 1 repolarization in normal and failing ventricular myocytes. *Journal of Molecular and Cellular Cardiology*, **172**, 52–62.

Gomez, J. F., Cardona, K., Romero, L., Ferrero Jr, J. M., & Trenor, B. (2014). Electrophysiological and structural remodeling in heart failure modulate arrhythmogenesis. 1D simulation study. *PLoS ONE*, **9**(9), e106602.

Grandi, E., Pandit, S. V., Voigt, N., Workman, A. J., Dobrev, D., Jalife, J., & Bers, D. M. (2011). Human atrial action potential and Ca^{2+} model: Sinus rhythm and chronic atrial fibrillation. *Circulation Research*, **109**(9), 1055–1066.

Grandi, E., Pasqualini, F. S., & Bers, D. M. (2010). A novel computational model of the human ventricular action potential and Ca transient. *Journal of Molecular and Cellular Cardiology*, **48**(1), 112–121.

Greiser, M. (2017). Calcium signalling silencing in atrial fibrillation. *The Journal of Physiology*, **595**(12), 4009–4017.

Greiser, M., Kerfant, B.-G., Williams, G. S., Voigt, N., Harks, E., Dibb, K. M., Giese, A., Meszaros, J., Verheule, S., Ravens, U., Allessie, M. A., Gammie, J. S., van der Velden, J., Lederer, W. J., Dobrev, D., & Schotten, U. (2014). Tachycardia-induced silencing of subcellular Ca^{2+} signaling in atrial myocytes. *Journal of Clinical Investigation*, **124**(11), 4759–4772.

Heijman, J., Sutanto, H., Crijns, H. J. G. M., Nattel, S., & Trayanova, N. A. (2021). Computational models of atrial fibrillation: Achievements, challenges, and perspectives for improving clinical care. *Cardiovascular Research*, **117**(7), 1682–1699.

Holmes, M., Hurley, M. E., Sheard, T. M. D., Benson, A. P., Jayasinghe, I., & Colman, M. A. (2022). Increased SERCA2a sub-cellular heterogeneity in right-ventricular heart failure inhibits excitation-contraction coupling and modulates arrhythmogenic dynamics. *Philosophical Transactions of the Royal Society B: Biological Sciences*, **377**(1864), 20210317.

Johnson, D. M., Heijman, J., Bode, E. F., Greensmith, D. J., van der Linde, H., Abi-Gerges, N., Eisner, D. A., Trafford, A. W., & Volders, P. G. (2013). Diastolic spontaneous calcium release from the sarcoplasmic reticulum increases beat-to-beat variability of repolarization in canine ventricular myocytes after -adrenergic stimulation. *Circulation Research*, **112**(2), 246–256.

Kanaporis, G., Martinez-Hernandez, E., & Blatter, L. A. (2023). Calcium- and voltage-driven atrial alternans: Insight from $[Ca]_i$ and V_m asynchrony. *Physiological Reports*, **11**(10), e15703.

Kazakova, D., Colman, M. A., Pradhan, A., Gudaitis, L., Nys, L., Cools, B., Rega, F., Vandenberk, B., Terracciano, C., Roderick, H. L., Sipido, K. R., & Dries, E. (2025). Early onset of Ca^{2+} waves and synchronization in multicellular clusters facilitate focal arrhythmogenesis in human heart failure. *bioRxiv*. https://doi.org/10.1101/2025.05.02.651991 [Accessed September 28, 2025]

Koivumäki, J. T., Korhonen, T., & Tavi, P. (2011). Impact of sarcoplasmic reticulum calcium release on calcium dynamics and action potential morphology in human atrial myocytes: A computational study. *PLoS Computational Biology*, **7**(1), e1001067.

Liu, M. B., de Lange, E., Garfinkel, A., Weiss, J. N., & Qu, Z. (2015). Delayed afterdepolarizations generate both triggers and a vulnerable substrate promoting reentry in cardiac tissue. *Heart Rhythm*, **12**(10), 2115–2124.

Louch, W. E., Bito, V., Heinzel, F. R., Macianskiene, R., Vanhaecke, J., Flameng, W., Mubagwa, K., & Sipido, K. R. (2004). Reduced synchrony of Ca^{2+} release with loss of T-tubules–a comparison to Ca^{2+} release in human failing cardiomyocytes. *Cardiovascular Research*, **62**(1), 63–73.

Mora, M. T., Gomez, J. F., Morley, G., Ferrero, J. M., & Trenor, B. (2019). Mechanistic investigation of Ca^{2+} alternans in human heart failure and its modulation by fibroblasts. *PLoS ONE*, **14**(6), e0217993.

Niederer, S. A., Lumens, J., & Trayanova, N. A. (2019). Computational models in cardiology. *Nature Reviews Cardiology*, **16**(2), 100–111.

Nivala, M., Ko, C. Y., Nivala, M., Weiss, J. N., & Qu, Z. (2012). Criticality in intracellular calcium signaling in cardiac myocytes. *Biophysical Journal*, **102**(11), 2433–2442.

Pinali, C., & Kitmitto, A. (2014). Serial block face scanning electron microscopy for the study of cardiac muscle ultrastructure at nanoscale resolutions. *Journal of Molecular and Cellular Cardiology*, **76**, 1–11.

Pitoulis, F. G., Watson, S. A., Perbellini, F., & Terracciano, C. M. (2020). Myocardial slices come to age: An intermediate complexity in vitro cardiac model for translational research. *Cardiovascular Research*, **116**(7), 1275–1287.

Restrepo, J. G., Weiss, J. N., & Karma, A. (2008). Calsequestrin-mediated mechanism for cellular calcium transient alternans. *Biophysical Journal*, **95**(8), 3767–3789.

Richards, M. A., Clarke, J. D., Saravanan, P., Voigt, N., Dobrev, D., Eisner, D. A., Trafford, A. W., & Dibb, K. M. (2011). Transverse tubules are a common feature in large mammalian atrial myocytes including human. *American Journal of Physiology-Heart and Circulatory Physiology*, **301**(5), H1996–H2005.

Roney, C. H., Bayer, J. D., Cochet, H., Meo, M., Dubois, R., Jaïs, P., & Vigmond, E. J. (2018). Variability in pulmonary vein electrophysiology and fibrosis determines arrhythmia susceptibility and dynamics. *PLOS Computational Biology*, **14**(5), e1006166.

Setterberg, I. E., Le, C., Frisk, M., Li, J., & Louch, W. E. (2021). The physiology and pathophysiology of T-tubules in the heart. *Frontiers in Physiology*, **12**, 718404.

Sheard, T. M. D., Hurley, M. E., Colyer, J., White, E., Norman, R., Pervolaraki, E., Narayanasamy, K. K., Hou, Y., Kirton, H. M., Yang, Z., Hunter, L., Shim, J.-U., Clowsley, A. H., Smith, A. J., Baddeley, D., Soeller, C., Colman, M. A., & Jayasinghe, I. (2019). Three-dimensional and chemical mapping of intracellular signaling nanodomains in health and disease with enhanced expansion microscopy. *ACS Nano*, **13**(2), 2143–2157.

Shiferaw, Y., Aistrup, G. L., & Wasserstrom, J. A. (2017). Mechanism for triggered waves in atrial myocytes. *Biophysical Journal*, **113**(3), 656–670.

Shiferaw, Y., Aistrup, G. L., & Wasserstrom, J. A. (2018). Synchronization of triggered waves in atrial tissue. *Biophysical Journal*, **115**(6), 1130–1141.

Smith, C. E. R., Pinali, C., Eisner, D. A., Trafford, A. W., & Dibb, K. M. (2022). Enhanced calcium release at specialised surface sites compensates for reduced t-tubule density in neonatal sheep atrial myocytes. *Journal of Molecular and Cellular Cardiology*, **173**, 61–70.

Stern, M. D., Song, L. S., Cheng, H., Sham, J. S., Yang, H. T., Boheler, K. R., & Ríos, E. (1999). Local control models of cardiac excitation-contraction coupling. A possible role for allosteric interactions between ryanodine receptors. *Journal of General Physiology*, **113**(3), 469–489.

Thul, R., Rietdorf, K., Bootman, M., & Coombes, S. (2015). Unifying principles of calcium wave propagation – Insights from a three-dimensional model for atrial myocytes. *Biochimica et Biophysica Acta (BBA) - Molecular Cell Research*, **1853**(9), 2131–2143.

Tomek, J., Zhou, X., Martinez-Navarro, H., Holmes, M., Bury, T., Berg, L. A., Tomkova, M., Jo, E., Nagy, N., Bertrand, A., Bueno-Orovio, A., Colman, M., Rodriguez, B., Bers, D., & Heijman, J. (2025). T-world: A highly general computational model of a human ventricular myocyte. *Circulation Research*, **138**(10), e328073.

Wang, K., Lee, P., Mirams, G. R., Sarathchandra, P., Borg, T. K., Gavaghan, D. J., Kohl, P., & Bollensdorff, C. (2015). Cardiac tissue slices: Preparation, handling, and successful optical mapping. *American Journal of Physiology-Heart and Circulatory Physiology*, **308**(9), H1112–H1125.

Xie, Y., Sato, D., Garfinkel, A., Qu, Z., & Weiss, J. N. (2010). So little source, so much sink: Requirements for afterdepolarizations to propagate in tissue. *Biophysical Journal*, **99**(5), 1408–1415.

Zhang, X., Ni, H., Morotti, S., Smith, C. E. R., Sato, D., Louch, W. E., Edwards, A. G., & Grandi, E. (2023). Mechanisms of spontaneous Ca^{2+} release-mediated arrhythmia in a novel 3D human atrial myocyte model: I. Transverse-axial tubule variation. *The Journal of Physiology*, **601**(13), 2655–2683.

Zhong, M., & Karma, A. (2024). Role of ryanodine receptor cooperativity in Ca^{2+}-wave-mediated triggered activity in cardiomyocytes. *The Journal of Physiology*, **602**(24), 6745–6787.

Additional information

Data availability statement

Underlying source code is provided with full documentation in the Zenodo repository https://doi.org/10.5281/zenodo.18671615.

Competing interests

The authors declare no potential conflict of interests.

Author contributions

M.A.C.: Concept and design; Model development; Code implementation; Simulations; Interpretation and analysis; Illustrations; Draft; Editing; Supplementary materials/Appendix. Y.S.: Concept and design; Interpretation and analysis; Draft; Editing. D.C.: Code implementation; Interpretation and analysis; Draft; Editing; Supplementary materials/Appendix.

Funding

This project was supported by a Medical Research Council Career Development Award (MR/V010050/1), awarded to M.A.C. D.C. was supported by a Human Frontier Science Program grant (RGP010/2024) awarded to M.A.C. Y.S. was supported by the National Institute of General Medical Sciences (1R16GM153647-01) and the National Science Foundation (2320846).

Keywords

alternans, calcium handling, calcium sparks and waves, excitation-contraction coupling, multi-scale modelling

Supporting information

Additional supporting information can be found online in the Supporting Information section at the end of the HTML view of the article. Supporting information files available:

Peer Review History